Electronic Thesis and Dissertation Repository

8-9-2019 2:00 PM

Investigating the Mechanisms of Breast Cancer Metastasis Using Multimodality Molecular Imaging

Katie Parkins, *The University of Western Ontario*

Supervisor: Foster, Paula J., *The University of Western Ontario*
Joint Supervisor: Ronald, John A., *The University of Western Ontario*
A thesis submitted in partial fulfillment of the requirements for the Doctor of Philosophy degree in Medical Biophysics
© Katie Parkins 2019

Follow this and additional works at: https://ir.lib.uwo.ca/etd

Part of the Translational Medical Research Commons

Abstract

Introduction: Breast cancer recurrence continues to be a significant challenge in the clinic. Despite successful removal and/or treatment of the original tumour, many patients experience relapse in the breast or at distant sites. Furthermore, the diagnosis of metastatic disease often occurs too late for effective treatment. **Methods**: In this thesis, we combine iron-based cellular MRI and longitudinal BLI to noninvasively track the fate of breast cancer cells into overt tumours in the mouse brain. We then apply this imaging model to study the effect of a primary breast tumour on the growth of secondary metastases in an immune competent mouse model. Finally, we utilized dual-luciferase BLI to investigate the potential of self-homing circulating tumour cells (CTCs) as a novel cancer theranostic in both orthotopic and metastatic models of breast cancer. **Results**: BLI complemented our cellular MRI technologies well by providing longitudinal measures of cancer cell viability. Using *in vivo* BLI/MRI, we demonstrated the presence of a 4T1 primary tumour significantly enhances total brain tumour burden. Finally, using dual-luciferase BLI, we demonstrated the ability of experimental CTCs to home to and treat primary tumours and disseminated breast cancer lesions. **Conclusion**: MRI and BLI are complementary technologies to noninvasively study the fate of breast cancer cells, as well as the mechanisms contributing to metastasis including CTR/CTE and tumour self-homing. Furthermore, we provide evidence that CTCs are a novel theranostic platform for the visualization and treatment of pre-established tumour sites throughout the body.

Keywords

Summary for Lay Audience

Introduction: Metastasis is defined as the spread of cancer cells from the original tumour to other parts of the body and is responsible for the majority of cancer related deaths. Thus, there is a need to better understand the mechanisms that contribute to the progression and spread of cancer. **Methods**: In this thesis, we used novel molecular imaging tools to study potential mechanisms of breast cancer metastasis in mouse models. We combined two complementary imaging technologies, cellular magnetic resonance imaging (MRI) and bioluminescence imaging (BLI) to get a more complete picture of breast cancer cell fate in the brain over time. We then applied these technologies to study the impact of a primary tumour on the growth of secondary metastases in the body. Finally, we applied non-invasive imaging to investigate the potential of circulating tumour cells as a novel delivery vehicle for anti-cancer therapeutics in mouse models of breast cancer. **Results**: BLI complemented our cellular MRI technologies well by providing longitudinal measures of cancer cell viability. Using *in vivo* BLI/MRI, we demonstrated the presence of a primary tumour enhances total brain tumour burden. Finally, using BLI, we demonstrated the ability of circulating tumour cells to home to and treat primary tumours and disseminated lesions. **Conclusion**: MRI and BLI are complementary technologies to noninvasively study the fate of breast cancer cells, as well as the mechanisms contributing to metastatic spread.

Co-Authorship Statement

Chapter 1 contains material from 3 previously published book chapters. The first book chapter is Parkins KM, Makela AV, Hamilton AM, Foster PJ (2018). "Cellular Magnetic Resonance Imaging for Tracking Metastatic Cancer Cells in the Brain" *Methods in Molecular Biology; Brain tumor stem cells,* and is included with permission of Springer. KMP and PJF wrote the majority of the manuscript. AVM and AMH also contributed to writing and editing the manuscript. The second book chapter is Makela A*, Murrell DH*, Parkins KM, Kara J, Gaudet J, Foster PJ (2016). "Cellular Imaging with MRI" *Topics in Magnetic Resonance Imaging*. AVM, DHM and PJF wrote the majority of the manuscript. KMP, JK and JG also contribute to the writing and editing of the manuscript. The third book chapter is Bazalova-Carter M, Murrell DH, Parkins KM, Ronald J, Foster PJ, Graves E, Granton P, and Wong E (2016). "Small Animal Radiotherapy and Imaging" *Advances in Medical Biophysics.* KMP and JAR wrote a subsection on Bioluminescence Imaging. MBC, DHM, PJF, EG, and PG were authors of additional subsections. EW edited and prepared the chapter.

Chapter 2 is reprinted from: Parkins KM, Hamilton AM, Makela AV, Chen Y, Foster PJ, Ronald JA (2016). "A multimodality imaging model to track viable cancer cells from single arrest to metastasis" *Scientific Reports.* KMP contributed to experimental design, data collection and analysis, and drafted the manuscript. AMH assisted with training and *in vivo* imaging. AVM performed intracardiac injections and assisted with data analysis. CY performed the histology and immunohistochemistry. PJF and JAR contributed to experimental design and drafting the manuscript.

Chapter 3 is reprinted from: Parkins KM, Dubois V, Hamilton AM, Makela AV, Ronald JA, Foster PJ (2018). "Multimodality cellular and molecular imaging of the impact of a primary tumor on metastatic growth in a syngeneic mouse model of breast cancer brain metastasis" *Scientific Reports*. KMP contributed to experimental design, data collection and analysis, and drafted the manuscript. VD assisted with *in vitro* data collection and analysis. AMH performed cell engineering and FACS analysis. AVM performed intracardiac injections and assisted with data analysis. PJF and JAR contributed to experimental design and drafting the manuscript.

Chapter 4 is in preparation for submission. Parkins KM, Dubois VP, Kelly JJ, Chen Y, Foster PJ, Ronald JA. "Engineering self-homing circulating tumor cells as novel cancer theranostics". *In preparation*. KMP contributed to experimental design, data collection and analysis, and drafted the manuscript. VD assisted with *in vitro* data collection and analysis. JJK performed cell engineering and FACS analysis. CY performed the histology and immunohistochemistry. PJF and JAR contributed to experimental design and drafting the manuscript.

Acknowledgments

I feel very fortunate to have been a part of the Medical Biophysics and Molecular Imaging graduate programs at the University of Western Ontario. Throughout my graduate studies I have had the opportunity to work with many amazing people who have greatly influenced the researcher I have become and the accomplishments I have been able to achieve.

First, I am very grateful to my supervisor, Dr. Paula Foster, for agreeing to take me on four years ago and supporting me all the way through to successfully pursue a PhD in Medical Biophysics. Your calm nature and compassionate teaching style will surely be missed as I take on my new adventure in Baltimore. Thank you for always looking for opportunities to introduce me to leaders in our field and providing opportunities for me to travel the world and present my research. Secondly, I feel so fortunate to have had the opportunity to also be supervised by Dr. John Ronald. John, your "cheerleader" enthusiasm for science is contagious and I couldn't have got through these last four years without your support and encouragement. I am so very grateful for all of the time you spent making my conference abstracts, manuscripts and scholarship applications completely red – future Ronald lab members are so lucky to have someone that dedicates so much time to their students. I feel beyond lucky to have you both as mentors, role models and friends.

I would like to express my sincerest appreciation to my advisory committee members, Drs Alison Allan and Michael Lock. Thank you for your continued support and guidance throughout my PhD. I have thoroughly enjoyed working with both of you and appreciate all of your contributions to the work I was able to accomplish in the last four years.

A huge thank you to the "OG" Foster lab members who pushed me along in my first three years (usually to grad club). Drs Donna Murrell, Jeff Gaudet and Ashley Makela, thank you for being the role models I needed as a new Masters student with no idea what I was doing or where I was going. I'm so grateful for your helpful advice, your leadership and your friendship over the years. I look forward to many more conferences, grad club days, and Christmas parties together with the Foster lab family.

To the new Foster lab "sorority sisters", I'm so glad to have been a part of your first year. It's hard to believe how quickly it went by as we've all become such good friends. Natasha-thank you for always being agreeable to coffee dates, talking me into an Aritzia trip, and making my slides "mic drop" worthy. Your friendship over the last year means more than you know. Veronica (V)- thank you for being my person for the last three years. I couldn't have got through any of my PhD projects without your help. I truly can't wait to see all of the amazing things you all accomplish in the years to come.

A tremendous thank you to the other members of CMIG that were instrumental in my graduate training, both scientifically and otherwise. To Drs Amanda Hamilton and John Kelly (JK), thank you for teaching me (or trying) all of your mad molecular bio skills and not laughing when I ask ridiculous questions. I am extremely grateful for your guidance and your friendship over the years. A huge thank you to Dr Yuanxin Chen who performed much of the histology in my thesis. To Dave Reese for "helping" when the 3T went down. To (the future Dr) Melissa Evans who kept me in line during months of studying, grad club

days, wearing the proper PPE and requesting lab meeting donuts. To Dr Timothy Scholl, thank you for your commitment as an examiner, your company at grad club and all of your "me trout" jokes. To Dr Savita Dhanvantari who led the Molecular Imaging Graduate program- thank you for your inspirational leadership over the years and for all of your support in helping us to present our work at conferences. To all of the other past and present members of the Ronald, Foster and Scholl groups, thank you for all of the great discussions in lab meeting, chats in the bullpen and drinks at Grad Club. You will all be missed more than you know.

A special thank you to my family who was fortunately close by to support me through this journey. I am so very lucky to have so many people in my life that believe in me and are genuinely excited to see what I accomplish next. Thank you for sitting through my practice talks and always pretending to be interested. I couldn't have done any of this without you. Thank you all for celebrating this achievement with me.

Table of Contents

List of Figures

List of Abbreviations

ATP	Adenosine triphosphate
BBB	Blood brain barrier
BLI	Bioluminescence imaging
bSSFP	Balanced steady state free precession
BTB	Blood tumour barrier
CCD	Charge coupled device
CD	Cytosine deaminase
CD:UPRT	Cytosine deaminase: uracil phosphoribosyl transferase
COX-2	Cyclooxygenase
CT	Computed tomography
CTC	Circulating tumour cell
CTE	Concomitant tumour enhancement
CTR	Concomitant tumour resistance
CXCL1	Chemokine (C-X-C motif) ligand 1

EGFR	Epidermal growth factor receptor
ER	Estrogen receptor alpha
FLuc	*Firefly* luciferase
GCV	Ganciclovir
Gd	Gadolinium
GE	Gradient echo
GFP	Green fluorescent protein
GM-CSF	Granulocyte-macrophage colony stimulating factor
HER2	Human epidermal growth factor receptor 2
HSV-TK	Herpes simplex virus thymidine kinase
IL-6	Interleukin 6
IL-8	Interleukin 8
M-tyrosine	Meta-tyrosine
Mn	Manganese
mpMRI	Multiparametric magnetic resonance imaging
MPIO	Micron sized iron oxide particle
MRI	Magnetic resonance imaging
O-tyrosine	Ortho-tyrosine
PAI	Photoacoustic imaging
PET	Positron emission tomography
PR	Progesterone receptor
RLuc	*Renilla* luciferase
RF	Radiofrequency

SE	Spin echo
SNR	Signal to noise ratio
SPECT	Single photon emission computed tomography
SPIO	Superparamagnetic iron oxide
SRS	Stereotactic radiosurgery
STAT3	Signal transducer and activator of transcription 3
TNBC	Triple negative breast cancer
TNF	Tumour necrosis factor
TR	Repetition time
US	Ultrasound
USPIO	Ultra-small superparamagnetic iron oxide
WBRT	Whole brain radiotherapy treatment
5'FC	5-Fluorocytosine
5'FU	5-Fluorouracil
5'FUMP	5-Fluorouridine monophosphate

Chapter 1

1   Introduction

This thesis employs cellular magnetic resonance imaging (MRI) and bioluminescence imaging (BLI) to visualize metastatic disease in animal models of breast cancer, to investigate potential mechanisms that contribute to metastatic spread, and to evaluate the ability of circulating tumor cells to home to pre-established lesions. This introductory chapter discusses how metastasis occurs, the relevant mechanisms we are exploring, and the imaging technologies we are using. This chapter provides background information and motivation for the studies presented in this thesis.

1.1   Motivation and Overview

Breast cancer recurrence continues to be a significant challenge in the clinic. Despite successful removal and/or treatment of the original tumour, many patients experience relapse in the breast or at distant sites. Furthermore, the diagnosis of metastatic disease often occurs too late for effective treatment as a result of clinical imaging modalities that lack the sensitivity necessary for early detection.

In this thesis, experimental imaging technologies are applied to study the mechanisms that contribute to breast cancer metastasis. In Chapter 2, we explore the advantages of combining iron-based cellular MRI and longitudinal BLI to noninvasively track the fate of solitary cancer cells into overt tumours in the mouse brain. In chapter 3, we apply this new imaging model to study the effect of a primary breast tumour on the growth of secondary

metastases in an immune competent mouse model. In chapter 4, we utilize dual-luciferase BLI to visualize the tumour self-homing capabilities of experimental circulating tumour cells (CTCs) in both orthotopic and metastatic models of breast cancer. Further, based on our self-homing results, we engineered CTCs with a suicide gene therapy system to explore their potential as a delivery vehicle for anti-cancer drugs. Finally, chapter 5 summarizes the major findings and significance of this thesis. In addition, limitations of this work and future directions are discussed.

1.2   Metastatic Breast Cancer

Breast cancer is the second leading cause of cancer related mortality in North America with a 99% 5-year survival rate for localized disease (stage I) that drops to 85% for regional disease (stages II-III), and further drops to a dismal 26% when the disease is metastatic (stage IV) at the time of diagnosis [1]. Breast cancer metastasis occurs when cells leave the original breast tumour, travel through the circulation and spread to other organs, most commonly the brain, bone, lung and liver [2].

Clinically, breast cancer can be divided into three main subtypes: 1) those expressing the estrogen receptor alpha (ER+), which typically also express the progesterone receptor (PR+), 2) those that overexpress human epidermal growth factor receptor 2 (HER2+) and 3) those that do not express any of the three markers termed "triple negative" breast cancers (TNBC) [3-6]. More recently, five additional molecular subtypes of breast cancer have been identified as a result of advancements in gene expression profiling. These include 1) luminal A (ER+, with low proliferation signatures), 2) luminal B (ER+, with high proliferation signatures), 3) basal like, 4) HER2+ enriched, and 5) normal breast-like.

Additionally, the Claudin-low subtype was identified and characterized as having low expression of Claudins 3, 4 and 7 [7], enriched for mesenchymal markers [8], and often a triple-negative phenotype. Each subtype has been shown to have different clinical features including common sites of metastasis, treatment response and overall survival [9-10].

1.2.1 Brain Metastasis

Breast cancer is the second most likely cancer to metastasize to the brain, estimated to be present in 0.41% of all breast cancer patients at the time of diagnosis [11-12]. Brain metastases can occur in all breast cancer patients; however, patients with triple negative and HER2+ breast cancer have a significantly higher incidence of brain metastasis than other breast cancer subtypes. A study by Jin and colleagues found that approximately one third of patients with TNBC and HER2+ breast cancer will develop brain metastases throughout the course of their disease [13]. Other studies have reported brain metastasis incidence rates of up to 50% for HER2+ breast cancer patients [14]. Furthermore, TNBC patients have a worse prognosis after developing brain metastases, with a shorter median survival time than in patients with other subtypes of breast cancer including HER2+ [13]. In this thesis, we utilize mouse models of TNBC and HER2+ breast cancers that metastasize to the brain.

1.2.2 Metastatic Colonization

Cancer metastasis has been shown to be a very inefficient process with the primary tumour shedding a high number of CTCs and very few going on to form overt metastases [15]. Experimental studies have shown that approximately 0.01% of cells injected into the

circulation will develop into metastases, with the majority of cells being destroyed by either the immune system or hemodynamic forces [16]. For metastatic cancer cells to successfully colonize the brain, they must survive within the vasculature, arrest in the microcirculation, and extravasate into the brain parenchyma. While many cancer cells will successfully execute these initial steps to get into the brain, survival outside the vasculature and adaptation to the surrounding tissue are both extremely inefficient steps, as they require sufficient oxygen and nutrients prior to any new tumour vasculature being formed [17-18].

1.2.3 Dormancy

Cancer cells that successfully colonize distant organs have three potential cell fates: 1) proliferation to form metastases, 2) cell death or 3) cell dormancy. Cancer cell dormancy is when a cancer cell goes into a quiescent state, remaining viable but not actively proliferating. A cancer cell can remain in a dormant state until it is triggered to become proliferative again. The factors that influence a cancer cell's ability to escape dormancy remain fairly unclear but are likely to contribute to cancer recurrence [19-21].

Importantly, there are currently no definitive markers to identify dormant cancer cells *in vivo*, which makes the study of cancer cell dormancy very challenging. Previous work has included *ex vivo* studies that confirm the absence of both proliferative and apoptotic markers to suggest a state of dormancy, as well as the retention of imaging agents to exploit nondividing from dividing cell populations *in vivo* [22]. In 2002, Naumov and colleagues showed that breast cancer cells can be labeled with fluorescent nanospheres and imaged with intravital microscopy. They defined dormant cells as those that retain their fluorescent label over time *in vivo,* as proliferative cells lose their label through cell division and

4

become undetectable. They found a large proportion of cells persisted as dormant cancer cells and were able to confirm viability by recovering the tissue and showing these cells were capable of returning to a proliferative state both in culture and *in vivo*. Similarly, groups including ours have shown the retention of iron oxides can be used to longitudinally visualize nonproliferative cancer cells with cellular MRI technologies. This technique is further discussed in the subsection "Cellular MRI" [23-25].

1.2.4 Breast Cancer Recurrence

In many cases, women presenting with only detectable primary tumours, and whose initial treatment was deemed successful, can relapse many years following initial treatment [26]. In a study by Dent et al., it was found that patients with TNBC had a significantly increased likelihood of cancer recurrence compared to those with other subtypes. However, the time of recurrence is also different between subtypes, with TNBC patients having an increased risk of recurrence at 1 to 3 years following diagnosis, that drops after 3 years, and patients with other subtypes having a fairly steady risk of recurrence throughout the entire follow up period [27]. In addition to dormancy reawakening, this may be a consequence of increased intra-tumoural heterogeneity in TNBC. Previous work has shown that primary TNBC can be very clonally diverse among patients with the same stage of cancer and that distinct sub-clones may be capable of maintaining homeostatic balance between clonal populations and thus, enhancing tumour growth [28]. However, intra-tumoural heterogeneity is not commonly considered in clinical practice. Patients are typically treated based on the hormone receptor status of their primary tumour, and metastatic sites (especially the brain) are not always biopsied for biomarker testing. As a result, cancer

5

recurrence may be attributed to treatment resistance of tumours that no longer carry the biomarkers/mutations that were present in the original tumour as well as the presence of dormant cells that are not effectively treated with common chemotherapeutic drugs that target proliferating cells [29]. This calls for a better understanding of cancer cell dormancy, the mechanisms of metastasis, and proactive treatments targeted at eliminating both dormant cancer cells and genetically diverse metastases.

1.2.5 Treatment of breast cancer

Most breast cancer patients will receive some form of surgery throughout the course of their disease. Surgical intervention is performed for a number of reasons including removing cancerous tissue (breast conserving surgery or mastectomy), investigative purposes (lymph node biopsy), breast reconstruction surgery, or to relieve symptoms associated with advanced cancer [30]. Often after breast conserving surgery or mastectomy, radiation therapy will be performed to lower the chance of the cancer returning in the breast and/or at distant sites. Alternatively, radiation therapy may be used to treat metastases in other parts of the body such as the bone or brain [31-32]. For those with hormone receptor positive breast cancers (ER- or PR- positive), hormone therapy is typically recommended as a way to systemically treat cancer cells throughout the body. For these cancers, high estrogen levels help the cancer cells grow and thus, most therapies work by lowering or preventing estrogen from acting on cancer cells. Many breast cancer patients may also receive some form of chemotherapy (i.e., doxorubicin, cisplatin, paclitaxel) throughout the course of their disease. Neoadjuvant chemotherapy is often used to try to shrink a tumour prior to surgery while adjuvant chemotherapy can be used to kill

6

off any remaining cells that may have been left behind during surgery or to lower the risk of cancer recurrence [33].

1.2.6 Treatment of brain metastasis

While many of the above treatment options have shown to be effective in treating breast tumours, current therapies often fail at a time when metastatic disease is already present [34-35]. Treatment of breast cancer brain metastases typically involves a combination of surgery with radio- and/or chemotherapy. Treatment plans often depend on the number of metastases within the brain, whereby patients having multiple lesions typically receive whole brain radiotherapy treatment (WBRT), while surgery and stereotactic radiosurgery (SRS) are feasible options for patients with 1-3 metastases and an otherwise good prognosis. In WBRT, high energy beams are applied to the entire brain in efforts to kill multiple metastases throughout. However, in doing so, there is the potential to damage healthy, non-cancerous tissue and WBRT is associated with cognitive impairment [31-32]. Alternatively, SRS can deliver precise and targeted radiation in fewer, high dose treatments, sparing healthy surrounding tissue [36].

Chemotherapy is often used in addition to WBRT, surgery or SRS to further decrease the chances of cancer recurrence. However, chemotherapy also presents some challenges in treating brain metastases. This is due to the highly selective barrier that surrounds the capillaries within the brain, known as the blood brain barrier (BBB), that allows entry of small molecules (hormones, nutrients etc.) but restricts entry of larger molecules such as toxins or bacteria. As a result, the BBB is typically very good at preventing most

chemotherapeutics from getting into the brain at an effective dose [29, 37]. Previous studies have shown that brain metastasis from breast cancer involves mediators such as cyclooxygenase (COX-2) and epidermal growth factor receptor (EGFR) to enhance extravasation through non-fenestrated capillaries [38]. When a cancer cell extravasates into the brain, the protective cells that make up the surrounding vasculature are compromised, and the BBB becomes known as the blood-tumour barrier (BTB). While the BBB in a healthy brain prevents many therapeutics and contrast agents from diffusing out of the circulation, the BBB/BTB can be disrupted (naturally or drug induced) in metastases resulting in "leaky" tumours that have enhanced permeability [39]. As a result, imaging agents such as gadolinium chelates that do not typically cross the BBB in a healthy brain, have been adapted in the clinic to effectively image permeable tumours with magnetic resonance imaging (MRI). This technique is further discussed in the subsection "MRI of cancer". Unfortunately, relying on BBB/BTB permeability for drug delivery has not been as successful, with common breast cancer drugs such as doxorubicin and trastuzumab showing effective treatment of extracranial metastases but not brain metastases [29, 38]. In recent years, there has been some development in small molecule therapies including capecitabine and lapatinib however, drug uptake has shown to be extremely variable [40].

1.3 Mechanisms of metastasis

Since metastasis is responsible for the majority of cancer related deaths, research has been focused on gaining a better understanding of the underlying mechanisms that regulate cancer metastasis in breast cancer as well as other cancer types. One group of potential mechanisms studied have suggested a relationship between the primary breast tumour and

the growth of secondary tumours in the body [41-67]. This thesis is focused on two of these concepts: concomitant tumour resistance (CTR) whereby the primary tumour restricts the growth of secondary tumours; and concomitant tumour enhancement (CTE) whereby the primary tumour stimulates secondary tumour growth (Figure 1.1).

	Concomitant Tumour Resistance (CTR)	Concomitant Tumour Enhancement (CTE)
Before Surgery	After Surgery	Before Surgery	After Surgery

Metastatic Inhibition — Metastasis — Metastasis — Metastatic Regression
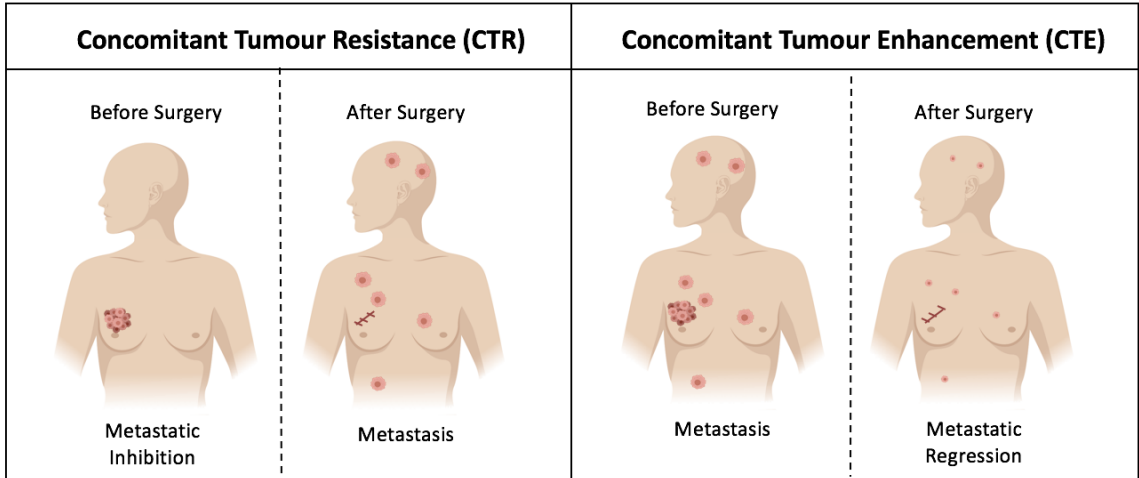
Figure 1.1 Schematic of concomitant tumour resistance vs. concomitant tumour enhancement: CTR occurs when an existing tumour inhibits the growth of secondary tumours throughout the body. As a result, surgical resection of the primary tumour can lead to an abrupt acceleration of distant metastases. Conversely, CTE occurs when an existing primary tumour accelerates the growth of secondary tumours such that surgical resection can lead to regression of metastases.

1.3.1 Concomitant tumour resistance

The phenomenon of concomitant tumour resistance (CTR) occurs when a host bearing a primary tumour inhibits the growth of secondary tumours throughout the body. The clinical relevance of CTR has been observed in patients where the removal of a primary tumour is followed by an abrupt acceleration of residual metastatic disease, suggesting the primary tumour mitigates the continued growth of secondary tumours [41-45]. For example, El Saghir and colleagues reported a case of non-small cell lung cancer whereby the patient, a 43-year old male, had tumour recurrence and accelerated growth following a minor trauma to the skull bone. The authors suggest the unusual growth may be a result of dormant cancer cells that were triggered by a new environment of stimulating factors following injury [45].

A number of hypotheses have been proposed to explain the CTR phenomenon. The first was by Ehrlich and Tyzzer in 1905 who proposed the "athrepsia theory", whereby nutrients that are necessary for secondary tumour growth are consumed by the primary tumour, restricting metastatic progression prior to resection [46]. They first observed this phenomenon in a rat sarcoma model, where the growth of one tumour was able to inhibit the growth of a subsequently injected tumour in the same animal. This theory was later supported by Marie and Clunet, who found a dramatic increase in the frequency of distant visceral metastases when a primary tumour was partially resected in mice in comparison to the number of spontaneous lesions that occur from an intact primary tumour [47]. In 1913, Tyzzer similarly found that Japanese waltzing mouse tumours that were partially excised led to larger metastases compared to control mice not undergoing tumour resection [48]. This study was considered further support for the athrepsia hypothesis.

The immunological hypothesis, coined "concomitant immunity" was originally proposed by Bashford et al., suggesting the growth of a tumour generates an anti-tumour immune response that is capable of preventing the growth of small secondary metastases [49]. This explanation has been supported by numerous preclinical studies using chemically or virally induced immunogenic murine tumour models [50-51]. For example, Franco and colleagues demonstrated in mouse models of bone and breast cancer that there may be two separate peaks of concomitant resistance that occur throughout tumour development. The first peak is caused only by small immunogenic tumours and is associated with a T-cell dependent immune reaction, while the second peak was found to be independent of tumour immunogenicity and caused by the presence of a serum factor in tumour bearing animals [51]. Similarly, Kirstein et al., demonstrated the ability to inhibit the growth of experimental lung metastases through reduction of circulating platelets and tumour associated thrombi in a mouse model of melanoma. Additionally, they restored platelet numbers and were able to re-establish tumour associated thrombus formation and experimental metastasis [52].

In addition, others have suggested the primary tumour can produce anti-proliferative and/or anti-angiogenic molecules into the circulation that indirectly limit the growth of secondary implants [53-57]. For example, O'Reilly et al, have shown that the systemic administration of angiostatin is capable of efficiently blocking neovascularization and thus, the growth of lung metastases in mouse models of cancer [56]. Ruggerio and colleagues also reported that serum from tumour bearing mice exhibited anti-proliferative properties that were

proportional to the size of the primary tumour as well as the relative amount of concomitant resistance observed [57]. The serum factors responsible for inhibition of secondary tumour growth were later identified as meta- and ortho-tyrosine (M- and O-tyrosine), two uncommon tyrosine isomers [58]. Mechanistic studies have since related the anti-tumour effects produced by these tyrosine isomers with inhibition of mitogen-activated protein/extracellular signal-regulated kinase pathway as well as inactivation of STAT3, which may induce a state of cancer cell dormancy [59].

1.3.2 Concomitant tumour enhancement

In addition to CTR, concomitant tumour enhancement (CTE) also exists, whereby the presence of a primary tumour stimulates the growth of secondary tumours [60-62]. This was first observed by Ando and colleagues in studying a mouse model of fibrosarcoma. They found that animals with a growing subcutaneous tumour in the hindlimb developed significantly more lung metastases after secondary inoculation of intravenously injected cancer cells compared to control animals. Interestingly, they found that the growth of an intramuscular tumour at a distant site within the same animals could be prevented by the growth of an existing primary tumour [60]. This is the first reported case of CTR and CTE co-existing in the same animals. Similarly, Janik et al, found a tumour bearing host is first protected and then made more susceptible to the development of metastases. They showed that the number of experimental metastases in the lungs was highest in animals bearing the oldest primary tumour (day 28), however, a moderately sized tumour (day 16) caused fewer metastases than control mice without a primary tumour suggesting an initial inhibitory CTR effect [61].

Other groups have suggested it is the ratio between the size of the primary and the secondary implant that determines whether CTR or CTE occurs. Bruzzo et al., demonstrated that a high ratio between the mass of the primary tumour relative to the mass of the secondary tumour can lead to CTR, while a low ratio can lead to a CTE effect [62]. More recently, McAllister and colleagues showed that osteopontin that is released into the circulation by the primary tumour is capable of promoting the growth of otherwise poorly growing implants. They demonstrated an activation of stromal cell precursors caused by osteopontin, consequently making it easier for cancer cells to recruit them and initiate growth [63]. Additionally, a few clinical cases of CTE have been reported whereby a nephrectomy for renal cell carcinoma is followed by a suspected regression of hepatic and/or pulmonary metastases [64-67].

Despite the relevance of CTR and CTE, clinical evidence of each remains lacking due to the fact that investigation depends on the presence of a growing primary tumour which often does not coincide with clinical treatment plans. Many groups have studied CTR and CTE in various experimental animal models; however, most of these studies have evaluated metastatic lesion growth using endpoint histology. Parts of this thesis focus on the development and application of longitudinal molecular imaging tools to noninvasively study CTR and CTE in mouse models of breast cancer metastasis.

1.3.3 Tumour self-seeding and/or self-homing

As described above, in the traditional theory of metastasis, cancer cells can leave the original tumour and unidirectionally seed metastases in nodes and/or distant sites. However, in 2006, Norton and Massague suggested CTCs that are shed from the primary tumour may also return to, and grow in, the tumour of origin and other established lesions. This fairly new idea of multidirectional metastasis was termed tumour "self-seeding" or "self-homing" and has since been shown to occur in animal models of human breast, colon and melanoma cancer [68-69].
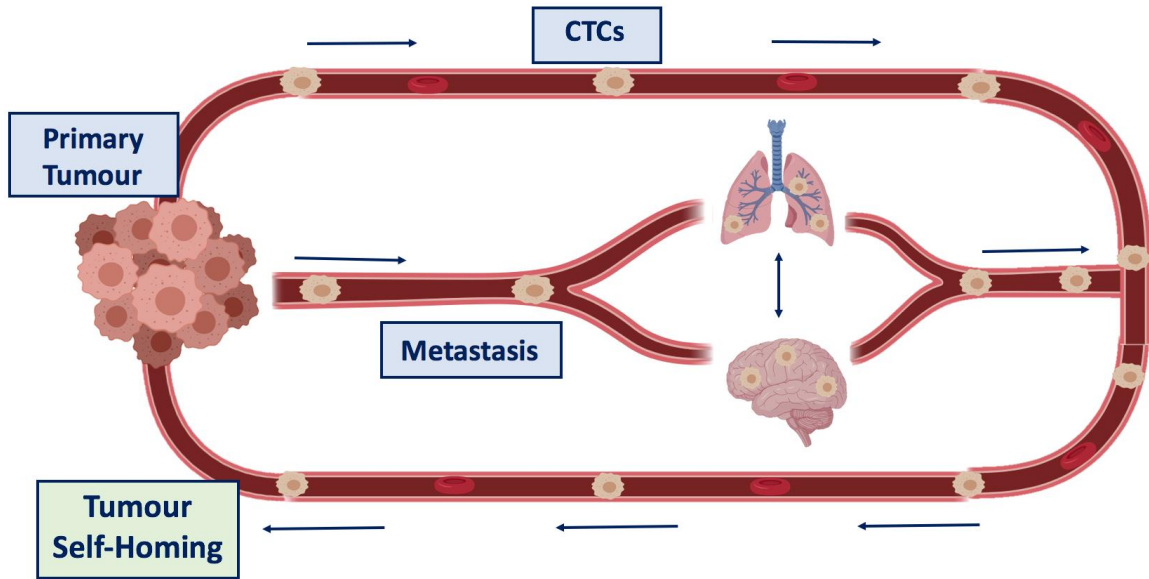
Figure 1.2 Schematic of tumour self-homing: Tumour self-homing or self-seeding occurs when cancer cells are shed from an established tumour (primary or distant metastases) and travel through the circulation to return to and grow at the original tumour site.

The concept of tumour self-homing has been shown to involve both the recruitment capabilities of the original tumour as well as the migratory or "seeding" potential of the CTCs themselves. Firstly, Carmaliet and Jain have shown that the leaky vasculature associated with an established tumour may permit the seeding and survival of cancer cells more easily than at a new site [70]. While one of the rate-limiting steps of unidirectional metastasis is adaptation to distant organs, CTCs may not need further adaptation to initiate growth in the microenvironment of their source tumour. This hypothesis was further supported by work from Kim and colleagues showing that tumours can become efficiently seeded by CTCs derived from a secondary tumour implant, distant metastases, or systemic injection, suggesting the primary tumour has the ability to recruit CTCs. They further attributed these findings to the cytokines, IL-6 and IL-8, that are produced by the primary tumour and act as chemoattractants to efficiently recruit CTCs [69]. More recently, Vilalta and colleagues have shown that radiation of tumour cells produces granulocyte-macrophage colony stimulating factor (GM-CSF) that can also act to enhance the recruitment of CTCs to irradiated sites. They provide evidence suggesting radiation induced cancer self-homing may act as a potential mechanism for cancer recurrence and, similar to studies by Kim et al., they show consistently increased self-homing irrespective of the route of CTC administration [71].

The characteristics of CTCs that contribute to their ability to self-home have also been studied. Kim et al., found that markers such as collagenase-1, fascin-1, and CXCL1 act as mediators of CTC infiltration into mammary tumours. The expression of these genes in primary breast tumours has been associated with priming of cancer cells for the seeding of

the lungs and brain as well as with relapse in cancer patients. Additionally, they provide evidence that tumour self-homing selects for a highly aggressive population of CTCs whereby, metastatic cell populations are more efficient seeders than their respective parental populations [69].

1.3.4 Development of Self-Homing Cancer Cells as Therapeutic Vectors

In the last decade, several groups have begun to exploit the self-homing properties of cancer cells in order to use them as delivery vehicles for anti-cancer therapeutics [72-76]. In 2004, Raykov et al, demonstrated the remarkable ability of metastatic cancer cells to efficiently deliver oncolytic viruses to pre-established tumours. Using a rat model, they show hepatoma cells can be successfully employed as H-1 parvovirus carriers to target and treat lung metastases [72]. Another group similarly showed that the limitations associated with systemic delivery of oncolytic virus can be overcome by using "carrier" cancer cells to shield virions from defense mechanisms. Furthermore, they showed that when cancer cells carrying oncolytic virus are administered systemically, lung tumour burden is significantly reduced and survival is prolonged compared to naked virion injection [73].

Other groups have engineered self-homing tumour cells to express suicide genes which can transfer death signals to neighbouring cancer cells in pre-established lesions. Freeman and colleagues demonstrated this by engineering cancer cells to express the gene for herpes simplex virus thymidine kinase (HSV-TK). HSV-TK expressing cells are sensitive to killing by the drug ganciclovir (GCV) and also produce a "bystander effect" whereby adjacent HSV-TK negative cells can be killed. Freeman et al., showed that survival was

significantly improved when mice with a pre-existing HSV-TK negative tumour were injected with secondary HSV-TK positive cells followed by GCV treatment compared to control animals [74]. Garcia-Castro et al., also showed the value of using suicide gene therapy in treating metastatic disease. They transduced human breast (MDA-MB-231) or prostate (PC3) cell lines to express the therapeutic gene cytosine deaminase (CD) that converts the nontoxic pro-drug, 5 fluorocytosine (5'FC) into an active chemotherapeutic 5-fluorouracil (5'FU). They found that tumour-bearing mice injected with CD expressing cells and treated with the pro-drug had significantly less primary tumour burden as well as fewer metastases in both the lungs and kidneys compared to control mice [75]. These suicide genes offer a unique opportunity to use cancer cells as a therapeutic carrier by enabling both a safety mechanism of self-induced toxicity as well as an efficacious bystander effect capable of killing surrounding non-engineered cells.

Dondossola et al., have also shown that cancer cells can be engineered to express therapeutic genes that influence the tumour microenvironment. In a 2016 study, they showed that cancer cells can be genetically modified to produce and release tumour necrosis factor (TNF), a cytokine known to have anti-tumour effects. In mouse models, they successfully demonstrated that cancer cells engineered to express TNF homed to pre-established tumours, released TNF and consequently damaged the neovascular endothelium and induced cancer cell death [76].

While the current approaches have shown promise, there are some important limitations of using cancer cells to carry therapeutic cargo. First and foremost, is the safety aspect of

introducing new cancer cells into a subject in efforts to treat them. The use of suicide genes has significantly improved the safety profile of using cancer cells as delivery vehicles however, further development is needed to enable noninvasive monitoring of their long-term fate *in vivo*. Likewise, there is a need for imaging tools to determine the self-homing efficiency of engineered CTCs prior to implementing them as a therapeutic carrier. Parts of this thesis explore the use of imaging reporter genes to enable noninvasive imaging to be used to evaluate the self-homing efficiency and therapeutic efficacy of engineered CTCs *in vivo*.

1.4   MRI of Cancer

Non-invasive imaging technologies can be used for a number of reasons along the course of cancer progression. This can include screening and early detection methods (e.g., mammography), visualizing the spread and severity of disease, as well as monitoring for signs of cancer recurrence (active surveillance). Furthermore, imaging technologies play a pivotal role in cancer treatment including for biopsy needle guidance, surgical/radiotherapy treatment planning and evaluating responses to most therapies. A number of different imaging modalities are used both clinically and pre-clinically for imaging cancer, including optical imaging, ultrasound (US), photoacoustic imaging (PAI), computed tomography (CT), magnetic resonance imaging (MRI), single photon emission computed tomography (SPECT), and positron emission tomography (PET). Among these, MRI is one of the most employed technologies as it provides excellent soft tissue contrast, high resolution images, and uses non-ionizing radiation [77].

In the clinic, conventional MRI can be used to assess a variety of tumour characteristics including tumour size, tumour perfusion, cancer cellularity, tumour metabolism and tumour pH [78-85]. Among these, contrast enhanced T1-weighted MRI is considered the most accurate detection method for clinical brain tumours. In preclinical cancer models, MRI cell tracking can be employed as a way to track specific cell populations *in vivo*. Cellular MRI enables longitudinal tracking of both transplanted and endogenous cell populations depending on the strategy that is used to label cells with contrast agents such as iron (iron-based cellular MR) or perfluorocarbons (Fluorine-19 MR) [23, 24, 86, 87]. This thesis utilizes iron-based cellular MRI for tracking metastatic breast cancer cells in the mouse brain.

1.4.1 Basic principles of MRI

In conventional MRI, an image is generated from hydrogen atoms (^{1}H or protons) within the tissues of our body, predominantly water and fat. A large magnetic field (B_0) causes the protons to align within the body and a radiofrequency (RF) transmitter is applied to excite protons which results in a change in the orientation of the net magnetization vector. When the RF pulse is turned off, the protons dephase and relax back to equilibrium, generating energy that creates detectable MR signal [88]. Since cancerous tissues have different relaxation rates (T1 and T2) compared to healthy tissues they can generate different contrast, and therefore, anatomical MRI is a valuable tool to visualize changes in size, spread and composition of tumours throughout the body [89].

1.4.2 Generating contrast

In an MR image, the most common forms of contrast weightings are dependent on proton density (PD), spin-lattice relaxation time (T1), or spin-spin relaxation time (T2). In PD-weighted images, regions of hyperintensity represent regions with high numbers of hydrogen atoms, while T1-weighted contrast is reflective of how long it takes protons to realign with B_0 after an RF pulse is applied. Tissues that have a short T1 such as fat appear bright in a T1-weighted image, while tissues with a long T1 like water or air appear dark. Contrast in T2-weighted images depends on the rate of dephasing (spin-spin relaxation) in a particular voxel following an RF excitation. In T2-weighted images, tissues with a long T2, like fluids, appear bright, while tissues with a short T2, such as fat, appear dark [88]. Contrast agents can be used to further enhance signal in an area of interest by shortening the T1 or T2 times of surrounding tissues. Paramagnetic agents such as gadolinium (Gd) and manganese (Mn) based agents act to shorten T1, resulting in bright or hyperintense areas in a T1-weighted image, while superparamagnetic agents such as iron-oxides shorten T2, resulting in signal loss or hypointense regions [88-90]. This thesis involves the use of iron-oxide nanoparticles.

RF coils are applied to transmit and/or receive the energy necessary to acquire an MR image. There are two types of coil configurations categorized as either surface or volume coils, whereby the size, geometry and efficiency of the coil impacts the amount of signal that can be acquired. While surface coils have shown to have increased sensitivity, the signal drops off significantly the farther away from the coil one tries to image. In contrast, volume coils enable a more uniform signal that is independent of depth, making them the

more common choice for imaging deep tissues such as the brain [91-92]. In this thesis, we used a custom-built insert gradient as well as a birdcage mouse head RF volume coil to allow for preclinical imaging on a clinical MR system. This unique MR setup is discussed further in Chapters 2 and 3.

The two main types of pulse sequences that can be used to generate an MR image are called spin echo (SE) and gradient echo (GE) sequences. SE imaging typically produces high quality images; however, can take relatively long to acquire. Alternatively, GE sequences have shorter TR and take less time to acquire but are susceptible to field inhomogeneities. In GE sequences, the signal intensity in the image is T2* weighted, which includes signal loss due to T2 relaxation as well as magnetic field inhomogeneity [88].

In our lab, we have used the balanced steady state free precession (bSSFP) iron-sensitive MR pulse sequence to detect iron labeled cells (also known as FIESTA, TrueFISP and balanced FFE) [88]. bSSFP is a type of GE sequence with T2/T1-weighted image contrast. It is one of the most signal to noise ratio (SNR) efficient sequences as a result of refocusing the magnetization at the end of each repetition time (TR), generating a "steady state" in both the transverse and longitudinal planes [88]. Using a bSSFP sequence, iron labeled cells appear as regions of signal void.

1.4.3 Iron-based Cellular MRI

To increase the conspicuity of cells with MRI, one can label them with iron-oxide nanoparticles, which are available in different sizes including micron sized iron oxide

(MPIO) nanoparticles (diameter $\geq$ 1um), superparamagnetic iron oxides (SPIOs; ~ 50-150 nm in diameter), and ultra-small superparamagnetic iron oxides (USPIOs; $\leq$ 50 nm in diameter) [93-94]. There are two main techniques to label cells with iron-oxide nanoparticles. Firstly, cells can be pre-labeled in culture with MPIOs, SPIOs, or USPIOs prior to transplantation into a subject (Figure 1.3). Many cultured cell types readily take up these iron oxides by simple coincubation [86,90,95,96] or can be encouraged to internalize iron particles using transfection agents, electroporation or magnetofection [98-100]. Labelling cells with MPIO offers substantially more iron content per cell and thus, improves MR detectability to low cell numbers, even single cells [86,90,95,96,101]. Alternatively, SPIOs and USPIOs can also be injected systemically for *in vivo* or "in situ" cellular labeling. In this instance, these particles are preferentially taken up by phagocytic cells of the reticuloendothelial system including macrophages and other immune cell types [87]. MPIO particles are limited to preclinical studies as their polymer matrix composition is not biodegradable. Ferumoxytol (Feraheme), a USPIO used for iron replacement therapy is being investigated for off-label use as an MR contrast agent [102-103].

Figure 1.3 **Ex vivo** *iron labeling of cancer cells: Cancer cells can be labeled ex vivo with*

| *Ex Vivo* Cell Labeling | Intracardiac Injection | *In Vivo* Imaging |
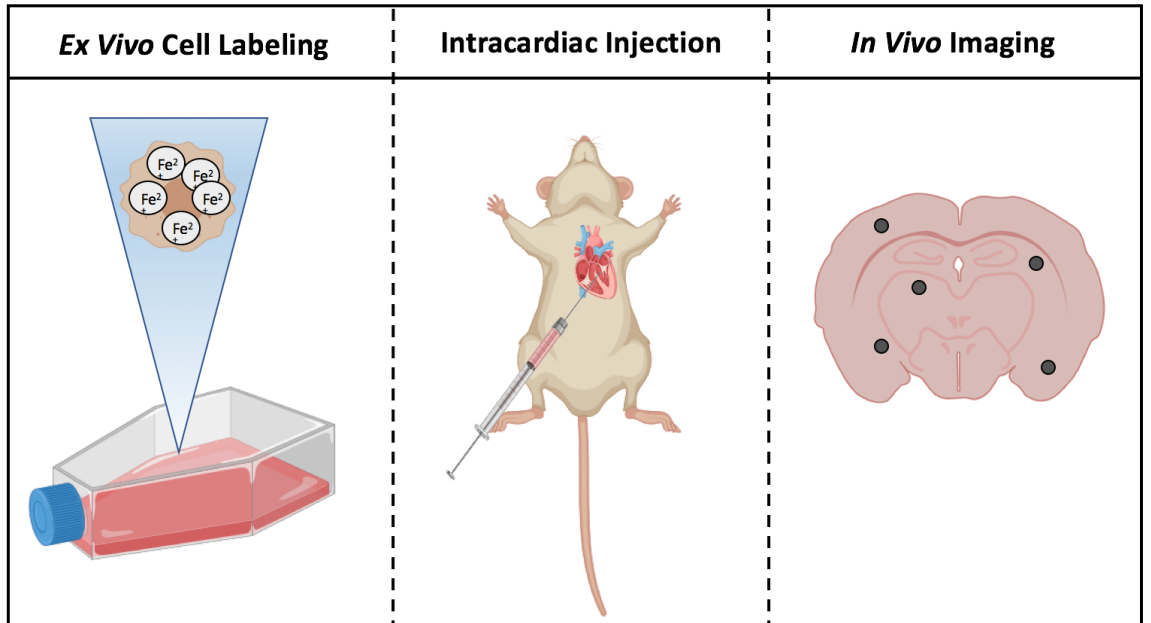
iron oxides prior to intracardiac injection into the beating mouse heart. These cells will

travel through the circulation and arrest in distant organs including the brain where

they can be visualized with cellular MRI.

Iron based cellular MRI has been applied to a number of different disease models to track different cell types including immune cells, stem cells, pancreatic islets and cancer cells [23, 24, 87, 97, 105-118]. While in its early years, there were concerns about iron having an effect on cell function, very few detrimental effects have been observed. However, in 2011, Rohani and colleagues found that MPIO labeled dendritic cells showed differences in activation and maturation compared to unlabeled cells, though they reported no difference in cell viability [111]. Importantly, previous work has shown that MPIO and SPIO labeling of cancer cells does not cause significant changes in cell viability, proliferation, apoptosis or metastatic efficiency [23, 86, 105].

1.4.4 Cellular MRI of Cancer

Cellular MRI has shown to be an invaluable tool to study the fate of cancer cells *in vivo*, enabling noninvasive monitoring of both proliferative and nonproliferative cells [23, 24, 87, 96, 104-105, 114-115]. The main advantage of using iron-based cellular MRI to track cancer cells *in vivo*, is that it has high sensitivity. In 2006, Heyn et al., demonstrated for the first time, that solitary cells can be visualized in the mouse brain using *in vivo* cellular MRI. By labelling a macrophage cell line in culture with SPIO, they demonstrated an iron loading efficiency of approximately 60 picograms of iron per cell and consequently, were able to visualize single iron-labeled cells in the brain with MRI [105]. Similarly, they showed this technique was also possible with metastatic breast cancer cells such that, tracking the fate of individual cancer cells in the brain was feasible. In these studies, MDA-MB-231BR cells, a highly brain metastatic variant of human MDA-MB-231 cells, were loaded with iron, injected into the left ventricle of mice, and monitored with bSSFP-based

cellular MRI over time. After a month of tumour development, they showed that cells that had arrested in the brain had three distinct cell fates: 1) signal voids that were present after injection but disappear for the remainder of the study, deemed "transient", 2) proliferative cancer cells that appear as signal voids after injection and later appear as areas of hyperintensity, representing tumours, and 3) nonproliferative cancer cells that retain their iron label over time, deemed "dormant". Furthermore, they confirmed these findings by co-registering discrete signal voids (representing iron-labeled cells) in MR images with confocal microscopy images confirming the ability to visualize individual fluorescent cells with cellular MRI [86].

1.4.5 Limitations of cellular MRI

The application of cellular MRI to study disease has shown tremendous growth in the last decade. However, there has not been nearly as much work done in tracking cancer cells compared to other cell populations such as immune, stem or therapeutic cell types [98-100, 106-112, 115-117]. This is likely attributed to the iron label being diluted during rapid cancer cell division, leading to a limited timeframe for detection of proliferating cancer cells. Since the iron is stored in the cell body, the amount of iron-oxide will get divided between daughter cells through each cell division, or lost to the extracellular environment, until eventually there is no longer enough iron per cell to be detected with MRI. This, however, can also be beneficial in exploiting non-dividing cell populations, for example, dormant cancer cells that are not actively dividing and will retain their iron label over time [23, 24].

Iron-based cellular MRI also lacks specificity compared to other cell tracking techniques. While the iron creates a distinct void and optimal contrast in anatomies such as the brain, there are many naturally dark or hypointense areas throughout the body that are difficult to distinguish from iron labeled cells, such as the lungs. In some cases, this limitation can be avoided by acquiring a pre-and post-iron image and determining the change in signal between the two acquisitions [87]. In addition, past studies have shown that iron oxides have a high R1 relaxivity that can lead to an increase in signal by using a T1-weighted pulse sequence with minimum echo time. Positive MR contrast has been demonstrated with both USPIOs and SPIOs and is becoming a common application for anatomies that naturally appear dark [118-120].

Another important limitation that needs to be considered when using iron-based cellular MRI is the difficulty in quantification [120-121]. Since the void created by the iron oxide is larger than the cell itself, it is quite difficult to determine the exact number of cells in a given area when many cells are present. Regardless, a number of different approaches have been developed to try to estimate the number of cell present by indirectly measuring the amount of signal loss produced by iron labeled cells. This has included counting the number of signal voids, measuring the percentage of black pixels in a particular region of interest, or measuring the amount of contrast produced by iron labeled cells known as fractional signal loss [87, 109, 120-123]. Others have also used T2/T2* relaxation rates to estimate the amount of iron in a given area [124].

1.5   Reporter gene imaging

In the last few decades, there has been significant progress in developing methods to stably track proliferating cell populations *in vivo* over time. Unlike iron-oxide nanoparticles that can be diluted through cell division, reporter gene based tracking involves engineering cells to stably express a transgene that makes a product that can be detected with a particular imaging modality. The inserted transgene will be passed to daughter cells, and thus will permit longitudinal tracking of both dividing and non-dividing cell populations. Reporter genes have most commonly been used for fluorescence microscopy studies of cultured cells. In 2008, the discovery and development of fluorescent reporter genes (GFP and its variants) was recognized with the chemistry Nobel prize to Drs. Roger Tsien, Osamu Shimomura and Martin Chalfie. However, in the last few decades with the development of whole-body small animal scanners, optical fluorescence and bioluminescence imaging (BLI) reporters have been used extensively for tracking various cell types in small animal models [125-131]. Moreover, since the early 2000s there has been many reporter genes developed for tracking of cells with clinically-relevant imaging modalities such as PET, SPECT, MRI and photoacoustic imaging [132-138]. Importantly, a landmark paper recently described the use of reporter gene-based tracking of therapeutic T cells in glioma patients, marking the first use of reporter genes to track a cellular therapeutic in the clinic [139].

1.5.1 Bioluminescence imaging

Bioluminescence imaging (BLI) was first described by Contag and colleagues in 1995 [140]. Since then, many groups have used BLI to track a variety of cell types in small animal models. BLI has been adapted by cancer researchers as a valuable cell tracking tool due to its high sensitivity, relatively low cost, and ability to differentiate between dead and viable cell populations. Furthermore, BLI has high specificity as the signal acquired is a direct measure of engineered cells [131].

To track transplanted cells, cultured cells are typically engineered to stably express a luciferase transgene, most commonly *Firefly* luciferase (FLuc) or *Renilla* luciferase (RLuc), which reacts with the corresponding substrate (D-luciferin for *Firefly* luciferase or h-coelenterazine for *Renilla* luciferase). The enzymatic reaction produces light as a product of enzyme-based oxidation of the substrate and photons are collected by a highly-sensitive cooled charge coupled device (CCD) camera that converts photons into electrons after striking silicon wafers [141] (Figure 1.4). To generate an image, CCD cameras spatially encode the intensity of incident photons into electrical charge patterns and the signal generated can be overlaid onto a white light image, an X-Ray or CT image for anatomical reference. *Firefly* luciferase is most commonly used since the reaction also requires ATP and oxygen to produce light and as a result, only viable cells produce signal. It also has a red-shifted emission spectrum compared to *Renilla* luciferase so allows for better light penetration out of deep tissues [130-131]. In 2004, Bhaumik and colleagues showed that *Firefly* and *Renilla* luciferase have orthogonal substrates, demonstrating a lack of cross

reactivity and thus, the ability to monitor the fate of two engineered cell populations independently in the same animal [142]. In this thesis, we use both a red-shifted *Firefly* luciferase from *Luciola italica* and *Renilla* luciferase 8 from *Renilla reniformis* to track two different cancer cell populations *in vivo* using longitudinal BLI.
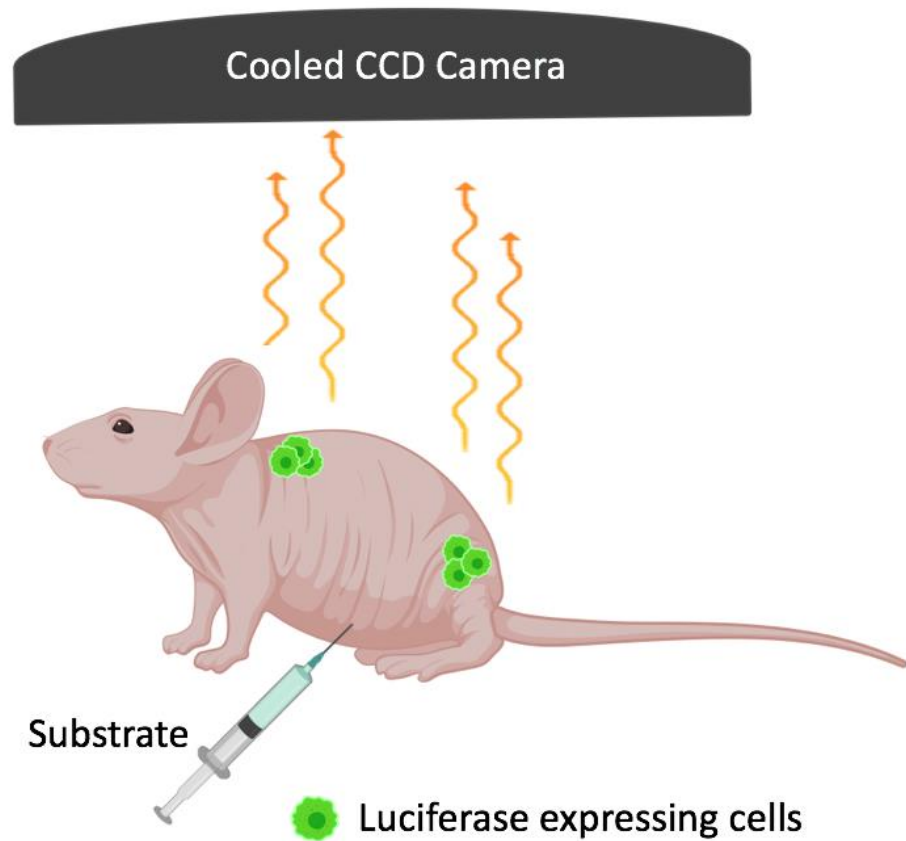
Figure 1.4 Schematic of BLI protocol: Luciferase expressing cells are implanted into the animal prior to imaging. Engineered cells will react with the corresponding substrate and produce light as a product of oxidation. Emitted photons are collected by a cooled CCD camera.

1.5.2 BLI of cancer models

Perhaps the most commonly used application of BLI is to track the growth, dissemination, and viability of cancer cells in mice during both normal tumour progression and in response to treatment(s). Tumour burden of subcutaneous tumours has traditionally been monitored using manual caliper measurements. While this technique is quick and relatively inexpensive, it however does not account for areas of necrosis or edema within the tumour, which can accumulate upon treatment without any change in tumour size. Additionally, caliper measurements are only relevant to subcutaneous tumour models, which are not as relevant as orthotopic models, and caliper measurements are also not a feasible option for assessing metastatic tumour burden in deep tissues. As an alternative, many groups have shown that BLI can provide rapid throughput measurements of tumour growth and regression in animals over time [143-157]. For example, Jenkins and colleagues demonstrate the ability to monitor both primary and spontaneous metastatic tumour burden noninvasively with BLI. They implanted luciferase expressing colon cancer cells subcutaneously into mice that consistently produce metastases in both the lungs and lymph nodes. They were able to show correspondence between the frequency and size of metastases detected *in vivo* with *ex vivo* imaging of excised lungs and lymph nodes [148].

BLI has also been employed to evaluate treatment response *in vivo*. Rehemtulla et al., showed that the survival of FLuc expressing gliosarcoma cells in rats can be noninvasively monitored following treatment with 1,3-bis (2-chloroethyl)-1-nitrosourea (BCNU). They compared serial anatomical MRI tumour volume measurements with BLI photon flux over time and demonstrate that both modalities yielded similar results, supporting the use of

BLI as an effective tool for evaluating treatment response in living subjects [152]. Furthermore, in recent years it has been shown that FLuc BLI may be superior to other imaging modalities in assessing treatment response since it can uniquely provide information on cellular viability. While imaging modalities including MRI and CT are useful for measuring changes in tumour volume following treatment, cancer cell death may occur much sooner than changes in tumour size. Thus, the high sensitivity of BLI as well as the ability to quantify only viable tumour cells, makes it a powerful complementary tool to evaluate early changes in tumour viability. In breast cancer models, BLI has been used extensively to evaluate the treatment effects of numerous therapies including but not limited to combretastatin A4 phosphate, trastuzumab, lapatinib, rapamycin, and cyclophosphamide [149-150]

1.5.3 Limitations of BLI

While BLI has significant value as a noninvasive cell tracking technology, it has some important limitations to consider. The most detrimental in studying a cancer metastasis model is the depth limitation. While BLI signal can be overlaid onto a brightfield or X-Ray image for anatomical reference, it is a two-dimensional modality and does not offer the 3-dimensional high-resolution images that MRI can [131, 132, 143]. Currently, there is not a way to determine the depth of a tumour within the body based on the signal acquired with most BLI systems. In recent years, three dimensional (3D) BLI systems have been developed with the capability to overlay BLI signal with a 3D CT image set; however, due to the increased cost, time required to acquire such a dataset, and the ability to image only one animal at a time during 3D image collection, these systems have not been readily used.

BLI signal relies on the availability of substrate and in the case of FLuc, other co-factors such as ATP, magnesium, and oxygen. This can produce a false negative effect in the areas that the substrate cannot easily accumulate into such as the brain, or in tumours that may have compromised vasculature, again limiting access to substrate [147]. In addition, since BLI is a measure of light output there can be an attenuation effect such that light is absorbed or scattered by tissue, with hemoglobin being the main absorber of light within tissues [141]. This can be seen in subcutaneous cancer models whereby scabbing forms on the surface of large tumours and BLI signal is seen surrounding the scab [152]. This is more confounding in metastatic models, due to the inability to readily visualize areas of hemorrhage or necrosis that may be limiting light output. Thus, the use of several imaging modalities together may overcome the inherent limitations of using only a single modality.

1.5.4 Benefits of multimodality imaging

As mentioned, multimodality imaging may provide a solution to overcome the limitations of using each modality independently. Technologies such as BLI and PET are commonly used to collect information on the biology of cells or groups of cells (their viability, tumour metabolism, etc.) while modalities such as MRI and CT can provide valuable anatomical information. Additionally, cellular or molecular MRI can enable visualization of molecular biomarkers, cells, or therapeutic drugs. By using a combination of these technologies, we can improve and expand the scope of information available regarding a certain disease state [146, 151, 157].

In a recent study by Le et al., the utility of combing BLI with multiparametric MRI (mpMRI) was investigated for characterizing an orthotopic rat model of glioblastoma. They showed that T1 and T2 weighted MR measurements of tumour volume continued to increase up until endpoint (day 18), while on average, BLI signal peaks at day 11 and then plateaued. Immunostaining confirmed the presence of both necrotic and hypoxic regions in the majority of tumours, which is likely responsible for the decrease in BLI signal at later timepoints [151]. Similarly, Fritz and colleagues demonstrated the advantages of combing micro CT with BLI to evaluate early tumour-bone interaction in a mouse model of tumour osteolysis. They found luciferase expressing tumour cells could be detected with BLI as early as two days post implantation while the first clinical signs did not appear until three weeks post injection. Furthermore, BLI measurements revealed an exponential increase in BLI signal after two weeks, while micro CT measurements suggested a decrease in bone density and bone mineral content as early as seven days [157]. These studies highlight the value in using complementary modalities to obtain a more complete picture of disease progression in preclinical models. Parts of this thesis explore the advantages of combining cellular MRI and BLI in tracking the fate of metastatic cancer cells *in vivo*.

1.6   Purpose of Thesis

This thesis uses MRI and BLI techniques to study the mechanisms that influence breast cancer metastasis. The objectives of this work were to develop a multimodality imaging model to better visualize the stages of the metastatic cascade noninvasively using a mouse model of breast cancer brain metastasis and to apply these imaging tools to study two

potential mechanisms of cancer metastasis: concomitant tumour enhancement and tumour self-homing.

1.6.1 Hypotheses

1. Bioluminescence imaging will complement our current iron-based cellular MRI tools by allowing rapid throughput screening and longitudinal measurements of cell viability.

2. In an immune competent mouse model of breast cancer metastasis, the presence of a primary tumour will inhibit the growth of metastasis.

3. Systemically administered CTCs will preferentially home to and effectively treat previously established disseminated breast cancer metastases throughout the mouse body.

In Chapter 2, cellular and conventional MRI techniques were combined with serial BLI to noninvasively track the fate of single breast cancer cells from their initial arrest in the brain to the formation of overt tumours. This chapter was published in Scientific Reports *(Parkins KM, et al., "A multimodality imaging model to track viable cancer cells from single arrest to metastasis" Scientific Reports. October 2016).*

In Chapter 3, we used MRI and BLI to investigate the impact of a primary breast tumour on the growth of secondary tumours in an immune competent mouse model of breast cancer metastasis. In this work, we demonstrated concomitant tumour enhancement whereby the presence of the primary tumour stimulated the growth of secondary metastases both in and

outside of the brain. This work was published in Scientific Reports *(Parkins KM, et al., "Multimodality cellular and molecular imaging of the impact of a primary tumor on metastatic growth in a syngeneic mouse model of breast cancer brain metastasis" Scientific Reports. June 2018)*

In Chapter 4, using dual-luciferase BLI, we demonstrated the ability of experimental CTCs to efficiently home to and treat primary tumours and disseminated breast cancer metastases throughout the mouse body. This chapter is in preparation for submission.

1.7 References

1. Institute, N. C. SEER Stat Fact Sheets: Female Breast Cancer. *SEER* Survival by Stage (2012).

2. Lee, Y. T. Breast carcinoma: pattern of metastasis at autopsy. *J. Surg. Oncol.* **23,** 175–180 (1983).

3. Allred, DC., Wu, Y., Mao, S., Nagtegaal, ID., Lee, S., Perou, CM., et al. Ductal carcinoma in situ and the emergence of diversity during breast cancer evolution. Clin Cancer Res; 14(2):370–378. (2008).

4. Shipitsin, M., Campbell, LL., Argani, P., Weremowicz, S., Bloushtain-Qimron, N., Yao, J., et al. Molecular definition of breast tumor heterogeneity. Cancer Cell. ; 11(3):259–273. (2007).

5. Allred, DC., Harvey, JM., Berardo, M., Clark, GM. Prognostic and predictive factors in breast cancer by immunohistochemical analysis. Mod Pathol. 11(2):155–168. (1998).

6. Sorlie, T., Perou, CM., Tibshirani, R., Aas, T., Geisler, S., Johnsen, H., et al. Gene expression patterns of breast carcinomas distinguish tumor subclasses with clinical implications. Proc Natl Acad Sci U S A. 98(19):10869–10874. (2001).

7. Herschkowitz, JI., Simin, K., Weigman, VJ., Mikaelian, I., Usary, J., Hu, Z., et al. Identification of conserved gene expression features between murine mammary carcinoma models and human breast tumors. Genome Biol. 8(5):R76. (2007).

8. Prat, A., Parker, JS., Karginova, O., Fan, C., Livasy, C., Herschkowitz, JI., et al. Phenotypic and molecular characterization of the claudin-low intrinsic subtype of breast cancer. Breast Cancer Res. 12(5):R68. (2010).

9. Parker, JS., Mullins, M., Cheang, MC., Leung, S., Voduc, D., Vickery, T., et al. Supervised risk predictor of breast cancer based on intrinsic subtypes. J Clin Oncol. 27(8):1160–1167. (2009).

10. Perou, CM., Sorlie, T., Eisen, MB., van de Rijn, M., Jeffrey, SS., Rees, CA., et al. Molecular portraits of human breast tumours. Nature. 406(6797):747–752. (2000).

11. Martin, AM., Cagney, DN., Catalano, PJ., Warren, LE., Bellon, JR., Punglia, RS., Claus, EB., Lee, EQ., Wen, PY., Haas-Kogan, DA., Alexander, BM., Lin, NU., Aizer, AA. Brain Metastases in Newly Diagnosed Breast Cancer: A Population-Based Study. JAMA Oncol. 3(8):1069–77. (2017).

12. Wen, PY., Loeffler, JS. Brain metastases. Curr Treat Options Oncol. 1(5):447–58. (2000).

13. Jin, J., Gao, Y., Zhang, J., Wang, L., Wang, B., Cao, J., & Wang, Z. Incidence, pattern and prognosis of brain metastases in patients with metastatic triple negative breast cancer. *BMC cancer*, *18*(1), 446. (2018).

14. Lin, NU. Brain metastases in HER2-positive breast cancer. Lancet Oncol. **14**:185–6. (2013).

15. MacDonald, I. C., Groom, A. C. & Chambers, A. F. Cancer spread and micrometastasis development: Quantitative approaches for in vivo models. *BioEssays* **24,** 885–893 (2002).

16. Luzzi, K. J., MacDonald, I. C., Schmidt, E. E., Kerkvliet, N., Morris, V. L., Chambers, A. F., & Groom, A. C. Multistep nature of metastatic inefficiency: dormancy of solitary cells after successful extravasation and limited survival of

early micrometastases. *The American journal of pathology*, *153*(3), 865-873. (1998).

17. Chambers, A. F. *et al.* Steps in tumor metastasis: new concepts from intravital videomicroscopy. *Cancer Metastasis Rev.* **14,** 279–301 (1995).

18. Kienast Y, von Baumgarten L, Fuhrmann M, Klinkert WEF, Goldbrunner R, Herms J, et al. Real-time imaging reveals the single steps of brain metastasis formation. Nat Med. 16:116–22. (2010).

19. Barkan, D., Chambers, AF. ß1-Integrin: A Potential Therapeutic Target in the Battle against Cancer Recurrence. Clin Cancer Res. 17:7219–23. (2011).

20. Ghajar, CM., Peinado, H., Mori, H., Matei, IR., Evason, KJ., Brazier, H., et al. The perivascular niche regulates breast tumour dormancy. Nat Cell Biol. 15:807–17. (2013).

21. Sosa, MS., Bragado, P., Debnath, J., Aguirre-Ghiso, JA. Regulation of Tumor Cell Dormancy by Tissue Microenvironments and Autophagy. Adv Exp Med Biol 734:73–89. (2013).

22. Naumov, GN., MacDonald, IC., Weinmeister, PM., Kerkvliet, N., Nadkarni, KV., Wilson, SM., et al. Persistence of Solitary Mammary Carcinoma Cells in a Secondary Site: A Possible Contributor to Dormancy. Cancer Res. 62. (2002).

23. Foster, PJ., Dunn, EA., Karl, KE., Snir, JA., Nycz, CM., Harvey, AJ., et al. Cellular Magnetic Resonance Imaging: In Vivo Imaging of Melanoma Cells in Lymph Nodes of Mice. Neoplasia. 10:207–16. (2008).

24. Economopoulos, V., Chen, Y., McFadden, C., Foster, PJ. MRI Detection of Nonproliferative Tumor Cells in Lymph Node Metastases Using Iron Oxide Particles in a Mouse Model of Breast Cancer. Transl Oncol. 6:347–54. (2013).

25. Townson, JL., Ramadan, SS., Simedrea, C., Rutt, BK., MacDonald, IC., Foster, PJ., et al. Three-dimensional imaging and quantification of both solitary cells and metastases in whole mouse liver by magnetic resonance imaging. Cancer Res 69:8326–31. (2009).

26. Demicheli, R., Abbattista, A., Miceli, R., Valagussa, P., & Bonadonna, G. Time distribution of the recurrence risk for breast cancer patients undergoing mastectomy: further support about the concept of tumor dormancy. *Breast cancer research and treatment*, *41*(2), 177-185. (1996).

27. Dent, R. *et al.* Triple-Negative Breast Cancer: Clinical Features and Patterns of Recurrence. *Clin. Cancer Res.* **13 ,** 4429–4434 (2007).

28. Marusyk, A., Tabassum, DP., Altrock, PM., Almendro, V., Michor, F., Polyak, K. Non-cell-autonomous driving of tumour growth supports sub-clonal heterogeneity. [Research Support, N.I.H., Extramural Research Support, Non-U.S. Gov't Research Support, U.S. Gov't, Non-P.H.S.]. Nature. 514(7520):54–58. (2014).

29. Naumov, GN., Townson, JL., MacDonald, IC., Wilson, SM., Bramwell, VH., Groom, AC., et al. Ineffectiveness of doxorubicin treatment on solitary dormant mammary carcinoma cells or late-developing metastases. Breast Cancer Res Treat 82:199–206. (2003).

30. Goldhirsch, A., Glick, J. H., Gelber, R. D., Coates, A. S., & Senn, H. J. Meeting highlights: international consensus panel on the treatment of primary breast cancer. *Journal of Clinical Oncology*, *19*(18), 3817-3827. (2001).

31. Viani, GA., Castilho, MS., Salvajoli, JV., Pellizzon, ACA., Novaes, PE., Guimarães, FS., et al. Whole brain radiotherapy for brain metastases from breast cancer: estimation of survival using two stratification systems. BMC Cancer. 7:53–61. (2007).

32. Mahmoud-Ahmed, AS., Suh, JH., Lee, S-Y., Crownover, RL., Barnett, GH. Results of whole brain radiotherapy in patients with brain metastases from breast cancer: a retrospective study. Int J Radiat Oncol Biol Phys. 54:810–7. (2002).

33. Early Breast Cancer Trialists' Collaborative Group. Effects of chemotherapy and hormonal therapy for early breast cancer on recurrence and 15-year survival: an overview of the randomised trials. *The Lancet*, *365*(9472), 1687-1717. (2005)

34. Stemmler, HJ., Kahlert, S., Siekiera, W., Untch, M., Heinrich, B., Heinemann V. Characteristics of patients with brain metastases receiving trastuzumab for HER2 overexpressing metastatic breast cancer. Breast. 15:219–25. (2006)

35. Lockman, PR., Mittapalli, RK., Taskar, KS., Rudraraju, V., Gril, B., Bohn, KA., et al. Heterogeneous blood-tumor barrier permeability determines drug efficacy in experimental brain metastases of breast cancer. Clin Cancer Res. 16. (2010).

36. Kocher, M., Soffietti, R., Abacioglu, U., Villà, S., Fauchon, F., Baumert, BG., et al. Adjuvant whole-brain radiotherapy versus observation after radiosurgery or surgical resection of one to three cerebral metastases: Results of the EORTC 22952-26001 study. J Clin Oncol. 29:134–41. (2011).

37. Stemmler, H-J., Schmitt, M., Willems, A., Bernhard, H., Harbeck, N., Heinemann, V. Ratio of trastuzumab levels in serum and cerebrospinal fluid is altered in HER2-positive breast cancer patients with brain metastases and impairment of bloodbrain barrier. Anticancer Drugs. 18:23–8. (2007).

38. Li, J. Brain Metastasis of Breast Cancer: Crossing the Blood-brain Barrier. *Journal of Applied Clinical Pathology (JACP).* (2017).

39. Connell, JJ., Chatain, G., Cornelissen, B., Vallis, KA., Hamilton, A., Seymour, L., et al. Selective permeabilization of the blood-brain barrier at sites of metastasis. J Natl Cancer Inst. 105:1634–43. (2013).

40. Morikawa, A., Peereboom, DM., Thorsheim, HR., Samala, R., Balyan, R., Murphy, CG,et al. Capecitabine and lapatinib uptake in surgically resected brain metastases from metastatic breast cancer patients: a prospective study. Neuro Oncol. 1–7. (2014).

41. Lange, PH., Hekmat, K., Bosl, G., Kennedy, BJ., Fraley, EE. Accelerated growth of testicular cancer after cytoreductive surgery, Cancer 45. 1498–1506. (1980).

42. Qadri, SS., Wang, JH., Coffey, JC., Alam, M., O'Donnell, A., Aherne, T., Redmond, HP. Can surgery for cancer accelerate the progression of secondary tumors within residual minimal disease at both local and systemic levels? Ann Thorac. Surg. 80. 1046–1050. (2005).

43. Peeters, CF., de Waal, RM., Wobbes, T., Ruers, TJ. Metastatic dormancy imposed by the primary tumor: does it exist in humans? Ann Surg. Oncol. 15. 3308–3315. (2008).

44. Beecken, WD., Engl, T., Jonas, D., Blaheta, RA. Expression of angiogenesis inhibitors in human bladder cancer may explain rapid metastatic progression after radical cystectomy, Int. J. Mol. Med. 23. 261–266. (2009).

45. El Saghir, NS., Elhajj, II., Geara, Hourani, MH. Trauma-associated growth of suspected micrometastases, B.M.C. Cancer. 5; 94. (205).

46. Ehrlich, P. Experimentelle Carcinomstudien an Mausen, in: P. Ehrlich (Ed.), Arbeiten aus dem Koiglichen Institut fur Experimentelle Therapie zu Frankfurt/ AM, Gustav Fischer, Jena, Germany, pp. 77–103. (1906).

47. Marie P, Clunet J. Fre´ quences des me´ tastases visce´ rales chez les souris cance´ reuses apre` s ablation chirurgicale de leur tumeur. Bull Assoc Francx pour l'e´ tude du cancer. 3: 19–23. (1910).

48. Tyzzer, EE. Factors in the production and growth of tumor metastases. J Med Res. 23: 309–332. (1913).

49. Bashford, E., Murray, J., Haaland, M. General results of propagation of malignant new growths, in: E. Bashford (Ed.), Third Scientific Report on the Investigation of the Imperial Cancer Research Fund, vol. 3, Taylor and Francis, London, pp. 262–268. (1908).

50. Franco, M., Bustuoabad, OD., di Gianni, PD., Goldman, A., Pasqualini, CD., Ruggiero, RA. A serum-mediated mechanism for concomitant resistance shared byimmunogenic and non-immunogenic tumours, Br. J. Cancer. 74;178–186. (1996).

51. North, RJ. The murine antitumor immune response and its therapeutic Manipulation, Adv. Immunology. 35;89–155. (1984).

52. Kirstein, J. M., Hague, M. N., McGowan, P. M., Tuck, A. B., & Chambers, A. F.

    Primary melanoma tumor inhibits metastasis through alterations in systemic

    hemostasis. *Journal of Molecular Medicine*, *94*(8), 899-910. (2016).

53. Gorelik, E. Concomitant tumor immunity and the resistance to a second tumor

    Challenge, Adv. Cancer Res. 39; 71–120. (1983).

54. Ruggiero, RA., Bustuoabad, OD., Cramer, P., Bonfil, RD., Pasqualini, CD.

    Correlation between seric antitumor activity and concomitant resistance in

    mice bearing non-immunogenic tumors, Cancer Res. 50;7159–7165. (1990).

55. DeWys, WD. Studies correlating the growth rate of a tumor and its metastases

    and providing evidence for tumor-related systemic growth-retarding factors,

    Cancer Res. 32;374–379. (1972).

56. O'Reilly, MS., Holmgren, L., Shing, Y., Chen, C., Rosenthal, RA., Moses, M.,

    Lane, WS., Cao, Y., Sage, EH., Folkman, J. Angiostatin: a novel angiogenesis

    inhibitor that mediates the suppression of metastases by a Lewis lung carcinoma,

    Cell. 79; 315–328. (1994).

57. Ruggiero, RA., di Gianni, PD., Franco, M., Bustuoabad, OD. Resistencia

    concomitante antitumoral, Medicina (Bs.As.) 56; 57–64. (1996).

58. Ruggiero, RA., Bruzzo, J., Chiarella, P., di Gianni, P., Isturiz, MA., Linskens, S.,

    Speziale, N., Meiss, RP., Bustuoabad, OD., Pasqualini, CD. Tyrosine isomers

    mediate the classical phenomenon of concomitant tumor resistance, Cancer

    Res. 71;7113–7124. (2011).

59. Ruggiero, RA., Bruzzo, J., Chiarella, P., Bustuoabad, OD., Meiss, RP.,

    Pasqualini, CD. Concomitant tumor resistance: the role of tyrosine isomers in the

mechanisms of metastases control, Cancer Res. 72;1043–1050. (2012).

60. Ando, K., Hunter, N., Peters, L. Immunologically nonspecific enhancement of artificial lung metastases in tumor-bearing mice, Cancer Immun. Immunother. 6 ;151–156. (1979).

61. Janik, P., Bertram, J., Szaniawska, B. Modulation of lung tumor colony formation by a subcutaneously growing tumor, J. Natl. Cancer Inst. 66 ;1155–1158. (1981).

62. Bruzzo, J., Chiarella, P., Meiss, RP., Ruggiero, RA. Biphasic effect of a primary tumor on the growth of secondary tumor implants, J. Cancer Res. and Clin. Oncol. 136; 1605–1615. (2010).

63. McAllister, SS., Gifford, AM., Greiner, AL., Kelleher, SP., Saelzler, MP., Ince, TA., Reinhardt, F., Harris, LN., Hylander, BL., Repasky, EA., Weinberg, RA. Systemic endocrine instigation of indolent tumor growth requires osteopontin, Cell 133; 994–1005. (2008).

64. Vizel, M., Oster, MW., Austin, JH. Spontaneous regression of a pulmonary metastasis after nephrectomy for renal cell carcinoma, J. Surg. Oncol. 12;175–180. (1979).

65. Lokick, J. Spontaneous regression of metastatic renal cancer. Case report and literature review, Am. J. Clin. Oncol. 20; 416–418. (1997).

66. Wyczolkowski, M., Klima, W., Bieda, W., Walask, K. Spontaneous regression of hepatic metastases after nephrectomy and mastectomy of renal cell carcinoma, Urol. Int. 66 ; 119–120. (2001).

67. Lekanidi, K., Vlachou, PA., Morgan, B., Vasanthan, S. Spontaneous regression of metastatic renal cell carcinoma: case report, J. Med. Case Reports. 1;89. (2007)

68. Norton, L., Massague, J. Is cancer a disease of self-seeding? Nat Med. 12:875–878. (2006).

69. Kim, MY., et al. Tumor self-seeding by circulating cancer cells. Cell 139(7):1315–1326. (2009).

70. Carmeliet, P., Jain, RK.. Angiogenesis in cancer and other diseases. Nature. 407:249–257. (2000).

71. Vilalta, M., Rafat, M., Giaccia, A. J., & Graves, E. E. Recruitment of circulating breast cancer cells is stimulated by radiotherapy. *Cell reports*, *8*(2), 402-409. (2014).

72. Raykov, Z., Balboni, G., Aprahamian, M., Rommelaere, J. Carrier cell-mediated delivery of oncolytic parvoviruses for targeting metastases. Int. J. Cancer 109, 742–749 (2004).

73. Power, AT., Wang, J., Falls, TJ., Paterson, JM., Parato, KA., Lichty, BD., Stojdl, DF., Forsyth, PA., Atkins, H. J. C. Bell, Carrier cell-based delivery of an oncolytic virus circumvents antiviral immunity. Mol. Ther. 15, 123–130 (2007).

74. Freeman, SM., Abboud, CN., Whartenby, KA., Packman, CH., Koeplin, DS., Moolten, FL., Abraham, GN. The "bystander effect": Tumor regression when a fraction of the tumor mass is genetically modified. Cancer Res. 53, 5274–5283 (1993).

75. Garcia-Castro, J., Mart.nez-Palacio, J., Lillo, R., Garc.a-S.nchez, F., Alemany, R., Madero, L., Bueren, JA., Ram.rez, M. Tumor cells as cellular vehicles to deliver gene therapies to metastatic tumors. Cancer Gene Ther. 12, 341–349 (2005).

76. Dondossola, E., Dobroff, AS., Marchi, S., Card.-Vila, M., Hosoya, H., Libutti, SK., Corti, A., Sidman, RL., Arap, W., Pasqualini, R.Self-targeting of TNF-releasing cancer cells in preclinical models of primary and metastatic tumors. Proc. Natl. Acad. Sci. U.S.A. 113, 2223–2228 (2016).

77. Law, M., Cha, S., Knopp, EA., Johnson, G., Arnett, J., Litt, AW. High-Grade Gliomas and Solitary Metastases%: Differentiation by Using Perfusion and Proton Spectroscopic MR Imaging. Neuroradiology. 222:715–21. (2002).

78. Bello, E., Colella, G., Scarlato, V., Oliva, P., Berndt, A., Valbusa, G., et al. E-3810 Is a Potent Dual Inhibitor of VEGFR and FGFR that Exerts Antitumor Activity in Multiple Preclinical Models. 71:1396–406. (2011).

79. Budde, MD., Gold, E., Jordan, EK., Frank, JA. Differential microstructure and physiology of brain and bone metastases in a rat breast cancer model by diffusion and dynamic contrast enhanced MRI. Clin Exp Metastasis. 29:51–62. (2012).

80. Moffat, BA., Chenevert, TL., Meyer, CR., Mckeever, PE., Hall, DE., Hoff, BA., et al. The Functional Diffusion Map: An Imaging Biomarker for the Early Prediction of Cancer Treatment Outcome. Neoplasia. 8:259–67. (2006).

81. Ross, BD., Chenevert, TL., Kim, B., Ben-Yoseph, O. Magnetic Resonance Imaging and Spectroscopy: Application to Experimental Neuro-Oncology. Q Magn Reson Biol Med. 1:89–106. (1994).

82. Rodrigues, TB., Serrao, EM., Kennedy, BWC., Hu, D., Kettunen, MI., Brindle, KM. Magnetic resonance imaging of tumor glycolysis using hyperpolarized 13Clabeled glucose. Nat Med. 20:93–8. (2014).

83. Mallett, CL., Lim, H., Thind, K., Chen, Y., Ribot, EJ., Martinez, F., et al. Longitudinal Anatomical and Metabolic MRI Characterization of Orthotopic Xenograft Prostate Tumors in Nude Mice. J Magn Reson Imaging. 856:848–56. (2014).

84. McVicar, N., Li, AX., Meakin, SO., Bartha, R. Imaging chemical exchange saturation transfer (CEST) effects following tumor-selective acidification using lonidamine.NMR Biomed. 28:566–75. (2015).

85. Ouwerkerk, R., Jacobs, MA., Macura, KJ., Wolff, AC., Stearns, V., Mezban, SD., et al. Elevated tissue sodium concentration in malignant breast lesions detected with non-invasive 23Na MRI. Breast Cancer Res Treat. 106:151–60. (2007).

86. Heyn, C., Ronald, JA., Ramadan, SS., Snir, JA., Barry, AM., MacKenzie, LT., et al. In vivo MRI of cancer cell fate at the single-cell level in a mouse model of breast cancer metastasis to the brain. Magn Reson Med. 56:1001–10. (2006).

87. Makela, A. V., Gaudet, J. M., & Foster, P. J. Quantifying tumor associated macrophages in breast cancer: a comparison of iron and fluorine-based MRI cell tracking. *Scientific reports*, *7*, 42109. (2017).

88. McRobbie, DW., Moore, EA., Graves, MJ., Prince, MR. MRI From Picture to Proton. 2nd edition. New York: Cambridge University Press. (2007).

89. Taylor, D. G., & Bore, C. F. A review of the magnetic resonance response of biological tissue and its applicability to the diagnosis of cancer by NMR radiology. *Journal of Computed Tomography*, *5*(2), 122-134. (1981).

90. Heyn, C., Bowen, CV., Rutt, BK., Foster, PJ. Detection threshold of single SPIO labeled cells with FIESTA. Magn Reson Med. 53:312–20. (2005).

91. Fukushima, E. Radiofrequency Coils for NMR: A peripatetic history of their twists and turns. In: RF Coils for MRI. 9-15. (2012).

92. Zanche, N De. Birdcage Volume Coil Design. In: RF Coils for MRI. 123-136. (2012).

93. Modo, M., Hoehn, M., Bulte, JWM. Cellular MR imaging. Mol Imaging. 4:143–64. (2005)

94. Korchinski, DJ., Taha, M., Yang, R., Nathoo, N., Dunn, JF. Iron Oxide as an MRI Contrast Agent for Cell Tracking. Magn Reson Insights. 8:15–29. (2015).

95. Foster-Gareau, P., Heyn, C., Alejski, A., Rutt, BK. Imaging Single Mammalian Cells With a 1.5T Clinical MRI Scanner. Magn Reson Med. 49:968–71. (2003).

96. Shapiro, EM., Sharer, K., Skrtic, S., Koretsky, AP. In Vivo Detection of Single Cells by MRI. Magn Reson Med. 55:242–9. (2006).

97. Arbab, AS., Yocum, GT., Kalish, H., Jordan, EK., Anderson, SA., Khakoo, AY., et al. Efficient magnetic cell labeling with protamine sulfate complexed to ferumoxides for cellular MRI. Blood. 104:1217-24. (2004).

98. Walczak, P., Kedziorek, DA., Gilad, AA., Lin, S., Bulte, JWM. Instant MR Labeling of Stem Cells Using Magnetoelectroporation. 774:769–74. (2005).

99. Siegers, GM., Ribot, EJ., Keating, A., Foster, PJ. Extensive expansion of primary human gamma delta T cells generates cytotoxic effector memory cells that can be labeled with Feraheme for cellular MRI. Cancer Immunol Immunother. 62:571–83. (2013).

100.   Kedziorek, DA., Kraitchman, DL. Superparamagnetic Iron Oxide Labeling of Stem Cells for MRI Tracking and Delivery in Cardiovascular Disease. Methods Mol Biol. 660:171–83. (2010).

101.   Shapiro, EM., Koretsky, AP. Micron-Sized Iron Oxide Particles (MPIOs) for Cellular Imaging: More Bang for the Buck. In: Bulte JWM, Modo MMJ, editors. Nanoparticles Biomed. Imaging, Springer New York; p.141–61. (2008).

102.   Bashir, MR., Bhatti, L., Marin, D., Nelson, RC. Emerging Applications for Ferumoxytol as a Contrast Agent in MRI. J Magn Reson Imaging. 41:884–98. (2015).

103.   Hamilton, B., Nesbit, G., Dosa, E., Gahramanov, S., Rooney, B., Nesbit, E., et al. Comparative analysis of ferumoxytol and gadoteridol enhancement using T- and T2-weighted MRI in neuroimaging. AJR Am J Roentgenol. 197:981–8. (2011).

104.   Ribot, EJ., Martinez-Santiesteban, FM., Simedrea, C., Steeg, PS., Chambers, AF., Rutt, BK., et al. In vivo single scan detection of both iron-labeled cells and breast cancer metastases in the mouse brain using balanced steady-state free precession imaging at 1.5 T. J Magn Reson Imaging. 34:231–8. (2011).

105.   Heyn, C., Ronald, JA., Mackenzie, LT., MacDonald, IC., Chambers, AF., Rutt, BK., et al. In vivo magnetic resonance imaging of single cells in mouse brain with optical validation. Magn Reson Med. 55:23–9. (2006).

106.   Hinds, KA., Hill, JM., Shapiro, EM., Laukkanen, MO., Silva, AC., Combs, CA., et al. Highly efficient endosomal labeling of progenitor and stem cells with

large magnetic particles allows magnetic resonance imaging of single cells. Blood. 102:867–72. (2003).

107.   Ahrens, ET., Xu, H., Genove, G., Morel, PA. Receptor-Mediated Endocytosis of Iron-Oxide Particles Provides Efficient Labeling of Dendritic Cells for In Vivo MR Imaging. Magn Reson Med. 49:1006–13. (2003).

108.   Shapiro, EM., Medford-Davis, LN., Fahmy, TM., Dunbar, CE., Koretsky, AP. Antibody-mediated cell labeling of peripheral T cells with micron-sized iron oxide particles (MPIOs) allows single cell detection by MRI. Contrast Media Mol Imaging. 2:147–53. (2007).

109.   Dekaban, GA., Snir, J., Shrum, B., de Chickera, S., Willert, JC., Merrill, M., et al. Semiquantitation of Mouse Dendritic Cell Migration In Vivo Using Cellular MRI. J Immunother. 32:240–51. (2009).

110.   Zhang, X., Chickera, SNDE., Willert, C., Economopoulos, V., Noad, J., Rohani, R., et al. Cellular magnetic resonance imaging of monocyte-derived dendritic cell migration from healthy donors and cancer patients as assessed in a scid mouse model. Cytotherapy. 13:1234–48. (2011).

111.   Rohani, R., de Chickera, SN., Willert, C., Chen, Y., Dekaban, GA., Foster, PJ. In vivo cellular MRI of dendritic cell migration using micrometer-sized iron oxide (MPIO) particles. Mol Imaging Biol. 13:679–94. (2011).

112.   de Chickera, SN., Willert, C., Mallet, C., Foley, R., Foster, PJ., Dekaban, GA. Cellular MRI as a suitable, sensitive non-invasive modality for correlating in vivo migratory efficiencies of different dendritic cell populations with subsequent immunological outcomes. Int Immunol. 24:29–41. (2012).

113.   Bernas, LM., Foster, PJ., Rutt, BK. Imaging Iron-Loaded Mouse Glioma Tumors With bSSFP at 3T. Magn Reson Med. 64:23–31. (2010).

114.   Magnitsky, S., Roesch, A., Herlyn, M., Glickson, JD. In Vivo and Ex Vivo MR Imaging of Slowly Cycling Melanoma Cells. Magn Reson Med. 66:1362–73. (2011).

115.   Berkova, Z., Jirak, D., Zacharovova, K., Kriz, J., Lodererova, A., Girman, P., et al. Labeling of Pancreatic Islets With Iron Oxide Nanoparticles for In Vivo Detection With Magnetic Resonance. Transplantation. 85:155–9. (2008).

116.   Barnett, BP., Arepally, A., Karmarkar, PV., Qian, D., Gilson, WD., Walczak, P., et al. Magnetic resonance-guided, real-time targeted delivery and imaging of magnetocapsules immunoprotecting pancreatic islet cells. Nat Med.13. (2007).

117.   Evgenov, NV., Medarova, Z., Dai, G., Bonner-Weir, S., Moore, A. In vivo imaging of islet transplantation. Nat Med. 12:144–8. (2006).

118.   Wei, H., Bruns, O. T., Kaul, M. G., Hansen, E. C., Barch, M., Wiśniowska, A., & Cordero, J. M. Exceedingly small iron oxide nanoparticles as positive MRI contrast agents. *Proceedings of the National Academy of Sciences*, *114*(9), 2325-2330. (2017).

119.   Li, Z., Yi, P. W., Sun, Q., Lei, H., Li Zhao, H., Zhu, Z. H., & Lu, G. Q. Ultrasmall water-soluble and biocompatible magnetic iron oxide nanoparticles as positive and negative dual contrast agents. *Advanced Functional Materials*, *22*(11), 2387-2393. (2012).

120. Liu, W., Frank, JA. Detection and quantification of magnetically labeled cells by cellular MRI. Eur J Radiol. 70(2):258-264. (2009).

121. Kim, JH., Jin, SM., Oh, SH., et al. Counting small hypointense spots confounds the quantification of functional islet mass based on islet MRI. Am J Transplant. 12(5):1303-1312. (2012).

122. Long, CM., van Laarhoven, HWM., Bulte, JWM., Levitsky, HI. Magnetovaccination as a novel method to assess and quantify dendritic cell tumor antigen capture and delivery to lymph nodes. Cancer Res. 69(7):3180-3187. (2009).

123. Sundstrom, T., Daphu, I., Wendelbo, I., et al. Automated tracking of nanoparticle labeled melanoma cells improves the predictive power of a brain metastasis model. Cancer Res. 73(8):2445-2456. (2013).

124. Mills, PH., Hitchens, TK., Foley, LM., et al. Automated detection and characterization of SPIO-labeled cells and capsules using magnetic field perturbations. Magn Reson Med. 67(1):278-289. (2012).

125. van der Horst, G., van Asten, J. J., Figdor, A., van den Hoogen, C., Cheung, H., Bevers, R. F., & van der Pluijm, G. Real-time cancer cell tracking by bioluminescence in a preclinical model of human bladder cancer growth and metastasis. *European urology*, *60*(2), 337-343. (2011).

126. Christian, N. A., Benencia, F., Milone, M. C., Li, G., Frail, P. R., Therien, M. J., & Hammer, D. A. In vivo dendritic cell tracking using fluorescence lifetime imaging and near-infrared-emissive polymersomes. *Molecular Imaging and Biology*, *11*(3), 167-177. (2009).

127.   Fowler, M., Virostko, J., Chen, Z. et al. Assessment of pancreatic islet mass after islet transplantation using in vivo bioluminescence imaging. Transplantation 79(7):768–776. (2005).

128.   Xiong, T., Zhang, Z., Liu, BF. et al. In vivo optical imaging of human adenoid cystic carcinoma cell metastasis. Oral Oncol 41(7):709–715. (2005).

129.   Shah, K. & Weissleder, R. Molecular optical imaging: applications leading to the development of present day therapeutics. NeuroRx 2, 215-225 (2005).

130.   Contag, P. R., Olomu, I. N., Stevenson, D. K. & Contag, C. H. Bioluminescent indicators in living mammals. Nat. Med. 4, 245-247 (1998).

131.   Contag, CH., Spilman, SD., Contag, PR., Oshiro, M., Eames, B., et al. Visualizing gene expression in living mammals using a bioluminescent reporter. *Pho- tochem. Photobiol.* 66:523–31. (1997).

132.   Mettler, F. A. Jr. & Guiberteau, M. J. Essentials of nuclear medicine imaging 5th Edition (Saunders/ Elsevier, Philadelphia). (2006).

133.   Gambhir, S. S. et al. A mutant herpes simplex virus type 1 thymidine kinase reporter gene shows improved sensitivity for imaging reporter gene expression with positron emission tomography. Proc. Natl Acad. Sci. USA 97, 2785-2790 (2000).

134.   Massoud, T. F., Singh, A. & Gambhir, S. S. Noninvasive molecular neuroimaging using reporter genes: part II, experimental, current, and future applications. AJNR Am. J. Neuroradiol. 29, 409-418 (2008).

135.   Massoud, T. F., Singh, A. & Gambhir, S. S. Noninvasive molecular neuroimaging using reporter genes: part I, principles revisited. AJNR Am. J. Neuroradiol. 29, 229-234 (2008).

136.   Serganova, I., Mayer-Kukuck, P., Huang, R. & Blasberg, R. Molecular imaging: reporter gene imaging. Handb. Exp. Pharmacol. 185, 167-223 (2008).

137.   Nyström, N. N., Hamilton, A. M., Xia, W., Liu, S., Scholl, T. J., & Ronald, J. A. Longitudinal Visualization of Viable Cancer Cell Intratumoral Distribution in Mouse Models Using Oatp1a1-Enhanced Magnetic Resonance Imaging. *Invest Radiol*. (2019).

138.   Qin, C., Cheng, K., Chen, K., Hu, X., Liu, Y., Lan, X., & Su, X. Tyrosinase as a multifunctional reporter gene for Photoacoustic/MRI/PET triple modality molecular imaging. *Scientific reports*, *3*, 1490. (2013).

139.   Keu, K. V., Witney, T. H., Yaghoubi, S., Rosenberg, J., Kurien, A., Magnusson, R., & Brown, C. Reporter gene imaging of targeted T cell immunotherapy in recurrent glioma. *Science translational medicine*, *9*(373), eaag2196. (2017).

140.   Contag, C. H., Contag, P. R., Mullins, J. I., Spilman, S. D., Stevenson, D. K., & Benaron, D. A. Photonic detection of bacterial pathogens in living hosts. *Molecular microbiology*, *18*(4), 593-603. (1995).

141.   Sadikot, R. T., & Blackwell, T. S. Bioluminescence imaging. *Proceedings of the American Thoracic Society*, *2*(6), 537-540. (2005).

142.   Bhaumik, S., & Gambhir, S. S. Optical imaging of Renilla luciferase reporter gene expression in living mice. *Proceedings of the National Academy of Sciences*, *99*(1), 377-382. (2002).

143.   Frangioni, J. V. New technologies for human cancer imaging. *Journal of clinical oncology*, *26*(24), 4012. (2008).

144.   Tempany, C. M., Zou, K. H., Silverman, S. G., Brown, D. L., Kurtz, A. B., & McNeil, B. J. Staging of advanced ovarian cancer: comparison of imaging modalities—report from the Radiological Diagnostic Oncology Group. *Radiology*, *215*(3), 761-767. (2000).

145.   Prescher, J. & Contag, C. Guided by the light: visualizing biomolecular processes in living animals with bioluminescence. *Curr Opin Chem Biol.* **14**, 80-89 (2010).

146.   Jost, S. C. *et al*. Measuring brain tumor growth: combined bioluminescence imaging–magnetic resonance imaging strategy. *Mol Imaging.* **8**, 7290-2009 (2009).

147.   Koberle, M. *et al*. Monitoring Disease Progression and Therapeutic Response in a Disseminated Tumor Model for Non-Hodgkin Lymphoma by Bioluminescence Imaging. *Mol Imaging.* **14**, 400-413 (2015).

148.   Jenkins, D. E., Oei, Y., Hornig, Y. S., Yu, S. F., Dusich, J., Purchio, T., & Contag, P. R. Bioluminescent imaging (BLI) to improve and refine traditional murine models of tumor growth and metastasis. *Clinical & experimental metastasis*, *20*(8), 733-744. (2003).

149.   Zhao, D., Richer, E., Antich, P. P., & Mason, R. P. Antivascular effects of combretastatin A4 phosphate in breast cancer xenograft assessed using dynamic bioluminescence imaging and confirmed by MRI. *The FASEB Journal*, *22*(7), 2445-2451. (2008).

150.   Kodack, D. P., Chung, E., Yamashita, H., Incio, J., Duyverman, A. M., Song, Y., & Goel, S. Combined targeting of HER2 and VEGFR2 for effective treatment of HER2-amplified breast cancer brain metastases. *Proceedings of the National Academy of Sciences*, *109*(45), E3119-E3127. (2012).

151.   Le, T. N., Lim, H., Hamilton, A. M., Parkins, K. M., Chen, Y., Scholl, T. J., & Ronald, J. A. Characterization of an orthotopic rat model of glioblastoma using multiparametric magnetic resonance imaging and bioluminescence imaging. *Tomography*, *4*(2), 55. (2018).

152.   Rehemtulla, A., Stegman, L. D., Cardozo, S. J., Gupta, S., Hall, D. E., Contag, C. H., & Ross, B. D. Rapid and quantitative assessment of cancer treatment response using in vivo bioluminescence imaging. *Neoplasia*, *2*(6), 491-495. (2000).

153.   Lamid-Ochir, O., Nakajima, T., Miyazaki, M., Zhang, X., Erdene, K., Murakami, T., & Tsushima, Y. Bioluminescence Image as a Quantitative Imaging Biomarker for Preclinical Evaluation of Cryoablation in a Murine Model. *Journal of Vascular and Interventional Radiology*, *29*(7), 1034-1040. (2018).

154.   Shi, J., Udayakumar, T. S., Xu, K., Dogan, N., Pollack, A., & Yang, Y. Bioluminescence tomography guided small-animal radiation therapy and tumor

response assessment. *International Journal of Radiation Oncology* Biology* Physics*, *102*(4), 848-857. (2018).

155. Li, L., Xiang, D., Ye, J., Du, Y., Chen, X., & Tian, J. Evaluation of chemotherapeutic response of temozolomide in orthotopic glioma using bioluminescence tomography. In *Medical Imaging 2018: Biomedical Applications in Molecular, Structural, and Functional Imaging*(Vol. 10578, p. 105780Y). International Society for Optics and Photonics. (2018).

156. Tao, K., Fang, M., Alroy, J., & Sahagian, G. G. Imagable 4T1 model for the study of late stage breast cancer. *BMC cancer*, *8*, 228. doi:10.1186/1471-2407-8-228. (2008).

157. Fritz, V., Louis-Plence, P., Apparailly, F., Noël, D., Voide, R., Pillon, A., & Jorgensen, C. Micro-CT combined with bioluminescence imaging: a dynamic approach to detect early tumor–bone interaction in a tumor osteolysis murine model. *Bone*, *40*(4), 1032-1040. (2007).

Chapter 2

2   A multimodality imaging model to track viable breast cancer cells from single arrest to metastasis in the mouse brain

Purpose*:* Cellular MRI involves sensitive visualization of iron-labeled cells *in vivo* but cannot differentiate between dead and viable cells. Bioluminescence imaging (BLI) measures cellular viability, and thus we explored combining these tools to provide a more holistic view of metastatic cancer cell fate in mice. **Methods:** Human breast carcinoma cells stably expressing *Firefly* luciferase were loaded with iron particles, injected into the left ventricle, and BLI and MRI were performed on days 0, 8, 21 and 28. **Results:** The number of brain MR signal voids (i.e., iron-loaded cells) on day 0 significantly correlated with BLI signal. Both BLI and MRI signals decreased from day 0 to day 8, indicating a loss of viable cells rather than a loss of iron label. Total brain MR tumour volume on day 28 also correlated with BLI signal. **Conclusion**: Overall, BLI complemented our sensitive cellular MRI technologies well, allowing us for the first time to screen animals for successful injections, and, in addition to MR measures of cell arrest and tumor burden, provided longitudinal measures of cancer cell viability in individual animals. We predict this novel multimodality molecular imaging framework will be useful for evaluating the efficacy of emerging anti-cancer drugs at different stages of the metastatic cascade.

2.1 Introduction

Breast cancer is the second most common cancer in both American and Canadian women[1]. The majority of breast cancer-associated mortality is due to metastasis; the dissemination of cancer cells from the primary tumour to other parts of the body, rather than the presence of a primary tumour. Therefore, the clinical need to better understand and prevent breast cancer metastasis is high.

A number of *in vivo* imaging modalities can be used to measure tumour size, location and metastatic burden such as positron emission tomography (PET), ultrasound (US), magnetic resonance imaging (MRI), computed tomography (CT), single photon emission computed tomography (SPECT) and optical imaging. Among these, MRI continues to be one of the most employed modalities for studying cancer due to its high resolution and soft tissue contrast without the use of ionizing radiation[2].

Cellular MRI is an established tool to non-invasively visualize and track specific cell populations *in vivo*. This technique uses iron oxide nanoparticles to label cells in culture or in situ, enhancing their detectability by MRI[3]. The presence of intracellular iron causes a distortion in the magnetic field which leads to signal loss in iron-sensitive images[3]. Typically, millions of intracellular ultrasmall iron oxide particles (USPIOs) are needed to be detected by MRI, however Shapiro et al. were the first to show that single, micron-sized iron particles (MPIOs) can be loaded into cells and allow for single cell detection[4]. Wu et al. showed that these particles can also be used to label *in situ* for successful tracking of immune cells[5]. Although the amount of iron within these particles is significantly more

than in the USPIOs, many cellular MRI studies have found that there is minimal impact on cell function or phenotype[6-8]. While we and others have used cellular MRI extensively in various scenarios, this technology has its limitations. First, is its limited ability to definitively differentiate between dead and viable cells. Furthermore, when a cell dies the iron label may be transferred to phagocytic bystander cells leading to false positive imaging results[9]. This was demonstrated by Winter *et al.* who injected both dead and living iron-labeled human epicardium-derived cells (EPDCs) into the infarcted heart of immune compromised mice[10]. The aim was to distinguish viable from dead cells by following the hypointensity of signal voids over time. They found that a difference could not be seen between signal intensity, void number, size or localization of live cells that migrate to the infarcted area, and dead cells that are taken up by macrophages or other bystander cells[10]. Thus, a complementary imaging tool to cellular MRI that could provide direct measures of cellular viability over time would enable a more complete picture of cell fate in preclinical models.

Similar to cellular MRI technology, bioluminescence imaging (BLI) with the reporter *Firefly* luciferase (FLuc) has been adapted by many researchers as a valuable cell tracking tool in preclinical models of cancer metastasis. The intensity and location of the bioluminescent signal can provide insights into the biology of neoplastic cells, with respect to their biodistribution and proliferative potential. FLuc BLI requires adenosine triphosphate (ATP) as a cofactor and so the BLI signal is directly proportional to the number of viable cells at a particular location[11]. This has been shown to provide corresponding information to tumour volume measurements with more structure-based

imaging such as CT or MRI. This can be crucial in models of treatment response where the size or morphology of a tumour may not change but the amount of viable tissue within the tumour will be altered[12]. Similarly, when a tumour naturally becomes necrotic as it becomes larger, volume measurements can overestimate the number of viable cancer cells[12]. Furthermore, BLI is a highly sensitive technology that can enable the visualization and quantification of cancer cells at a stage where tumours are not yet detectable by these other relatively less affordable and less sensitive imaging modalities[13]. Given its high sensitivity and ability to provide measures of cellular viability, in this study we evaluated whether BLI can be used in conjunction with cellular MRI to follow cancer cell fate from their initial arrest in the brain to the formation of overt tumors in a well-established mouse model of breast cancer metastasis. We demonstrate that BLI complements well with our sensitive cellular MRI technologies, allowing us for the first time to get direct longitudinal measures of whole-brain single cell arrest, tumour volumes, and cancer cell viability, providing a more holistic view of transplanted cancer cell fate in living subjects. Importantly, combining of these imaging technologies should be broadly applicable to numerous preclinical models of experimental metastasis.

2.2   Materials & Methods

2.2.1   Cell Labelling and Transduction Procedure

Brain seeking human breast carcinoma cells (JIMT1-BR3) were engineered to stably co-express FLuc and GFP following transduction with an LVP020 lentiviral vector (GenTarget Inc., CA, USA). These cells were transduced and generously gifted by Dr.

Patricia Steeg's lab. Cells were maintained in DMEM containing 10% FBS at 37°C and 5% CO^2. For iron labeling, 2×10^6 cells were plated in a 75cm^3 flask, supplemented with DMEM containing 10% FBS, and allowed to adhere for 24 hours. Then cells were incubated for an additional 24 hours with 10mL media containing 25μg/mL of MPIO beads (0.9 um in diameter, 63% magnetite, labeled with Flash Red; Bangs Laboratory, Fishers, IN, USA). Cells were washed once in the flask with Hanks balanced salt solution (HBSS) and then trypsinized with 0.25% Trypsin-EDTA. The cells were then collected and thoroughly washed three more times with HBSS to remove unincorporated MPIO before cell injection and *in vitro* evaluation.

2.2.2   In Vitro Studies

To evaluate the relationship between cell number and BLI signal, cells were seeded in 24-well plates in 0.5 mL of growth medium at concentrations of 5×10^3, 1×10^4, 2×10^4 and 5×10^4 cells per well. Cells were allowed to adhere for 24 hours and then 5μL of D-luciferin (30mg/mL; Perkin Elmer) was added to the growth medium 5 minutes prior to BLI using a hybrid optical/Xray scanner (In Vivo FX PRO; Bruker formerly Kodak).

To evaluate if MPIO labeling effects BLI signal, cells were seeded in 24-well plates in 2mL of growth medium with 1×10^4 cells per well. Cells were allowed to adhere for 24hr and then 25μg/mL of MPIO was added to the growth medium for half of the wells. Cells were then incubated for an additional 24hr before 5μL of D-luciferin (30mg/mL) was added for BLI.

2.2.3   Animal Model

The animals were cared for in accordance with the standards of the Canadian Council on Animal Care, and under an approved protocol of the University of Western Ontario's Council on Animal Care. To deliver MPIO-labeled FLuc/GFP+ cells into the brain, 1.75×10^5 cells were injected into the left ventricle of 12 female nu/nu mice (6 –7 weeks old; Charles River Laboratories, Wilmington, MA, USA). Cells were suspended in 0.1mL of HBSS and image-guided slow injections into the left ventricle were performed using a Vevo 2100 ultrasound system (VisualSonics Inc.).

2.2.4   Animal Work Design

Figure 2.1 illustrates the 4-week timeline of our *in vivo* multimodality imaging model. Twelve mice received intracardiac injections of 1.75×10^5 MPIO-labeled JIMT1-BR3-FLuc/GFP+ cells on day 0. BLI signal was detectable one-hour post injection and was used to differentiate between mice that had a successful intracardiac injection and mice that did not. Mice that did not have successful injections were excluded from the remainder of the study. Mice that had successful injections moved onto day 0 MRI four hours post injection. These mice were then imaged with both BLI and MRI on days 8, 21 and 28. After endpoint imaging, one mouse was sacrificed for cryofluorescence imaging and the rest were sacrificed for histology.
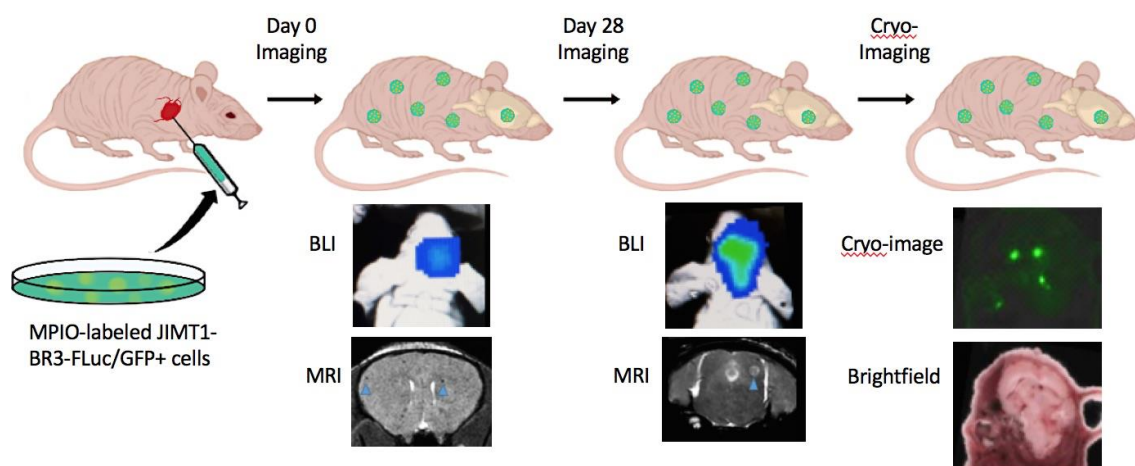
Figure 2.1 Experimental design for in vivo imaging: Illustration of MRI, BLI and fluorescence cryo-imaging of metastases in mice with intracardiac injection of human breast carcinoma cells. Original image courtesy of Chelsey Gareau.

2.2.5   BLI Procedure

All *in vivo* BLI was performed on a hybrid optical/Xray scanner (In Vivo FX PRO; Bruker formerly Kodak). Mice were anesthetized with isofluorane (2% in 100% oxygen) using a nose cone attached to an activated carbon charcoal filter for passive scavenging. Approximately one hour following cell injection whole body BLI imaging was used to screen mice for successful intracardiac injection on day 0. Only mice with BLI signal from the brain proceeded to MRI (i.e., only mice with successful intracardiac injections). On days 0, 8, 21 and 28, mice received 150 μL of D-luciferin (30mg/mL) intraperitoneally and BLI images were captured every 5 minutes for up to 35 minutes.

2.2.6   MRI Procedure

All MRI scans were performed on a 3T GE clinical MR scanner (General Electric) using a custom-built gradient coil and a custom-built solenoidal mouse brain radiofrequency coil [3,14]. Mice were anesthetized with isofluorane (2% in 100% oxygen) using a nose cone attached to an activated carbon charcoal filter for passive scavenging and images were obtained using a 3D balanced steady state free precession (bSSFP) imaging sequence [Fast Imaging Employing Steady State Acquisition (FIESTA) on the GE system] which has been previously optimized for iron detection [15]. Mice were imaged on days 0, 8, 21 and 28. The scan parameters for days 0 and 8 were: repetition time (TR) = 8ms, echo time (TE) =4ms, bandwidth (BW) = 41.7kHz, flip angle (FA) = 35 degrees, averages (NEX)= 2, phase cycles=4, matrix = 150x150. Total scan time was approximately 15 minutes per mouse. For days 21 and 28, a longer scan time was required for tumour detection and so imaging

parameters were: TR=10ms, TE=5ms, BW= 12.5kHz, FA=35 degrees, NEX=2, phase cycles=8, matrix= 150x150. Total scan time was approximately 35 minutes per mouse.

2.2.7 Image Analysis

Brain BLI signal was measured using region-of-interest (ROI) analysis using the Bruker Molecular Imaging Software. An ROI was drawn around the brain, the mean photon flux (photons/second/mm^2) was measured, and the peak value over the 30-minute imaging session was used for each mouse at each time point. MRI images were analyzed using OsiriX software (Pixmeo, SARL, Bernex, Switzerland). The number of dark pixels within the total brain volume was also determined from day 0 images; The brain was outlined as a region of interest where a threshold value is set based on the mean value of signal void ±2 standard deviations. The total number of black pixels under this threshold value was obtained from the entire tumour volume signal intensity histogram. For days 0 and 8 images, signal voids were also manually counted in every 8th slice. The sum of all slices was then multiplied by 4 to account for a standard signal void that goes through an average of two slices. For days 21 and 28, brain metastases were manually traced by a single observer. 3D tumor volumes were reconstructed using the OsiriX volume algorithm from the manual segmentation of a region of interest around each tumor boundary in every bSSFP image slice for each mouse.

2.2.8 Histology

At endpoint, mice were sacrificed by pentobarbital overdose and perfusion fixed with 4% paraformaldehyde. Mouse brains were removed and cryopreserved in ascending

concentrations of sucrose (10, 20, and 30% w/v) in distilled water for 1 hour each. Brains were immersed in optimal cutting temperature (OCT) compound, oriented in a sectioning plane parallel to that of MRI, and frozen using liquid nitrogen. Contiguous 10-μm frozen sections were collected and stained using the following: hematoxylin and eosin (H&E) to visualize tumour morphology, *Firefly* luciferase antibody (Abcam Inc., Cambridge, MA,USA; product # ab21176, dilution factor 1:1000) to identify luciferase positive cells, and Perl's Prussian blue (PPB) staining to visualize iron. Stained sections were imaged using a Zeiss 510 laser scanning confocal microscope and GFP-positive cancer cells were also imaged.

2.2.9　Cryo-Fluorescence Imaging

After endpoint MR imaging (day 28), one mouse was sacrificed by pentobarbital overdose and then flash frozen in OCT freezing medium by liquid nitrogen immersion. The entire mouse was sectioned and optically imaged every 50μm using a CryoViz^{TM} (Bioinvision Inc., Cleveland, OH) cryo-imaging device. Block-face images were collected with an in plane resolution of 10.5 x 10.5 μm^2. Brightfield and fluorescent images were acquired, stitched together and visualized using proprietary software (Bioinvision Inc).

2.2.10　Statistics

We evaluated the effect of MPIO labeling on BLI signal in the JIMT1-BR3/FLuc-GFP cell line using a two-tailed t-test. Pearson correlational analysis of cell number to photon flux in culture was performed as well as on *in vivo* BLI and MRI data on days 0 and 28. For all tests, a nominal p-value <0.05 was considered statistically significant.

2.3 Results

2.3.1 In Vitro Studies

Figure 2.2A shows the JIMT1-BR3/FLuc-GFP cell line was efficiently labelled with MPIO. The Perl's Prussian blue stain shows intracellular iron in blue within the breast cancer cells that appear pink. JIMT1-BR3/FLuc-GFP cells were seeded at $5\text{x}10^3$, $1\text{x}10^4$, $2\text{x}10^4$, and $5\text{x}10^4$ cells per well and BLI was performed. A significant positive correlation was seen between the number of JIMT1-BR3/FLuc-GFP cells seeded per well and BLI signal ($R^2 = 0.928$). More specifically, as cell number increased, BLI signal also increased (Figure 2.2B, 2.2C). There was no significant difference in BLI signal detected in cells that were labeled with MPIO ($M = 2.00 \text{ x } 10^7 \pm 5.17 \text{ x } 10^6$ p/s/mm^2) and cells that were not labeled ($M = 2.18 \text{ x } 10^7 \pm 5.21 \text{ x } 10^6$ p/s/mm^2) (*ns, p value* $=0.82$; Figure 2.2D, 2.2E). This suggests that MPIO labelling has no significant quenching effect on BLI signal. These results are from three independent experiments with three replicates of each condition.
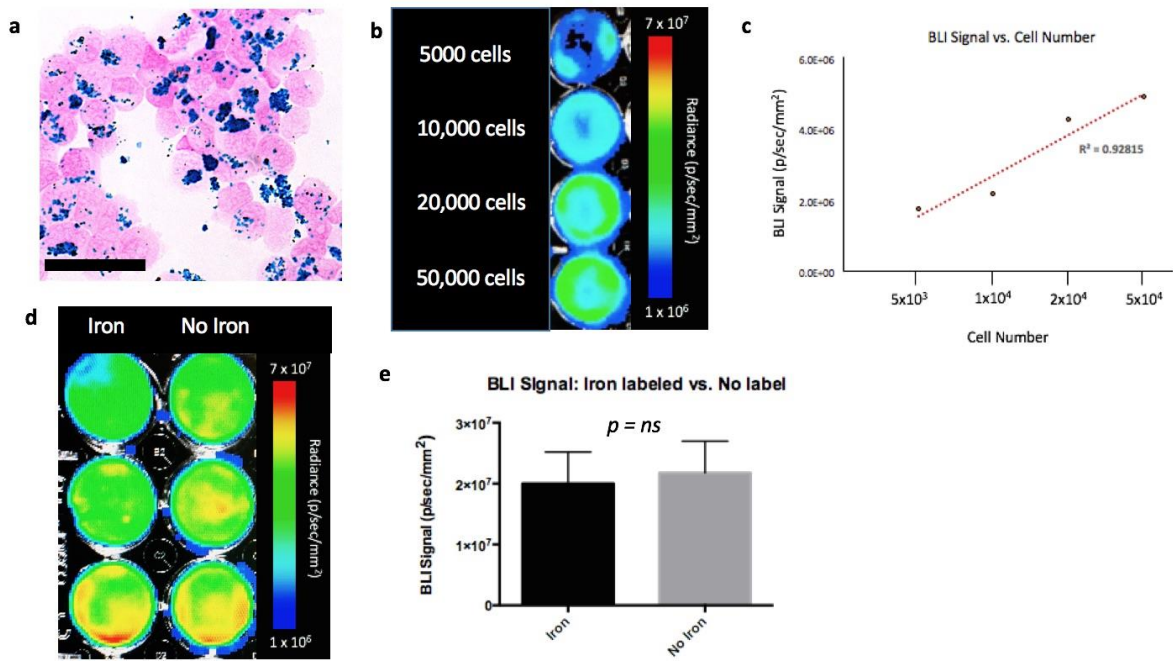
Figure 2.2 In vitro experiments: a) Perl's Prussian blue stain identifies iron labelled cells in blue (scale bar x 100). b) JIMT1BR3-Fluc/GFP+ cells seeded at various concentrations c) A strong linear correlation is seen between cell number and BLI signal; R^2 =0.928 d) MPIO labeled JIMT1BR3-Fluc/GFP+ cells (L) and non-labeled JIMT1BR3-Fluc/GFP+ cells (R). e) There was no significant difference in BLI signal detected in cells that were labeled with MPIO and cells that were not labeled (ns, p value =0.82). These results are representative of three experiments with three wells of each condition.

2.3.2   In Vivo Studies

Figure 2.3 shows image data from day 0. On day 0, iron labeled cells were visualized as signal voids by MRI, distributed throughout the brain (Figure 2.3A). On average, 609± 98 discrete, signal voids per brain were quantified throughout the brains in MRI images from the nine animals that had successful injections of 1.75×10^5 MPIO-labeled cells. As mentioned, BLI signal was also detected in the brain of these nine mice on day 0 (Figure 2.3B). Three of twelve mice did not have a successful intracardiac injection and showed signal in other organs such as the lungs or abdominal cavity but not in the brain. These mice were excluded from the remainder of the study. Figure 2.3C shows that the number of signal voids measured on day 0 by MRI showed a significant correlation with BLI signal in the brain on day 0 (R^2=0.75, $p < 0.01$). Percent black pixels were also measured from day 0 MRI images with the average percent black pixels within the whole brain being 3.35%; and showed a significant correlation with day 0 BLI signal in the brain (R^2=0.74, $p < 0.01$) (Figure 2.3D).
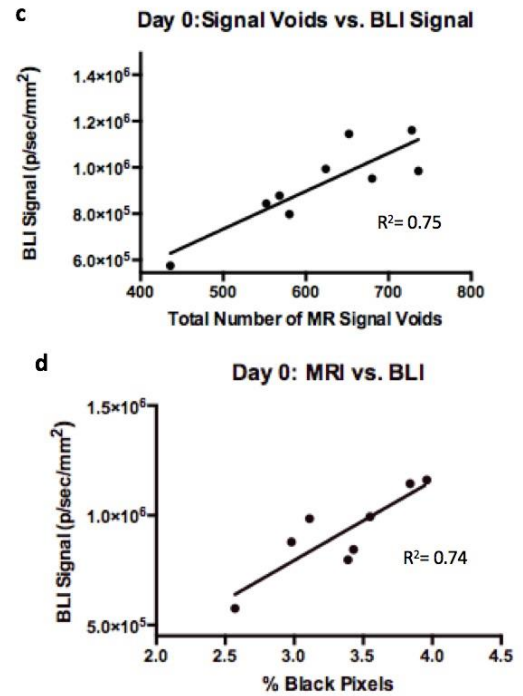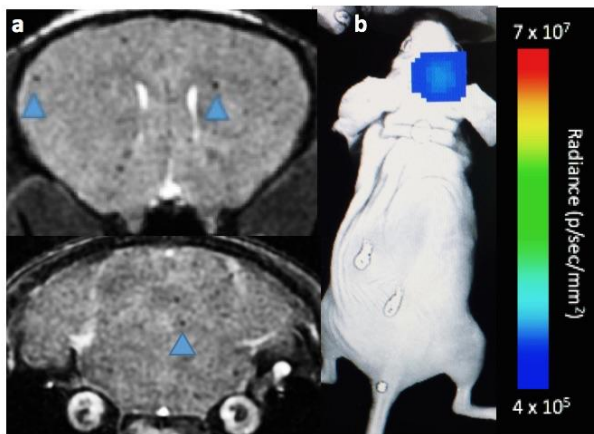
Figure 2.3 Day 0 Imaging: a) single arrested cells could be visualized as signal voids (blue arrows) in day 0 MR images. b) BLI signal was detectable in the brain on day 0. c) A significant correlation was found between total number of signal voids measured from day 0 MRI scans and day 0 BLI signal in the brain (R^2=0.75, p < 0.01). d) A significant correlation was found between total percentage of black pixels measured from day 0 MRI scans and day 0 BLI signal in the brain (R^2=0.74, p < 0.01).

Figure 2.4A shows imaging data over time and illustrates the MRI and BLI signal loss and recurrence over time with tumour development. Notably, on day 8, there were few to no voids seen by MRI and no detectable BLI signal in the brain; this is because the majority of cancer cells die and are cleared and those that remain are below our current BLI detection threshold. On day 21, three of nine mice showed BLI signal in the brain as well as small tumours detected by MRI. The remaining six mice did not have detectable tumours with either MRI or BLI at day 21. On day 28, these three mice had increased BLI signal and larger brain metastases detected by MRI.

When we graph BLI signal over time, we found that the signal dropped at day 8 when the cells were cleared but returned again when tumours started to form by day 21 (Figure 2.4B). A one-way ANOVA was performed and BLI signal in the brain was found to be significantly different at all time points ($p < 0.0001$).
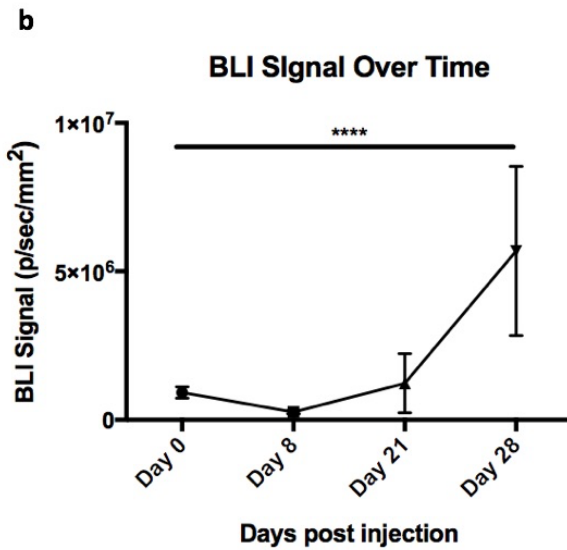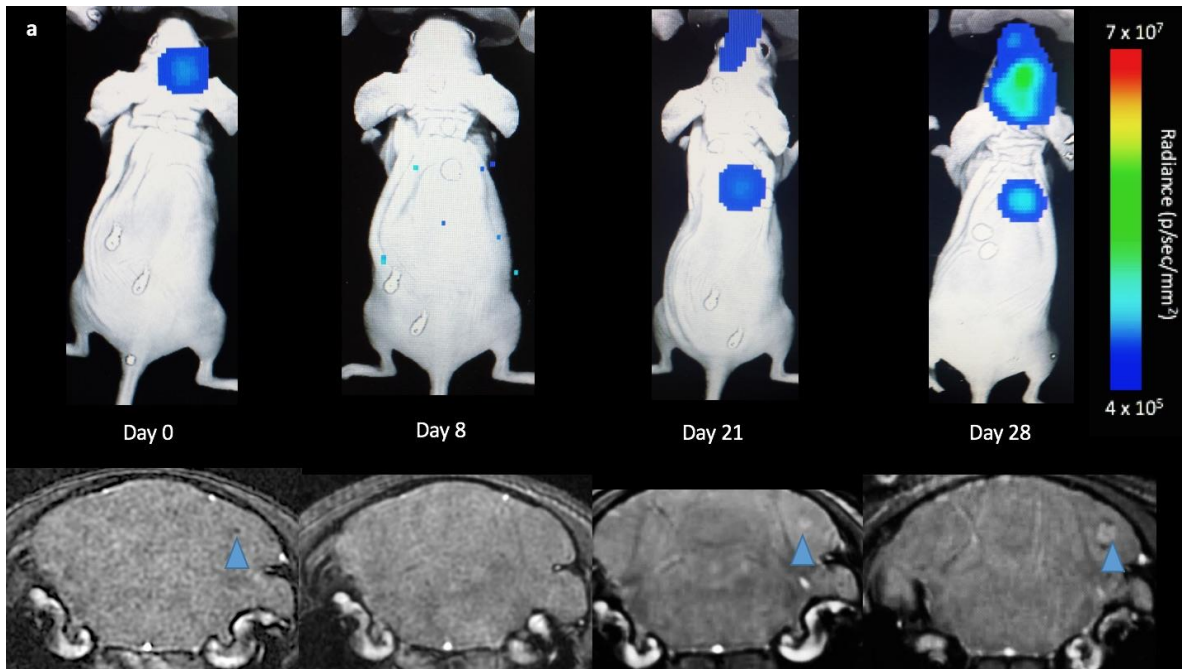
Figure 2.4 MRI and BLI over time a) Representative BLI (top) and MRI images (bottom) of one mouse imaged on days 0, 8, 21 and 28; blue arrow shows signal void progressing into tumour b) BLI signal in the brain over time. This graph is

representative of 8 mice that made it to endpoint. A one-way ANOVA was performed

and all time points were found to be significantly different (p < 0.0001).

Figure 2.5 shows image data from day 28. One mouse had to be sacrificed after day 21 imaging and so day 28 data is representative of eight mice. By day 28, brain metastases appeared as regions of hyperintensity by MRI and BLI signal was detected in the brains of all eight mice that had made it to endpoint (Figures 2.5A, 2.5B). In BLI images, six out of eight mice also showed metastases in areas other than the brain. Total brain tumour burden measured by MRI at endpoint (day 28) showed a significant correlation with BLI signal in the brain on day 28 (R^2=0.80, $p < 0.01$) (Figure 2.5C).
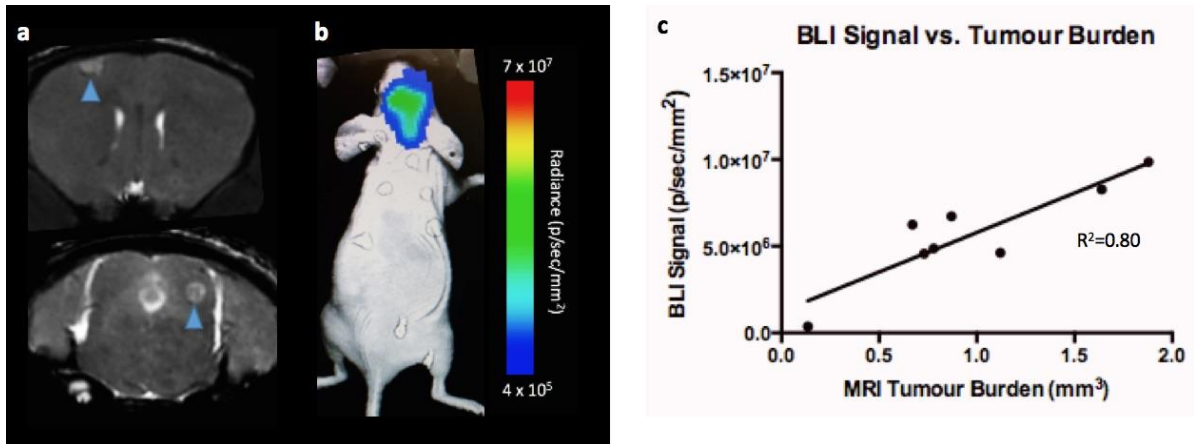
Figure 2.5 Day 28 Imaging: a) Brain metastases (blue arrows) appear as region of hyperintensity in day 28 MR images. b) Tumours were also detected using BLI on day 28. c) A significant correlation was found between total brain tumour burden measured by MRI at endpoint (day 28) and BLI signal in the brain (R^2=0.80, $p < 0.01$).

2.3.3 Histology and Whole-mouse Cryo-fluorescence Imaging

Mice were sacrificed 28 days after intracardiac cell injection. Dual fluorescence microscopy of immunostained sections demonstrated that the location of luciferase positive cells (labelled with red fluorescence) corresponded with the location of GFP expression (seen in green) (Figure 2.6). These dual labelled cells also corresponded well with tumours seen in MR images suggesting that metastases are composed of the FLuc-GFP positive cells. In one mouse, the presence of tumours was also confirmed using cryo-fluorescence which has the ability to perform whole-body brightfield and fluorescence imaging throughout the entire mouse. Cryo-imaging allowed for the detection of metastases at day 28 in both the brain and other areas of the body (Figure 2.7). Some of the metastases seen with cryo-imaging could be matched to MR tumours but not all of them; this is likely because some were too small to be detected with MRI. Whole body cryo-imaging also allowed for the localization of metastases seen with BLI. Due to light scattering and depth limitations, we cannot be certain where within the body the BLI signal is coming from; cryo-imaging allows us to further explore a region of signal and find out where exactly the tumour is located within the mouse body.
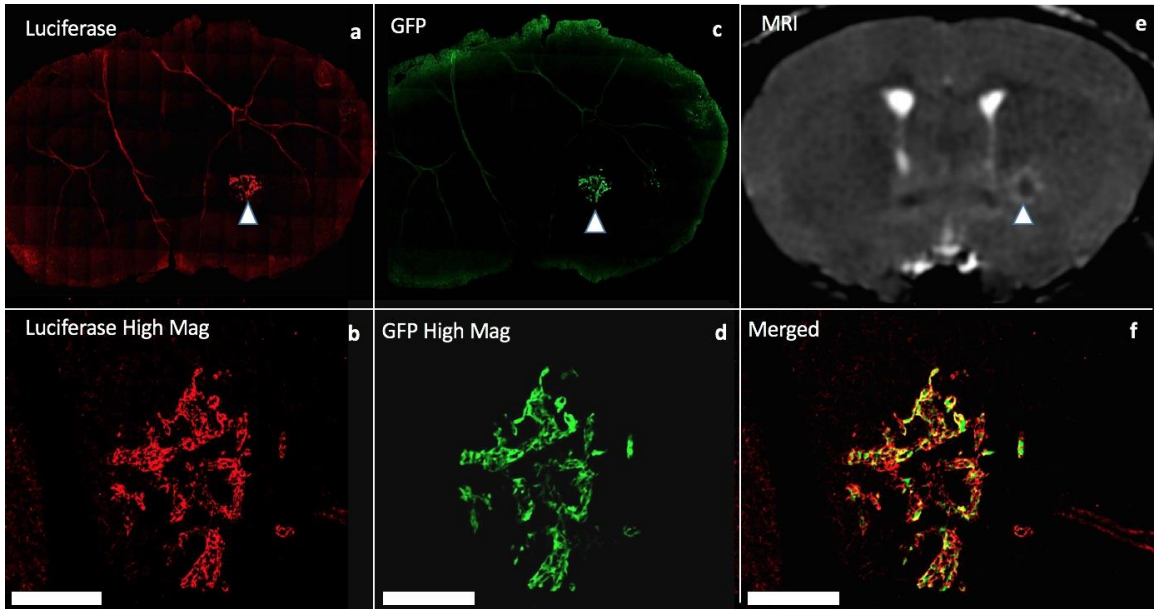
Figure 2.6 Fluorescence microscopy and immunohistochemistry: *Firefly* **luciferase stain (c,d) green fluorescence protein (a/c low magnification, b/d high magnification) e) Corresponding MRI image f) Merged luciferase and GFP images at high magnification; blue arrows show tumour within whole slice image. Scale bars = 300um**
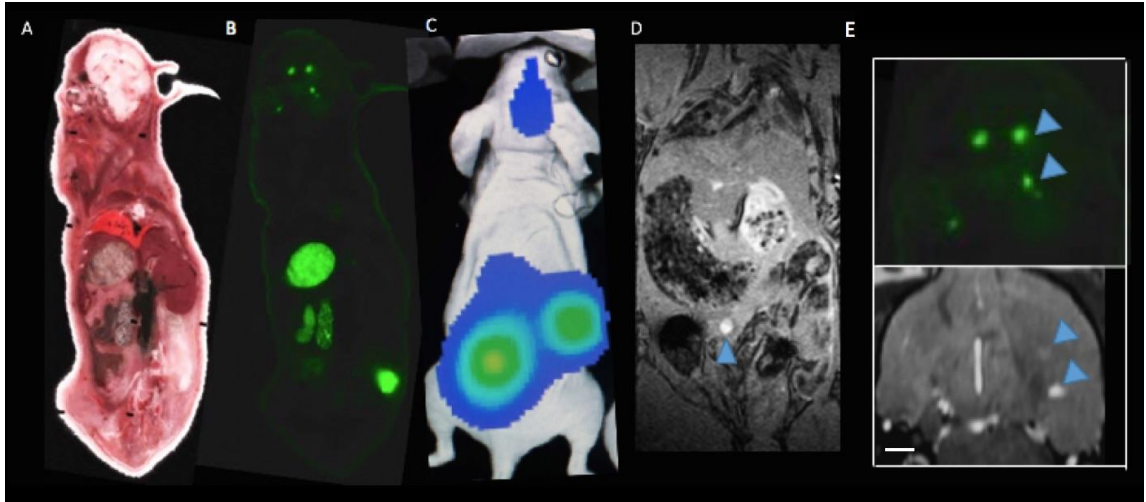
Figure 2.7 Cryoviz Imaging: (A) Brightfield image of cryoviz mouse imaged on day 28 (B) Fluorescence microscopy detects GFP+ brain tumours and body tumours in same slice as brightfield image (C) Corresponding day 28 BLI and (D) Whole body MRI (E) Brain metastases (blue arrows) in cryo-image and corresponding MRI slice in the same orientation. Scale bar = 0.50mm

2.4 Discussion

We have previously demonstrated that cellular MRI is a valuable cell tracking tool for preclinical investigation of brain metastatic breast cancer. However, it has limited ability to differentiate between dead and viable cells. Moreover, MRI can also provide measures of tumor volume in mouse models but this can potentially overestimate the number of viable cancer cells in those tumors. In this study, we have for the first time combined cellular MRI with BLI to provide longitudinal measures of cellular viability and better study the entire metastatic cascade, from initial arrest to tumor formation, in a well-established breast cancer brain metastases mouse model. BLI complemented our cellular MRI techniques well, demonstrating for the first time that MR measures of early cell arrest are indeed viable cancer cells, that the decrease in MR void number from day 0 to day 8 is due to loss of arrested viable cells rather than loss of iron label, and that MR measures of brain tumor volumes at day 28 correlate well with BLI measures of cellular viability, indicating that tumors are mostly composed of viable cells in this model.

Past studies have found that the left cardiac ventricular delivery of cells is an ideal model for monitoring *in vivo* single cell detection; this is due to the fact that the delivery to a given organ is initially proportional to the percentage of cardiac output (%CO) to that organ. In this case, the %CO to the brain is ~9.5% and therefore for an injection of 175,000 cells, we can expect ~16,625 cells to be delivered to the brain microcirculation[16]. However, <1% of these cells are expected to be retained in the brain by 2 hours post injection[16]. On average, 609± 98 discrete, signal voids were visualized throughout the brain in day 0 MRI images. The MPIO used to label the JIMT1BR3-FLuc/GFP cells affects the MR signal by creating

a blooming effect. As a result, a signal void appears much larger than the cell itself; making single cell detection feasible. It has been shown that a signal void is usually representative of a single cell, however it can also be representative of two or three cells clumped together[3]. Thus, the 400-700 cells we are detecting at day 0 may be closer to 1000 cells.

When compared to other imaging technologies, BLI is often characterized as relatively inexpensive, user friendly and highly sensitive. As a result, BLI can be used as a high-throughput screening tool for cell tracking studies. In this study, we used BLI to screen for successful intracardiac injections on day 0. Mice that did not have a successful injection, did not have any bioluminescent signal detected in the brain and thus were excluded from the study. Prior to developing this model, each mouse would need to undergo a day 0 MRI scan to determine if the injection was successful by detecting arrested cells (i.e., signal voids). BLI can also be used to guide experimental design as well as predict or evaluate a region of interest in less developed animal models. In this study, whole body BLI allowed for the detection of metastases at sites that we had not previously detected or evaluated. Day 28 BLI images helped to predict suspected organs of metastasis for *ex vivo* analysis. To achieve sufficient resolution to detect iron-labelled cells in the brain, within a suitable scan time, only the brain is imaged with MRI and metastases in other parts of the body may have been overlooked if they were not prominent.

While MRI and BLI have been used separately as measures of overall tumour burden, primarily in models with singular tumours, the concurrent application of BLI and MRI to studying the entire process of brain metastasis has not been performed. In this work, BLI

allowed for repetitive, non-invasive, whole body imaging and MRI based measurements were used to validate BLI measurements of single cell arrest and tumour burden in the mouse brain. There was a significant linear relationship between tumour volume measured by MRI and light output measured by BLI. Although our MRI based measurements may be a result of both dead and live tumour cells, phagocytic bystander cells (for iron measurements), and other tumour stromal cells, BLI signal is representative of viable tumour cells only. The correspondence between modalities at day 28 suggests that our metastases are made up of mostly viable cancer cells at this time point. If we had imaged at a later time point the correlation between modalities may become weaker as tumours progress and develop a necrotic core. Similarly, if treatment was given, a decrease in viable tumour tissue will affect the correlation between our multimodality tumour burden measurements. This is an important advantage of BLI when evaluating potential treatment paradigms, as a tumour may not look anatomically different in early stages of treatment but the amount of viable tissue within that tumour may change.

Cryo-imaging allowed for the detection of fluorescent micrometastases in the brain as well as other places in the body. While food in the abdominal cavity creates some autofluorescence this may be alleviated in the future using alfalfa-free diets. However, tumours detected with cryo-fluorescence imaging that appear to be in the middle right abdominal cavity and above the left hindlimb matched well with BLI images and appear much brighter than the autofluorescence from the food. Like MRI, the cryo-imaging can also allow us to localize and count the number of micrometastases in the brain where as the BLI image gives us one individual measure for all combined tumours. Some brain

metastases found in MR images matched our cryo-fluorescence images well while others appeared too small to be detectable with MRI.

This study demonstrates how a multimodality imaging model that uses both MRI and BLI can overcome the limitations of using each modality independently. Although BLI can produce a measure of tumour burden within the brain, we are unable to collect information on the number, size or distribution of tumours within the region of interest. This can be a limiting factor in cancer metastasis models that use BLI only; numerous tumours or arrested cells that are close in proximity appear as one large region of signal due to light scattering, and at equivalent sizes tumours that are more superficial will appear to be brighter than those that are located deeper. In contrast, MRI can detect individual iron-loaded cells and provide information on tumour 3D location and size. These modalities also complement each other at different time points throughout the experiment. Our current BLI protocol was not sensitive enough to detect signal in the brain on day 8, even though we know there are in fact viable cancer cells there (i.e., tumours formed in the brain and signal voids were seen on day 8). Future work using newer luciferase substrates or BLI machines with more sensitive CCD cameras could overcome this limitation[17, 18]. However, our cellular MRI technology was able to detect the limited number of cells that persisted in the brain on day 8. By day 21 tumours were easily detected by BLI in three of nine mice however, these tumours were very small and thus difficult to find with MRI. Tumours with minimal burden and MR contrast on day 21 may have been overlooked if BLI signal had not predicted metastases prior to MRI imaging.

2.5   Conclusion

In this work, we applied multimodality imaging to monitor the growth of metastatic breast cancer cells in the brain from single arrested cells to overt tumours. BLI complemented our sensitive iron-based cellular MRI technologies well, allowing us for the first time to get direct longitudinal measures of whole-brain single cell arrest, tumour burden, and cancer cell viability in the brain. Future work will extend these tools for whole-mouse MRI/BLI of metastatic burden, which will be extremely valuable for enabling an improved understanding of the fate of single cancer cells throughout the body and evaluation of current and emerging treatment paradigms.

2.6   References

1. Siegel, R., Ma, J., Zou, Z. & Jemal, A. Cancer statistics, 2014. *CA: Cancer J Clin.* **64**, 9-29 (2014).

2. Fass, L. Imaging and cancer: A review. *Mol Oncol.* **2**, 115-152 (2008).

3. Heyn, C., Bowen, C., Rutt, B. & Foster, P. Detection threshold of single SPIO-labeled cells with FIESTA. *Magnet Reson Med.* **53**, 312-320 (2005).

4. Shapiro, E. M. *et al.* MRI detection of single particles for cellular imaging, *Proc Natl Acad Sci USA.* **101**, 10901-10906 (2004).

5. Wu, Y. L. *et al*. In situ labeling of immune cells with iron oxide particles: an approach to detect organ rejection by cellular MRI, *Proc Natl Acad Sci USA*. **103**, 1852-1857 (2006).

6. Gonzales-Lara LE. *et al*. The use of cellular magnetic resonance imaging to track the fate of iron-labelled multipotent stromal cells after direct transplantation in a mouse model of spinal cord injury. *Mol Imaging Biol*. **13,** 702–711 (2011).

7. Noad J, *et al*. MRI tracking of transplanted iron-labeled mesenchymal stromal cells in an immune-compromised mouse model of critical limb ischemia. *NMR Biomed.* **26**, 458–467 (2013).

8. Lu S, *et al*. In vivo MR imaging of intraarterially delivered magnetically labeled mesenchymal stem cells in a canine stroke model. *PLoS ONE*. **8**, e54963 (2013).

9. Amsalem, Y. et al. Iron-oxide labeling and outcome of transplanted mesenchymal stem cells in the infarcted myocardium. *Circulation.* **116**, I-38 (2007).

10. Winter, E.M. *et al*. Cell tracking using iron oxide fails to distinguish dead from living transplanted cells in the infarcted heart. *Magn Reson Med.* **63**, 817–821 (2010).

11. Prescher, J. & Contag, C. Guided by the light: visualizing biomolecular processes in living animals with bioluminescence. *Curr Opin Chem Biol.* **14**, 80-89 (2010).

12. Jost, S. C. *et al*. Measuring brain tumor growth: combined bioluminescence imaging–magnetic resonance imaging strategy. *Mol Imaging.* **8**, 7290-2009 (2009).

13. Koberle M. *et al*. Monitoring Disease Progression and Therapeutic Response in a Disseminated Tumor Model for Non-Hodgkin Lymphoma by Bioluminescence Imaging. *Mol Imaging.* **14**, 400-413 (2015).

14. Heyn, C. et al. In vivo MRI of cancer cell fate at the single-cell level in a mouse model of breast cancer metastasis to the brain. *Magn Reson Med.* **56,** 1001-1010 (2006).

15. Ribot, E. *et al*. In vivo single scan detection of both iron-labeled cells and breast cancer metastases in the mouse brain using balanced steady-state free precession imaging at 1.5 T. *J. Magn Reson Imaging.* **34,** 231-238 (2011).

16. Basse, P., Hokland, P., Heron, I. & Hokland, M. Fate of Tumor Cells Injected Into Left Ventricle of Heart in BALB/c Mice: Role of Natural Killer Cells. *J Natl Cancer I.* **80,** 657-665 (1988).

17. Evans, M. et al. A synthetic luciferin improves bioluminescence imaging in live mice. *Nature Methods.* **11,** 393-395 (2014).

18. Adams, S. & Miller, S. Beyond D-luciferin: expanding the scope of bioluminescence imaging in vivo. *Curr Opin Chem Biol.* **21,** 112-120 (2014).

Chapter 3

3 Multimodality cellular and molecular imaging of concomitant tumour enhancement in a syngeneic mouse model of breast cancer metastasis

Introduction: The mechanisms that influence metastatic growth rates are poorly understood. One mechanism of interest known as concomitant tumour resistance (CTR) can be defined as the inhibition of metastasis by existing tumour mass. Conversely, the presence of a primary tumour has also been shown to increase metastatic outgrowth, termed concomitant tumour enhancement (CTE). The majority of studies evaluating CTR/CTE in preclinical models have relied on endpoint histological evaluation of tumour burden. **Objective**: The goal of this research was to use conventional magnetic resonance imaging (MRI), cellular MRI, and bioluminescence imaging to study the impact of a primary tumour on the development of brain metastases in a syngeneic mouse model. **Results:** Here, we report that the presence of a 4T1 primary tumour significantly enhances total brain tumour burden in Balb/C mice. Using in vivo BLI/MRI we could determine this was not related to differences in initial arrest or clearance of viable cells in the brain, which suggests that the presence of a primary tumour can increase the proliferative growth of brain metastases in this model. **Conclusion**: The continued application of our longitudinal cellular and molecular imaging tools will yield a better understanding of the mechanism(s) by which this physiological inhibition (CTR) and/or enhancement (CTE) occurs.

3.1 Introduction

Breast cancer is the second leading cause of cancer related deaths in North America with the majority of deaths due to metastasis, the dissemination of cancer cells from the primary tumour to other parts of the body[1]. One of the most common, as well as most fatal sites of metastatic growth for breast cancer patients is the brain, with the incidence of brain metastasis increasing and prognosis remaining poor[2]. Improved knowledge regarding how quickly cancer cells disseminate from the primary tumour and the rate of secondary metastases development, as well as the mechanisms that control proliferation rate, are key to developing new therapies to prevent or halt metastatic growth and prevent cancer mortality.

The mechanisms that influence metastatic growth rates are poorly understood. One mechanism of interest is concomitant tumour resistance (CTR), which describes the ability of the primary tumour to restrict the growth of distant metastases[3,4]. The relevance of CTR has been shown by numerous observations of the removal of a primary tumour being followed by an abrupt acceleration of residual metastatic disease. CTR has been observed in both breast cancer patients[5] and animal models of breast cancer[6]. It has also been observed in patients with other solid tumour types[7,8]. Conversely, it has been shown that the presence of a primary tumour can likewise increase metastatic outgrowth, a phenomenon coined concomitant tumor enhancement (CTE). However, in the clinic, very few examples of CTE have been reported with most of them being related to suspected regressions of hepatic and/ or pulmonary metastases following nephrectomy for renal cell carcinoma[9-12]. While imaging has been used to describe CTR/CTE effects in patients[13], the

majority of studies evaluating CTR/CTE in preclinical models have relied on endpoint histological evaluation of tumour burden[14,15]. The application of cellular and molecular imaging tools will allow the non-invasive and longitudinal visualization of metastatic progression to study CTR/CTE effects *in vivo*, which will ultimately yield better evaluation of putative molecular mechanism(s) by which this physiological inhibition and/or enhancement occurs. In turn, this may lead to new anti-metastatic therapeutics aimed at these mechanisms and their non-invasive evaluation.

Previously, we applied cellular MRI techniques to study the impact of a primary tumour on metastatic outgrowth in an immune deficient mouse model of experimental breast cancer metastasis to the brain and demonstrated clear CTR effects in the brain[16]. Cellular MRI involves pre-labeling cultured cancer cells with superparamagnetic iron oxide nanoparticles prior to transplantation into mice. This labeling allows transplanted cells to be tracked over time with iron-sensitive MRI techniques. Single cell imaging of cancer cells arresting in the brain at the time of injection and of non-dividing, iron-retaining cancer cells over time is achievable with this technique[17]. However, limitations of iron oxide based cellular MRI are that there is limited ability to differentiate between dead and viable cells, that it is possible for iron particles to be transferred to bystander cells such as macrophages upon cell death, and that the iron particles are diluted during cell division leading to loss of cell detection in proliferative cells. These limitations can be overcome using reporter gene based cell tracking tools, since a stably expressed reporter gene is passed on to daughter cells and will not be expressed in bystander cells. By engineering cells to express a luciferase reporter, bioluminescence imaging (BLI) can provide a direct readout of cell

viability in dividing cell populations. Overall, as recently described[18], combining our highly sensitive cellular MRI tools and BLI yields complementary information on the fate of metastatic cancer cells in preclinical models. As others have pointed to a role of the immune system in CTR/CTE and differences in primary tumour effects have been seen across models of the same cancer type[8], the purpose of this study was to apply our multimodality imaging tools to study whether CTR/CTE effects are present in the syngeneic 4T1 immune competent mouse model of breast cancer metastasis.

3.2   Methods

3.2.1   Cell Labelling and Transduction Procedure

The 4T1-BR5 cells were received from Dr. Patricia Steeg's lab and engineered to stably co-express red-shifted *Luciola Italica* luciferase (Red-FLuc) and green fluorescent protein (GFP) using a commercial lentiviral vector (RediFect Red-FLuc-GFP; PerkinElmer, USA). Cells were transduced and FACS sorted based on GFP expression using a FACSAria III flow cytometric cell sorter (BD Biosciences). The resultant 4T1BR5-Red-FLuc/GFP cells were maintained in DMEM containing 10% FBS and 1% antibiotics, at 37°C and 5% CO_2. For iron labeling, $2x10^6$ 4T1BR5-Red-FLuc/GFP cells were plated, and 24 hours later were incubated with 25µg/mL of micron-sized superparamagnetic iron oxide (MPIO) beads for an additional 24 hours (0.9 µm in diameter, 63% magnetite, conjugated with Flash Red; Bangs Laboratory, Fishers, IN, USA). Cells were washed three times with Hanks balanced salt solution (HBSS), collected and thoroughly washed three more times with HBSS to wash off residual unincorporated MPIO before *in vitro* evaluation or injection into animals.

94

3.2.2 In Vitro Studies

All *in vitro* results are from three independent experiments with three replicates of each condition. To evaluate the relationship between cell number and BLI signal, 1×10^3, 5×10^3, 1×10^4, 1.5×10^5, and 5×10^5 4T1BR5-Red-FLuc/GFP cells were seeded in each well of 24-well plates. Twenty-four hours later, 5 µL of D-luciferin (30 mg/mL; Syd Labs, Inc., MA, USA) was added to the growth medium and BLI images were collected 5 minutes later using a hybrid optical/X-ray scanner (IVIS Lumina XRMS In Vivo Imaging System, PerkinElmer). BLI signal was measured with region-of-interest (ROI) analysis using LivingImage Software (Perkin Elmer). An ROI was drawn around each well to measure the average radiance (photons/second/mm^2/steradian), and the mean average radiance across replicates was determined for each independent experiment.

To evaluate if MPIO labeling influenced BLI signal, 1.25×10^5 4T1BR5-Red-FLuc/GFP cells were seeded in each well of a 24-well plate. Twenty-four hours later, 25µg/mL of MPIO was added for half of the wells. After an additional twenty-four-hour incubation period, the media for all wells was replaced with fresh media without iron, 5µL of D-luciferin (30mg/mL) was added for BLI, and BLI signal per well was analyzed as above.

Vybrant MTT proliferation assays were used to evaluate the effects of genetic engineering on cell proliferation. 6.25×10^3 4T1BR5-Red-FLuc/GFP or naïve 4T1BR5 cells were seeded in each well of 96 well plates and cells were evaluated 24 and 48 hours later. Twenty microliters of MTT solution was added to each well and absorbance at 450nm was measured using a microplate spectrophotometer (Fluoroskan Ascent FL,

ThermoLabSystems). Cell labeling efficiency was assessed by Perl's Prussian blue (PPB) staining, as previously described[19].

3.2.3 Animal Model

Figure 3.1A illustrates the experimental mouse model used in this study. Animals were cared for in accordance with the standards of the Canadian Council on Animal Care, and under an approved protocol of the University of Western Ontario's Council on Animal Care (2014-026). Six to eight-week-old female BALB/c mice (n=32) were obtained from Charles River Laboratories (Willington, MA, USA). Mice received a lower right mammary fat pad (MFP) injection of either vehicle (HBSS; Control mice; n=16) or 300,000 unlabeled 4T1 cells (MFP mice; n=16). MFP tumour growth was evaluated by measurement with calipers in two perpendicular dimensions, and the tumour volume was estimated using the following formula volume = 0.52 (width)^2(length), for approximating the volume (mm^3) of an ellipsoid [20, 21]. MFP tumours grew for either seven days (Small MFP) or 14 days (Large MFP) prior to all mice receiving an intracardiac injection of $2x10^4$ MPIO-labeled 4T1BR5-Red-FLuc/GFP cells in 0.1mL of HBSS. Injections were performed under image guidance using a Vevo 2100 ultrasound system (VisualSonics Inc.).
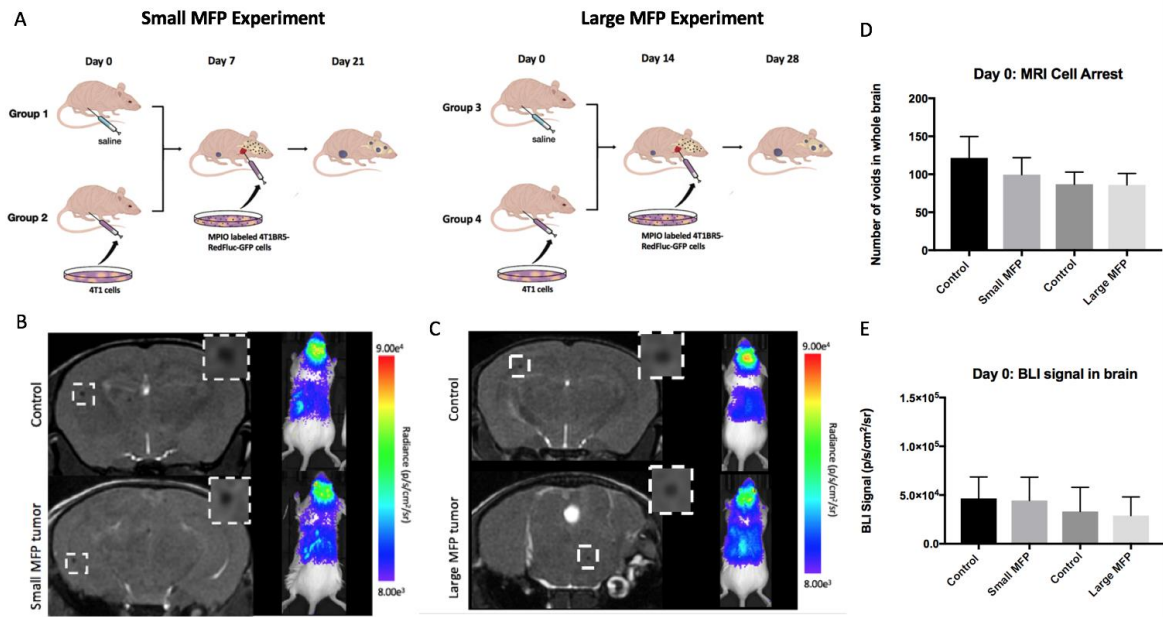
Figure 3.1 Experimental design of animal model: A) Experimental design of animal model used for Small and Large MFP experiments **B)** On day 0, the number of discrete signal voids, representing iron-labeled cells, that arrested in the brain on day 0 as well as brain BLI signal was not significantly different between mice with and without a small MFP tumour. **C)** There were also no significant differences in cell arrest for mice with large MFP tumours. **D/E)** All four groups of mice were not significantly different from each other in MRI cell arrest at day 0 as well as BLI signal in the brain at day 0. Data is presented as mean +/- SD.

3.2.4 BLI Procedure

BLI was performed on days 0, 7 and 14 for all mice after intracardiac injection using a hybrid optical/X-ray scanner (IVIS Lumina XRMS In Vivo Imaging System, PerkinElmer). Mice were anesthetized with isoflurane (2% in 100% oxygen) using a nose cone attached to an activated carbon charcoal filter for passive scavenging. Anesthetized mice received a 150 μL intraperitoneal injection of D-luciferin (30 mg/mL) and BLI images were captured for up to 35 minutes. On day 0, approximately one hour following intracardiac injection, whole body BLI was used to screen mice for successful intracardiac injection on day 0 and to measure brain BLI signal. Only mice with brain BLI signal proceeded to MRI (i.e., only mice with successful intracardiac injections).

3.2.5 MRI Procedure

MRI was performed on a 3T GE clinical MR scanner (General Electric) using custom-built gradient and solenoidal mouse brain radiofrequency coils[22,23]. Mice were anesthetized with isoflurane (2% in 100% oxygen) and images were obtained using a 3D balanced steady state free precession (bSSFP) imaging sequence [Fast Imaging Employing Steady State Acquisition (FIESTA) on the GE system], which has been previously optimized for iron detection[24]. Small MFP and control mice were imaged on days 0, 7, and 14 and large MFP and control mice on days 0 and 14 after intracardiac injection. The scan parameters for day 0 were: repetition time (TR)=8 ms; echo time (TE)=4 ms; bandwidth (BW)=41.7 kHz; flip angle (FA)=35 degrees; averages (NEX)=2; phase cycles=4; matrix=150x150; field-of-view (FOV)= 1.5; resolution: 100 x 100 x 200 μm; and scan time= 19.25 minutes. For days

7 and 14, a longer scan time was required for tumour detection using the following imaging parameters: TR=10 ms; TE=5 ms; BW=12.5 kHz; FA=35 degrees; NEX=2; phase cycles=8; matrix=150x150; FOV=1.5; resolution=100 x 100 x 200 μm; scan time=36.76 minutes. In addition, large MFP mice and corresponding control mice (n=16), a 3D bSSFP imaging sequence was used to obtain high resolution MR images of the whole mouse body on day 9 using a solenoidal whole-body radiofrequency coil. Sequence parameters were as follows: TR=6.3 ms; TE=3.1 ms; BW=31 kHz; FA=35 degrees; NEX=2; phase cycles=8; matrix=300×150; FOV = 60×30 mm; resolution=$200 \times 200 \times 200$ μm^3; and scan time= 22 minutes. One large MFP mouse and one control mouse also had whole body MR scans at endpoint (day 14) to allow us to match MR and BLI detectable metastases to whole-mouse cryo-fluorescence images as described below.

3.2.6   Image Analysis

Brain BLI signal was measured with region-of-interest (ROI) analysis using LivingImage Software (Perkin Elmer). An ROI was drawn around the brain, the average radiance (photons/second/mm^2/sr) was measured, and the peak value over the 35-minute imaging session was used for each mouse at each time point. Whole body BLI signal was measured the same way as listed above with the ROI drawn around the whole mouse body. MRI images were analyzed using OsiriX software (Pixmeo, SARL, Bernex, Switzerland). For days 0 and 7 images, total brain signal void number, representing iron labeled cancer cells, was determined by manually counting voids in every MR slice. For day 14 images, brain metastases were manually traced in every bSSFP image slice for each mouse and 3D tumour volumes were reconstructed using the OsiriX volume algorithm.

3.2.7 Cryo-Fluorescence Imaging

After endpoint MR imaging (day 14), one large MFP and one control mouse were sacrificed by isoflurane overdose and then flash frozen in OCT freezing medium by liquid nitrogen immersion. The entire mouse was sectioned and optically imaged every 50-μm using a cryo-fluorescence imager (CryoViz™; Bioinvision, Inc., Cleveland, OH). Block-face images were collected with an in-plane resolution of 10.5×10.5 μm^2. Brightfield and fluorescent images were acquired, stitched together and visualized using proprietary software (Bioinvision, Inc).

3.2.8 Histology

At endpoint, the majority of mice (n=26) were sacrificed by isoflurane overdose and perfused with 4% paraformaldehyde via the left ventricle. Mouse brains were removed and cryopreserved in ascending concentrations of sucrose (10, 20, and 30% w/v) for 24 hours each. Brains were immersed in optimal cutting temperature (OCT) compound, oriented in a sectioning plane parallel to that of MRI, and frozen using liquid nitrogen. Contiguous 10-μm frozen sections were collected and select sections were stained with hematoxylin and eosin (H&E). Stained sections were imaged using an Invitrogen EVOS FL Auto Cell Imaging System and histological images were manually matched to MR slices using anatomical landmarks such as the ventricles and MR-visible tumours. Fluorescence images of 4T1BR5-Red-FLuc/GFP cancer cells were also collected on the same microscope and matched to MR slices. Spleens were collected and weighed. Contiguous 10-μm paraffin embedded sections were collected, select sections were stained with H&E, and imaged

using a Zeiss 510 laser scanning confocal microscope.

3.2.9 Statistics

A power analysis was performed using G*Power software to determine the appropriate sample size for this study. All statistics were calculated using GraphPad Prism 4. A Shapiro-Wilk normality test found that some of our *in vitro* data was not normally distributed and thus, a non-parametric test (Mann-Whitney) was performed on proliferation experiments. Pearson's rank correlation was used to determine a relationship between cell number and BLI signal. Student's two-tailed unpaired t test was used to compare the other *in vitro* experiments as well as between animal groups. A nominal p-value less than 0.05 was considered statistically significant.

3.3 Results

3.3.1 In Vitro Studies

4T1-BR5 cells were 85.4% transduced with a lentiviral vector and sorted to stably co-express Red-FLuc/GFP (Suppl. 1A/B). The resultant 4T1BR5-Red-FLuc/GFP cells were efficiently (>90%) labeled with MPIO prior to intracardiac injection (Suppl. 1C). There was no significant difference in BLI signal detected in 4T1BR5-Red-FLuc/GFP cells that were labeled with MPIO (2.14 x 10^7 ± 1.37 x 10^6 p/s/mm^2/sr) compared to those that were not labeled (2.48 x 10^7 ± 1.80 x 10^6 p/s/mm^2/sr) (Suppl. 1D). Furthermore, a significant positive correlation was detected between the number of 4T1BR5-Red-FLuc/GFP cells and BLI signal (R^2 = 0.98, *p<0.01*; Suppl. 2A). There were no differences in cellular proliferation detected between naïve 4T1-BR5 and 4T1BR5-Red-FLuc/GFP cells (Suppl.

2B). 4T1-BR5-Red-Fluc/GFP cells also showed no significant change in Red-Fluc expression over multiple passages in culture (Suppl. 2C).

3.3.2 In Vivo Studies

We first looked at imaging data from the day of intracardiac injection (Day 0) shown in Figure 3.1. Iron labeled cells were visualized in MR images as discrete signal voids distributed throughout the mouse brain (Figure 3.1B, 3.1C). Across all 32 mice with a successful intracardiac injection, an average of 98 ± 5 discrete signal voids per mouse were quantified throughout the brains in MR images. The number of discrete signal voids on day 0 was not significantly different between mice with (100 ± 7 voids) and without (121 ± 10 voids) a small primary MFP tumour (Figure 3.1D). Similarly, the number of discrete signal voids on day 0 was not significantly different between mice with (86 ± 5 voids) and without (87 ± 6 voids) a large primary MFP tumour (Figure 3.1D). BLI signal was also detected in the brain of these thirty-two mice on day 0 (Figure 3.1B, 3.1C). We found no significant difference in brain BLI signal between mice with ($4.4x10^4 \pm 8.5x10^3$ p/s/mm^2/sr) and without ($4.7x10^4 \pm 7.8 x10^3$ p/s/mm^2/sr) a small primary MFP tumour, nor with ($2.9x10^4 \pm 6.8x10^3$ p/s/mm^2/sr) or without ($3.3x10^4 \pm 8.7x10^3$ p/s/mm^2/sr) a large primary MFP tumour (Figure 3.1E).

All MFP tumors were manually assessed with caliper measurements throughout the study. We found a significant difference in Small MFP tumour volume between days 0 (time of intracardiac injection; 138.8 ± 12.11 mm^3) and 14 (endpoint; 666.4 ± 20.89 mm^3; p<0.001).

Similarly, we found a significant difference in Large MFP tumour volume between days 0 (308.4 ± 9.14 mm^3) and 14 (817.9 ± 15.12 mm^3).

For mice in the small MFP experiment we looked at imaging data over time and Figure 3.2 illustrates the MRI and BLI signal loss over time representing viable cancer cell clearance in the brain for BLI as well as potential iron label dilution in MR images. The number of signal voids in the brain significantly decreased from day 0 (109.9 ± 7.58 voids) to 7 (7 ± 0.27 voids) for control mice and from day 0 (92.88 ± 6.96) to 7 (7.75 ± 0.70; p<0.0001; Figure 3.2B) for small MFP mice. BLI signal in the brain also significantly decreased for control mice from day 0 (5.1x10^4 ± 5.8x10^3 p/s/mm^2/sr) to 7 (1.5x10^4 ± 3.6x10^3 p/s/mm^2/sr) and for small MFP mice from day 0 (4.4x10^5 ± 8.5x10^3) to day 7 (2.9x10^5 ± 9.8x10^3; p<0.01; Figure 3.2C).

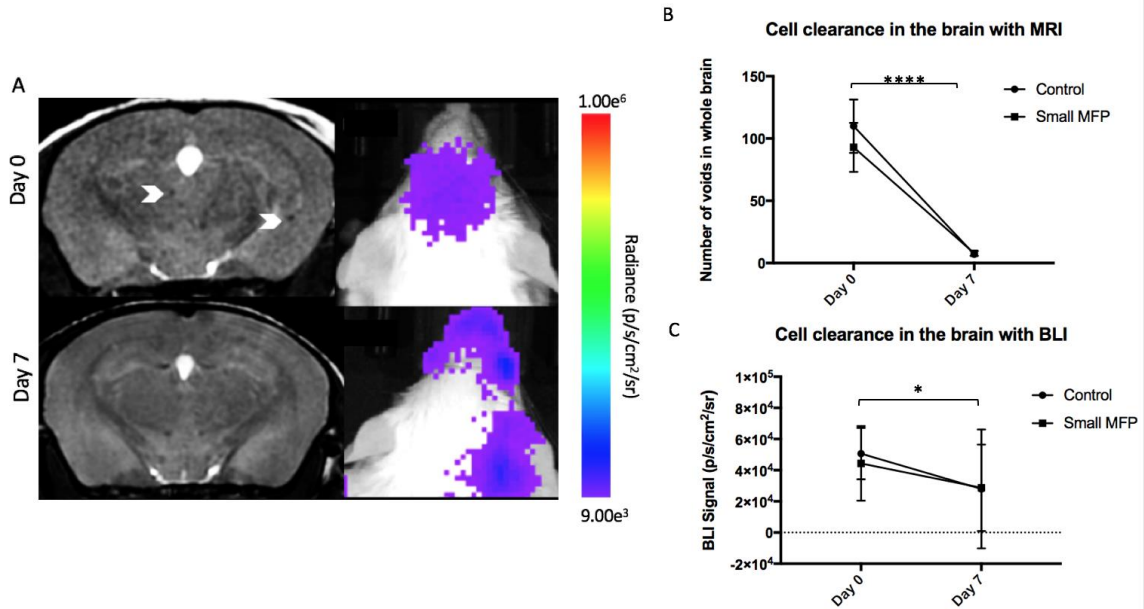**Figure 3.2 Cell clearance imaging: A) BLI and MR imaging data illustrates the signal loss over time with cell clearance in the brain of small MFP and control mice. B) The number of signal voids in the brain decreases from days 0 to 7 as cancer cells are cleared from the brain. C) BLI signal also decreases from day 0 to 7 as cancer cells are cleared from the brain. Data is presented as mean +/- SD. * indicates p<0.05.**

At day 14, brain metastases appeared as regions of hyperintensity by MRI in all twenty-nine mice that made it to endpoint as well as two large MFP mice that had an early endpoint of day 10 due to illness (Figure 3.3 - Small MFP group; Figure 3.4 – Large MFP group). An additional mouse in the large MFP group had to be sacrificed at day 9 due to signs of illness but endpoint MRI was not performed and thus this mouse was not included in our endpoint analysis. Figures 3.3A, 3.4A show an MR slice from a representative mouse from each group. MR image analysis revealed that mice with a small primary MFP tumour $(13.63 \pm 2.05$ tumours) had significantly more brain metastases than control mice $(6 \pm 0.84$ tumours) (Figure 3.3C). We also found that mice with a small MFP tumour $(2.38 \pm 0.55$ mm^3) had significantly higher total brain tumour volume than control mice $(0.72 \pm 0.17$ mm^3) (Figure 3.3D). Similarly, we found that mice with a large primary MFP tumour $(30 \pm 2.22$ tumours) had significantly more brain metastases than control mice $(12 \pm 1.48$ tumours) (Figure 3.4C). We also found that mice with a large MFP tumour $(4.81 \pm 0.59$ mm^3) had significantly increased total brain tumour volume than control mice $(1.65 \pm 0.44$ mm^3) (Figure 3.4D).

Figures 3B/4B show BLI images of a representative mouse from each group at endpoint (day 14). All 13 MFP mice that made it to endpoint had BLI signal in the brain while only 13 of 16 control mice had signal in the brain. An additional 2 MFP mice (large) had BLI signal in the brain at day 10 (day of sacrifice) which were included in our endpoint measurements of brain tumour burden. BLI signal in the brain at endpoint was not significantly different between mice with $(1.1 \times 10^5 \pm 5.1 \times 10^4$ p/s/mm^2/sr) and without (4.3 $\times 10^4 \pm 3.5 \times 10^5$ p/s/mm^2/sr) a small MFP tumour (Figure 3.3E). However, BLI signal in the

brain at endpoint was significantly different between mice with ($5.9 \times 10^4 \pm 2.2 \times 10^4$ p/s/mm^2/sr) and without ($1.1 \times 10^4 \pm 4.7 \times 10^3$ p/s/mm^2/sr) a large MFP tumour (Figure 3.4E). All MFP and control mice had BLI signal in the body at endpoint. Similarly, whole body BLI signal was not significantly different between mice with ($1.2 \times 10^7 \pm 5.9 \times 10^6$ p/s/mm^2/sr) and without ($4.5 \times 10^6 \pm 2.5 \times 10^6$ p/s/mm^2/sr) a primary MFP tumour (Figure 3.3F) or between mice with ($3.1 \times 10^5 \pm 1.7 \times 10^5$ p/s/mm^2/sr) and without ($1.2 \times 10^5 \pm 7.9 \times 10^4$ p/s/mm^2/sr) a large MFP tumour (Figure 3.4F).

Figure 3.3 Endpoint imaging for small MFP mice: A) At day 14, brain metastases appeared as regions of hyperintensity by MRI, and B) regions of BLI signal in the brain and body. C) Mice with a primary small MFP tumor had significantly more brain metastases than mice without a primary tumor. D) Mice with a primary tumor had significantly more total brain tumor burden than mice without a primary small MFP tumor. E/F) There were no significant differences in BLI signal in the brain or body between mice with and without a primary small MFP tumour. Data is presented as mean +/- SD. * indicates p<0.05; ** indicates p<0.01.
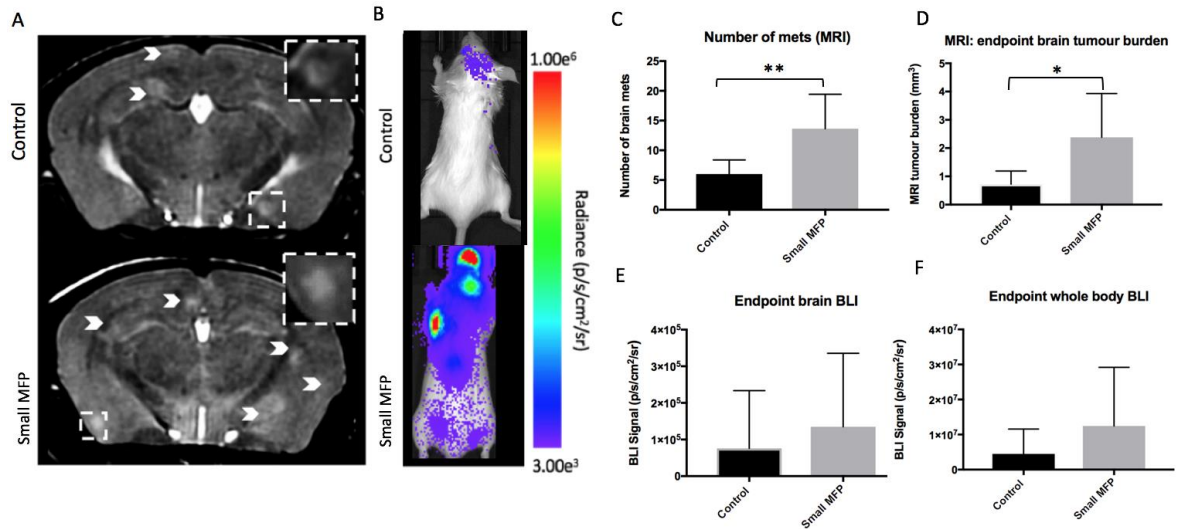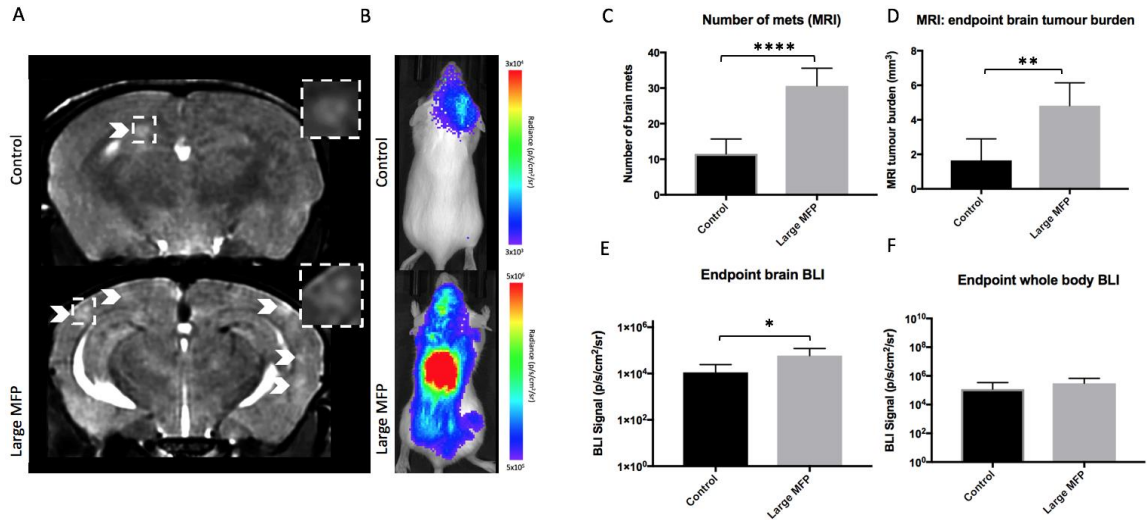
Figure 3.4 Endpoint imaging for large MFP mice: A) At day 14, brain metastases appeared as regions of hyperintensity by MRI, and B) regions of BLI signal in the brain and body. C) Mice with a large MFP tumor had significantly more brain metastases than mice without a primary tumor. D) Mice with a large MFP tumour had significantly more total brain tumor burden than mice without a primary tumor. E/F) Similarly, mice with a large MFP tumour had significantly more BLI signal in both the brain and the body compared to control mice. Data is presented as mean +/- SD. * indicates p<0.05; ** indicates p<0.01.

3.3.3 Histology and whole-mouse cryo-fluorescence imaging

In one large MFP mouse, lung metastases were detectable in whole-body MR images but not in the respective control mouse (Suppl. 3.3). In one small MFP mouse the presence of tumours was also confirmed in *ex vivo* BLI (Suppl. 3.4). Coronal MR images show corresponding orientation to BLI signal; *in vivo* and *ex vivo* whole body BLI were also matched presenting signal in the abdominal region. Fluorescence microscopy demonstrated that the location of 4T1BR5-Red-FLuc/GFP cells corresponded well with H&E as well as hyperintense signal representing tumors in the corresponding MR slice (Suppl. 3.5). This confirms that metastases detected with MRI contain 4T1BR5-Red-FLuc/GFP cells. In two mice, the presence of tumors was also confirmed using cryo-fluorescence imaging which has the ability to perform whole-body brightfield and fluorescence imaging throughout the entire mouse. Cryo-fluorescence imaging allowed for the detection of metastases at day 14 in both the bone and other areas of the body (Figure 3.5). We were able to match some of the metastases seen with cryo-imaging to MR tumours. Cryo-fluorescence imaging also allowed for the localization of secondary metastases seen with BLI. Due to light scattering and the depth limitation of BLI, we cannot be certain where within the body as well as the number of metastases the signal is coming from; cryo-imaging allows us to further explore a region of interest and find out exactly where the tumor is located. Finally, we found that spleens from large MFP tumour-bearing mice (0.65 ± 0.03g) were enlarged with significantly higher weights compared to spleens collected from control mice (0.15 ± 0.01g) (p<0.0001; Figure 3.6A, 3.6B). Normal spleen histology was observed in control mice but it was found that the spleens isolated from large MFP mice showed a reduction in red pulp compared to control mice (Figure 3.6C).
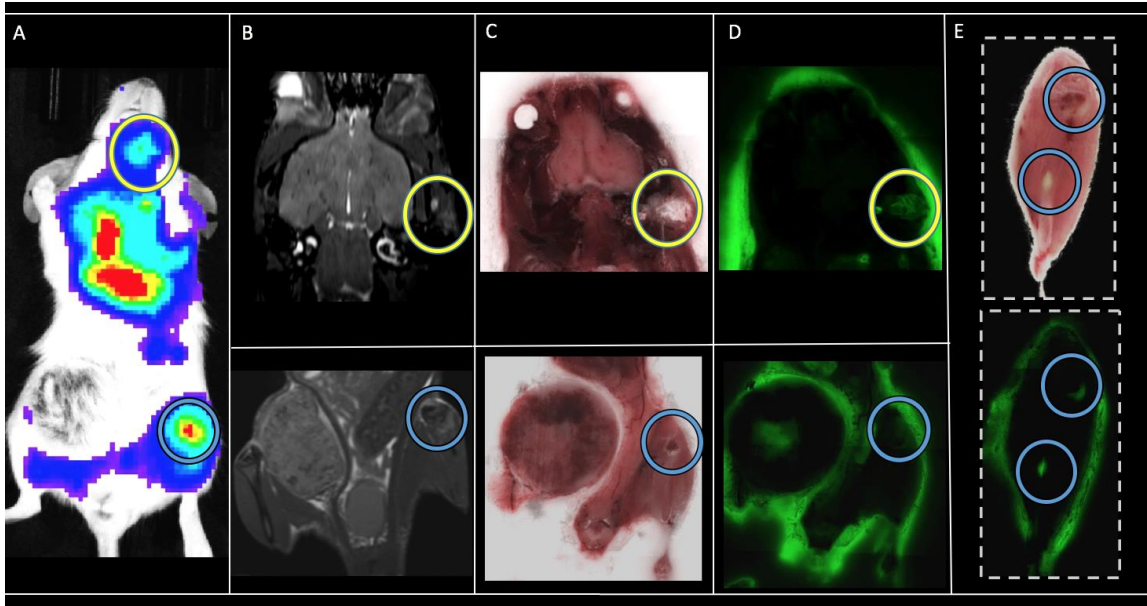
Figure 3.5 Cryoviz Imaging: In a mouse from the large MFP group we were able to detect distant metastases (head circled in yellow; bone circled in blue) with BLI (A) and match them to corresponding MR (B) and brightfield (C/E) and fluorescence (D/E) cryoviz images.
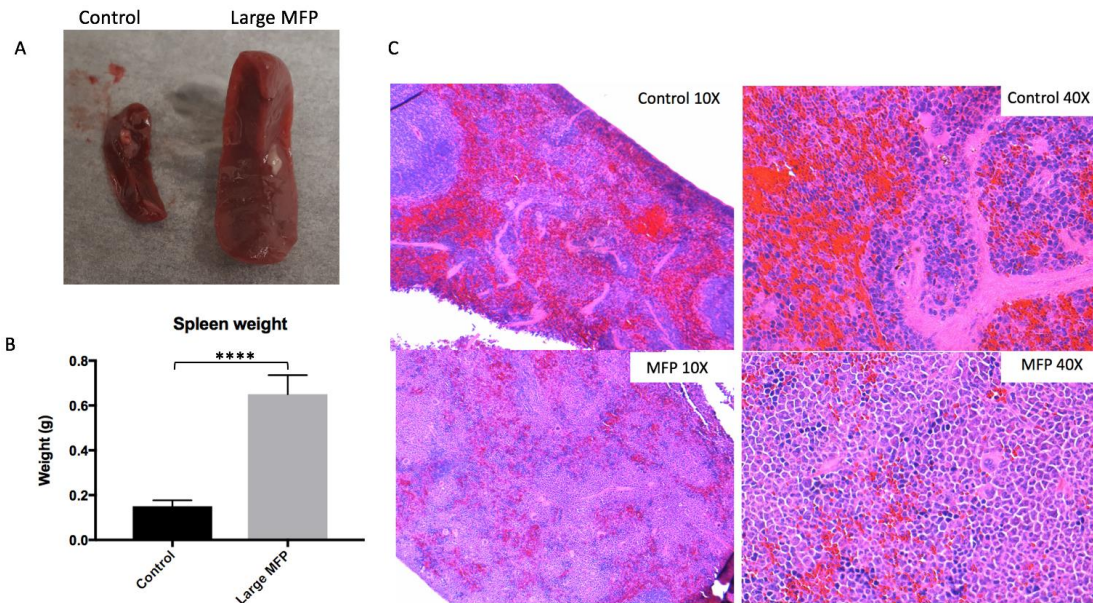
Figure 3.6 Observed splenomegaly: A/B) Spleens from large MFP tumor-bearing mice were enlarged and significantly higher in weight(g) than spleens collected from control mice. C) Normal spleen histology was observed in control mice (Top) but it was found that the spleens isolated from large MFP mice showed a reduction in red pulp (bottom) compared to control mice and normal spleen histology. Data is presented as mean +/- SD. ** indicates $p<0.0001$.**

3.4 Discussion

Clinical and experimental evidence suggests that a primary tumour can both accelerate (CTE) or retard (CTR) the growth of distant metastases[4-14]. In this study, we found CTE effects in the syngeneic 4T1 model using multimodality imaging. The presence of a primary MFP tumour increased the number and total volume of brain metastases as measured with MRI and BLI (in the large MFP group). Secondly, this effect was amplified when the primary tumour was larger at the time of secondary injection of experimental metastatic cells. To our knowledge, this is the first report of multimodality imaging being used to study the impact of a primary tumour on metastatic outgrowth in the 4T1 model.

In our previous studies in immune compromised mice (nu/nu) we found the presence of a human primary breast tumour (MDA-MB-231) significantly inhibited the growth of MDA-MB-231BR brain metastases (i.e., a CTR effect)[16]. For this study, MRI revealed fewer brain metastases developed in mice with than without a primary tumour. Interestingly, using cellular MRI, we also found that significantly more signal voids (representing non-dividing cancer cells) persisted in endpoint images of mice that had a primary tumour compared to mice that did not. This highlighted that a primary tumour can in part maintain cancer cell dormancy and mitigate overt metastases formation, a potential new mechanism for CTR. We could not assess endpoint signal void number in the current study due to the very low number of cells arresting and remaining in the brain at endpoint. In future studies, we could shorten the experimental timeline to enable a greater number of cells injected into the heart, which in turn could result in more voids persisting at endpoint.

Our results between the two models suggests the immune system may play a role in mediating CTR or CTE effects, as also suggested previously by others. Janik et al., found that immune competent mice are first protected and then made more susceptible to the growth of lung metastases by the presence of a progressively growing primary tumour[7]. Similarly, Vaage et al., showed that immunity decreases around day 20 after implanting tumour cells into mice and that this phenomenon was associated with an excess of tumour antigen, and that after removal of the primary tumour immunity is quickly restored[26]. This may provide support as to why we found an amplified CTE effect in our large MFP mice. This cohort of mice had 14 days of primary tumour growth (compared to 7 days in small MFP mice) before secondary injection, followed by 14 days of metastatic growth. This theoretical 20-day period would fall fairly early (6 days) into the period of metastatic growth, leaving these mice vulnerable to enhanced metastatic growth due to decreased immunity. Whether the immune system is playing a significant role in the CTE effects seen in this study could be determined by moving our 4T1/4T1BR5 model from BALB/c mice into an immune compromised mouse (e.g., nu/nu), expecting either a CTR effect or a lesser CTE effect than seen in the present study. Similarly, we may see a more significant CTR effect by studying the MDA-MB-231/MDA-MB231BR model into more immune deficient mice than used before (nu/nu) such as nod-scid-gamma (NSG) mice, or evaluating whether a CTE effect might appear in humanized mice.

An immunological component to the CTE effects seen is also suggested from our findings in the spleens from our animals. We found splenomegaly in tumour-bearing mice however, this finding was associated with a reduction in red pulp and not differences in white pulp.

Kirstein et al., found splenomegaly in tumour-bearing animals was associated with tri-lineage extramedullary hematopoiesis as well as a reduction in white pulp in their mouse model of CTR[14]. Other groups have also seen splenomegaly in tumour-bearing animals, specifically in the 4T1-model. Thus, differences in the ratio of red vs. white pulp in splenic tissue needs to be studied further to determine whether this is an effect of prolonged 4T1 tumor growth or an effect of CTE.

Past studies have shown that the size of the primary tumour plays a key role in whether a CTE or CTR effect is observed. For instance, Bruzzo et al., previously demonstrated secondary tumour growth can be either stimulated or inhibited depending on the ratio between the mass of the primary tumour relative to that of the secondary tumour implant. They found that high ratios tended to cause inhibition of secondary tumour growth while low ratios induced a stimulation effect[8]. For the present study, we injected our secondary cancer cell line at an early time point (7 days post MFP injection) when the primary MFP tumour is relatively small. We did this in an effort to best match the size of our MDA-MB-231 model at the time of secondary injection. However, despite similar primary tumour size at the time of secondary injection, these two models produced opposite effects (CTE/CTR). This may be due to differences in cell line aggressiveness; 4T1 metastases can be detected as early as 7 days whereas the less aggressive MDA-MB-231 model may take between 2-3 weeks before metastases start to form in the brain. This is significantly more time for the MDA-MB-231 primary tumour to grow (increasing the ratio between primary and secondary) to produce a CTR effect on secondary tumour growth. In the 4T1 model, as metastases quickly develop, the ratio between primary and secondary tumours

becomes smaller over time. In the current study, we also injected a second cohort of animals at a late time point (14 days post MFP injection) when the primary tumour is relatively large to try to increase the ratio between primary and secondary tumour (producing a CTR effect). However, we found that increasing the size of the primary tumour at the time of secondary injection significantly amplified our CTE effect.

An important step in the metastatic cascade is the initial arrest of cancer cells. When cancer cells enter the circulation, they can travel through the bloodstream and arrest in the capillary beds of distant sites throughout the body and extrasvasate into the interstitial space where they can begin to form new tumours. For breast cancer patients, metastases are most commonly found in the brain, bone, lung and liver[25]. Our multimodality imaging tools allow us to noninvasively monitor both the number (MRI) and viability (BLI) of arrested single cancer cells in the brain, allowing us to for the first time study the effect of a primary tumour on cancer cell arrest as well as cancer cell clearance. In the present study, we found there was not a significant difference in viable cancer cell arrest in the brain between mice with a primary MFP tumour and control mice. We also found that there was not a significant difference in cancer cell clearance from the brain, suggesting the presence of a primary MFP tumour does not influence the number of viable, iron labeled cancer cells that arrest in the brain at day 0, nor does it affect the clearance of these cells, indicating that in this model the increased tumour growth we detected in mice with primary tumors at endpoint is not due to effects at the early stages of the metastatic cascade. Another important step is the intravasation of cells from the primary tumour. We will explore this

115

in the future by evaluating the effects of removal of the primary tumour on spontaneous metastasis formation.

BLI was performed at endpoint on all mice to measure viable tumour burden in both the brain as well as whole body. Although our MR analysis shows a strong CTE effect in the brain of both the small and large MFP mice, we only found significant differences in brain bioluminescence signal between mice with a large primary MFP tumour and control mice. Previous studies have also shown disagreement in tumour volume and BLI measurements at endpoint[27,28]. Although surprising, it should be noted that MRI and BLI are measuring two different tumour characteristics; MRI is measuring tumour volume, which is affected by many things including the number of tumour or stromal cells present and the presence of edema, amongst other things, whereas BLI is providing a measure of the viability of the engineered cancer cells over time. Moreover, BLI is not without its caveats, particularly when studying metastatic disease. First, BLI signal is depth dependent. Small shallow tumours will appear brighter or equivalent in signal to larger deep tumours. Hence, BLI should be used for monitoring relative tumour viability over time rather than considering BLI signal at any one-time point to represent a direct measure of absolute tumour burden. Second, necrosis may be present within some of the metastases. While our MRI tumour burden may be composed of both live and dead tumour tissue, BLI signal is representative of viable cancer cells only. Third, any areas of hypoxia in a tumour may demonstrate lower BLI signal due to the need for oxygen in the luciferase/luciferin reaction. Despite these caveats, our previous work has shown that the information provided by both imaging

116

modalities over time makes them very complementary technologies for studying cancer metastasis[18].

To account for the possibility of spontaneous metastases developing from our naïve primary cell line and contributing to the main findings in this study, our metastatic cell line was engineered to express GFP. As a result, we can confirm that any GFP-positive metastases came from our intracardiac injection of metastatic cells, whereas GFP-negative metastases are likely spontaneous metastases. In our endpoint histology, we did not find any GFP-negative metastases (all 19 tumours found were GFP-positive), suggesting that all brain metastases detected with MRI at endpoint came from our metastatic cell line and not the primary tumour. In addition, we performed a study where we injected 300,000 4T1-FLuc-GFP cells into the mammary fat pad of immune competent mice. We then monitored primary tumour growth over 28 days with BLI. In this 4-week period we were not able to detect distant metastases in the brain or any other organ. Since BLI is more sensitive than MRI, we can be fairly confident that there are also not any MR-detectable metastases at this time point. This has also been shown by other groups studying spontaneous metastasis of 4T1 cells with BLI[29]. For example, Tao *et al.,* shows that by week 6 after mammary fat pad injection of $1x10^6$ 4T1 cells, only 1 of 6 mice had BLI-detectable metastases in the brain. This is more than three times the number of cells that we are injecting for the current study and thus, we do not expect spontaneous metastases to form in our 4-week time line. In this study, we also show significant differences in endpoint tumour burden in the brain with BLI measures. If a large portion of the MRI tumour burden was from spontaneous

metastases, we predict we would not have seen the differences we found in our BLI measurements.

3.5   Conclusion

In this work, we applied cellular and molecular imaging tools to evaluate the effect of a primary breast tumour and its size on the growth of brain metastases in the immune competent 4T1 mouse model. We found total brain tumour burden was significantly greater in mice with a primary MFP tumour (Small or Large) compared to those without. We also found that mice with a large MFP tumour had significantly more BLI signal in the brain at endpoint compared to control mice. Interestingly, using *in vivo* BLI and MRI we could determine that these differences in endpoint tumour burden were not related to differences in the initial arrest or clearance of viable cells in the brain, which suggests that the presence of a primary tumour can increase the proliferative growth of brain metastases in this syngeneic 4T1 mouse model. Future work will utilize our imaging tools to explore the role of the immune system in promoting or preventing metastatic growth. Understanding the different immunological and/or molecular mechanisms of stimulation (CTE) versus inhibition (CTR) will be extremely valuable in finding new therapeutic options for breast cancer patients.

3.6 References

1. Siegel, R., Ma, J., Zou, Z., Jemal, A. CA: a cancer journal for clinicians. *Cancer Statistics.* **64**, (1):9-29 (2014).

2. Scully, O.J., Bay, B.H., Yip, G., Yu, Y.Breast cancer metastasis. *Cancer Genomics Proteomics*. **9,** (5):311-320 (2012).

3. Chiarella, P., Bruzzo, J., Meiss, R.P., Ruggiero, R.A. Concomitant tumor resistance. *Cancer Lett*. **28,** 324(2): 133-41 (2012).

4. Prehn, R.T. The inhibition of tumor growth by tumor mass. *Cancer Res*. **51,** 2-4 (1991).

5. Demicheli, R., Miceli, R., Moliterni, A., Zambetti, M., Hrushesky, W.J., Retzky, M.W., et al. Breast cancer recurrence dynamics following adjuvant CMF is consistent with tumour dormancy and mastectomy-driven acceleration of the metastatic process. *Ann Oncol* . **16,** 1449-1457 (2005).

6. McAllister, S.S., Gifford, A.M., Greiner, A.L., Kelleher, S.P., Saelzler, M.P., Ince, T.A., et al. Systemic endocrine instigation of indolent tumor growth requires osteopontin. *Cell*. **133,** 994-1005 (2008).

7. Janik, P., Bertram, J.S., Szaniawska, B. Modulation of lung tumor colony formation by a subcutaneously growing tumor. *J Natl Cancer Inst*. **66,** 1155-8 (1981).

8. Bruzzo, J., Chiarella, P., Meiss, R.P., Ruggiero, R.A. Biphasic effect of a primary tumour on the growth of secondary tumour implants. *J Cancer Res Clin Oncol*. **136,** 1605-15 (2010).

9. Vizel, M.W., Oster, J.H., Austin. Spontaneous regression of a pulmonary metastasis after nephrectomy for renal cell carcinoma. *J. Surg. Oncol.* **12,** 175–180 (1979).

10. Lokick, J. Spontaneous regression of metastatic renal cancer: Case report and literature review. *Am. J. Clin. Oncol.* **20,** 416–418 (1997).

11. Wyczolkowski, M., Klima, W., Bieda, W., Walask, K. Spontaneous regression of hepatic metastases after nephrectomy and mastectomy of renal cell carcinoma. *Urol. Int*. **66,** 119–120 (2001).

12. Lekanidi, K., Vlachou, P.A., Morgan, B., Vasanthan, S. Spontaneous regression of metastatic renal cell carcinoma: case report. *J. Med. Case Reports*. **1,** 89 (2007).

13. El Saghir, N. S., Elhajj, I. I., Geara, F. B., & Hourani, M. H. Trauma-associated growth of suspected dormant micrometastasis. *BMC cancer*. **5(1),** 94 (2005).

14. Kirstein, J. M., Hague, M. N., McGowan, P. M., Tuck, A. B., & Chambers, A. F. Primary melanoma tumor inhibits metastasis through alterations in systemic hemostasis. *Journal of Molecular Medicine*. **94(8),** 899-910 (2016).

15. Franco, M., Bustuoabad, O. D., Di Gianni, P. D., Goldman, A., Pasqualini, C. D., & Ruggiero, R. A. A serum-mediated mechanism for concomitant resistance shared by immunogenic and non-immunogenic murine tumours. *British journal of cancer*. **74(2),** 178 (1996).

16. Hamilton, A.M., Parkins, K.M., Murrell, D.H., Ronald, J.A., Foster, P.J. Investigating the Impact of a Primary Tumor on Metastasis and Dormancy Using MRI: New Insights into the Mechanism of Concomitant Tumor Resistance. *Tomography. 2 (2), 79-84* (2016).

17. Shapiro, E.M., Skrtic, S., Sharer, K., Hill, J.M., Dunbar, C.E., Koretsky, A.P. MRI detection of single particles for cellular imaging, *Proc Natl Acad Sci USA*. **101,** 10901- 10906 (2004).

18. Parkins, K. M., Hamilton, A. M., Makela, A. V., Chen, Y., Foster, P. J., & Ronald, J. A. A multimodality imaging model to track viable breast cancer cells from single arrest to metastasis in the mouse brain. *Sci. Rep. 6,* 35889 (2016)

19. McFadden, C., Mallett, C.L., Foster, P.J. Labeling of multiple cell lines using a new iron oxide agent for cell tracking by MRI. *Contrast Media Mol Imaging*. **6(6),** 514–522 (2011).

20. Euhus, D.M., Hudd, C., LaRegina, M.C., Johnson, F.E. Tumor measurement in the nude mouse. *J Surg Oncol.* **31,** 229-234 (1986).

21. Tomayko, M.M., Reynolds, C.P. Determination of subcutaneous tumor size in athymic (nude) mice. *Cancer Chemother. Pharmacol.* **24,** 148-154 (1989).

22. Heyn, C., Bowen, C., Rutt, B. & Foster, P. Detection threshold of single SPIO-labeled cells

    with FIESTA. *Magnet Reson Med.* **53,** 312-320 (2005).

23. Heyn, C. et al. In vivo MRI of cancer cell fate at the single-cell level in a mouse model of breast cancer metastasis to the brain. *Magn Reson Med.* **56,** 1001-1010 (2006).

24. Ribot, E. *et al*. In vivo single scan detection of both iron-labeled cells and breast cancer

    metastases in the mouse brain using balanced steady-state free precession imaging at 1.5 T. *J. Magn Reson Imaging.* **34,** 231-238 (2011).

25. Parker, B., Sukumar, S. Distant metastasis in breast cancer: molecular mechanisms and therapeutic targets. *Cancer Biol Ther.* **2,**14–21 (2003).

26. Vaage, Y. Free tumor antigen and immune serum factors in control of metastasis. *Gan Monogr Cancer Res.* **20,** 129-145 (1977).

27. Song, H.T., Jordan, E.K., Lewis, B.K., Liu, W., Ganjei, J., Klaunberg, Frank, J.A. Rat model of metastatic breast cancer monitored by MRI at 3 tesla and bioluminescence imaging with histological correlation. *Journal of translational medicine.* **7(1),** 88 (2009).

28. Black, P.C., Shetty, A., Brown, G.A., Esparza-Coss, E., Metwalli, A.R., Agarwal, P.K., Dinney, C.P. Validating bladder cancer xenograft bioluminescence with magnetic resonance imaging: the significance of hypoxia and necrosis. *BJU international.* **106(11),** 1799-1804 (2010).

29. Tao, K., Fang, M., Alroy, J., Sahagian, G.G. Imagable 4T1 model for the study of late stage breast cancer. *BMC cancer.* **8(1),** 228 (2008).

Chapter 4

4 Engineered self-homing circulating tumour cells as novel metastatic breast cancer theranostics

Purpose: New ways to target and treat metastatic disease are urgently needed. Tumor "self-homing" describes the recruitment of circulating tumor cells (CTCs) back to a previously excised primary tumor location, contributing to tumor recurrence, as well as their migration to established metastatic lesions. Recently, self-homing CTCs have been exploited as delivery vehicles for anti-cancer therapeutics in preclinical primary tumor models. However, the ability of CTCs to self-home and treat metastatic disease is largely unknown. **Methods:** Here, we employ molecular imaging to explore whether systemically-administered CTCs home to metastatic lesions and if CTCs armed with both a reporter gene and a cytotoxic prodrug gene therapy can be used to visualize and treat metastatic disease. **Results:** Bioluminescence imaging (BLI) performed over time revealed a remarkable ability of CTCs to home to primary and metastatic tumors throughout the body. Mice that received therapeutic CTCs had less BLI signal as well as less primary tumour burden than control mice. Preliminary data also showed self-homing therapeutic CTCs may be effective at treating disseminated breast cancer metastases. **Conclusion:** Using dual-luciferase BLI, this study demonstrates the noteworthy ability of experimental CTCs to home to disseminated breast cancer lesions. Moreover, by incorporating a prodrug gene therapy system into our self-homing CTCs, we show exciting progress towards effective and targeted delivery of gene-based therapeutics to treat both primary and metastatic lesions.

4.1 Introduction

Cancer patient outcomes have significantly improved in the last few decades due to superior cancer imaging, surgical, and radiotherapy techniques, the recent application of 'omics' lesion profiling to guide therapy, and more efficacious drugs [1]. These advances now allow many patients with localized primary tumours or minimal metastatic disease at the time of diagnosis, or during recurrence, to be effectively managed. Yet despite these transformative advances, the ability to benefit patients with highly disseminated metastatic disease remains a significant challenge. Difficulties with controlling metastatic disease include, but are not limited to, the lack of tools to visualize lesions at an earlier stage when they may be more readily treated, insufficient systemic delivery of therapeutics to all lesions, and, most notably, extensive tumour heterogeneity both within and between lesions throughout the body [2,3]. These substantial barriers highlight an unmet need for new technologies to effectively visualize and treat metastatic lesions, preferably so-called theranostic tools that have both diagnostic and therapeutic capabilities.

Cells are an attractive form of theranostic vector as they can be readily engineered *ex vivo* prior to transplantation with both molecular-genetic imaging reporter genes for noninvasive localization and therapeutic transgenes [4-7]. While some cell types have been shown to naturally home to lesions, such as stem cells and immune cells [8-14], one can also engineer cells with receptors targeting tumour-associated antigens to redirect *in vivo* cellular tropism. Recently, chimeric antigen receptor T cells (CAR-T cells) targeting the B cell antigen CD-19 became the first genetically-modified cell-based therapies to be approved for patients with relapsed or refractory B-cell precursor acute lymphoblastic

leukemia and large B cell lymphoma [15-18]. While substantial efforts are now aimed at using CAR-T cells for the treatment of solid tumours, so far, their less than ideal therapeutic effectiveness has been attributed to insufficient tumour-homing and/or intratumoural immunological barriers [19]. Thus, the continued exploration of alternative cell types that can effectively home to metastatic solid tumours for use as novel theranostic vectors is warranted.

Paget's "seed and soil hypothesis" describes the wide dissemination of "seeds", or circulating tumour cells (CTCs), from a primary tumour and the formation of overt metastases selectively in "soils" that permit CTC survival and proliferation [20]. However, due to the non-permissive nature of tumour-free organs, metastasis has been shown to be an inefficient process in both experimental animal models and cancer patients [21-23]. The impedance of the formation of new metastases has been partly attributed to both vascular barriers that inhibit CTC extravasation from the blood as well as unfavorable survival conditions [24]. Conversely, shed CTCs have been shown to be highly capable of homing back to their tumour of origin, a concept termed tumour "self-seeding" that was first suggested and demonstrated by Kim and colleagues [25]. Self-seeding has been shown in animal models of human breast, colon and melanoma cancer, and is theorized to contribute to tumour recurrence following resection [25]. Unlike in tumour-free organs, tumour vasculature is often "leaky" due to a compromised vascular endothelium, and thus, more easily facilitates the extravasation of CTCs back into their original tumours [26]. Moreover, the primary tumour microenvironment is considered highly permissive soil for the continued survival and growth of recruited CTCs, leading to the expansion of highly

metastatic clones that have a higher capacity to seed distant organs [25]. Similarly, metastatic lesions that have formed in distant organs are also considered fertile soil for additional "self-homing" CTCs to migrate to, survive, and expand within, which may contribute to accelerated metastatic disease progression [25].

In the last two decades, several groups have exploited self-homing CTCs as "self-targeted" delivery vehicles for *ex vivo* loaded anti-cancer therapeutic cargo [27-32]. Cargo has included oncolytic viruses such as the H-1 parvovirus and vesicular stomatitis virus (VSV), prodrug converting enzyme genes including herpes simplex virus thymidine kinase (HSV-TK) and cytosine deaminase (CD), transgenes that target the tumour microenvironment such as tumour necrosis factor (TNF), and the secretory version of TNF-related apoptosis-inducing ligand (S-TRAIL). Additionally, a few groups have co-engineered the therapeutic CTCs and/or their viral cargo with optical or positron emission tomography (PET) imaging reporter genes to enable the fate of the cells/cargo to be monitored with molecular-genetic imaging [28-30, 32]. Importantly, while the ability to target, visualize, and treat singular pre-established subcutaneous tumours as well as orthotopic or metastatic lesions in a singular organ (e.g., lungs [28] or brain [32]) has been demonstrated, to the best of our knowledge, the ability of self-homing CTCs to migrate into and be used to visualize and treat spontaneous multi-organ metastatic disease is largely unknown.

Here, we employed longitudinal molecular-genetic imaging to show that systemically-administered engineered CTCs efficiently home to both orthotopic and spontaneous metastatic breast cancer lesions. Further, we demonstrate that CTCs armed with both an

imaging reporter gene and the gene for the prodrug converting enzyme cytosine deaminase-uracil phosphoribosyltransferase (CD:UPRT) can be used to effectively visualize and treat metastatic disease, resulting in distinctly increased survival times. Our preclinical study supports engineered CTCs as a novel self-targeting cellular theranostic platform for the visualization and treatment of distributed metastases - the most relevant lesions to patient outcome.

4.2   Results
4.2.1 Tracking of Self-Homing Cancer Cells in a Contralateral Orthotopic Tumour Model

Previous studies have shown that breast cancer cells from one mammary fat pad can home into a contralateral mammary fat pad (MFP) tumour [25]. Thus, we first started exploring the use of imaging to monitor tumour self-homing using this same experimental setup. We engineered the mouse breast cancer cell line (4T1) and its brain-seeking metastatic variant (4T1BR5) to express the orthogonal bioluminescence imaging (BLI) reporters *Renilla* luciferase (RLuc) and *Firefly* luciferase (FLuc), respectively.   This allowed us to sensitively track both populations in the same animal over time. 4T1 cells were transduced with a lentiviral vector encoding both RLuc and ZsGreen and sorted to obtain 4T1-RLuc cells (Suppl. 4.1A). No significant change in ZsGreen expression over multiple passages was seen (Suppl. 4.1B) and there was a significant positive correlation shown between the number of 4T1-RLuc cells and RLuc/ZsGreen signal ($R^2 = 0.99$, *p<0.001*; Suppl. 4.1C). FLuc-expressing 4T1BR5 (4T1BR5-FLuc) cells were engineered and characterized similarly in a previous study [33]. We next ensured a lack of cross-reactivity of the

luciferase substrates. 4T1BR5-FLuc cells incubated with D-luciferin demonstrated significantly higher BLI signal than 4T1-RLuc cells, 4T1 parental cells, or equivalent volume of media, and 4T1-RLuc cells did not produce signal significantly different than 4T1 parental cells or media alone *(p<0.001*; Suppl. 4.1D). Similarly, after the addition of h-Coelenterazine, 4T1-RLuc cells had significantly higher signal than 4T1BR5-FLuc cells, 4T1 parental cells, or equivalent volume of media and 4T1BR5-FLuc cells did not produce signal significantly different than 4T1 parental cells or media alone *(p<0.001*; Suppl. 4.1E*)*. We next explored the migration of our engineered cells towards conditioned media from both cell lines using transwell migration assays. A significant increase in cell migration was seen for 4T1BR5-FLuc cells when conditioned media from 4T1-RLuc cells was used compared to conditioned media from 4T1BR5-FLuc cells or unconditioned media *(p<0.01*; Suppl. 4.1F*)*. A significant increase in cell migration was also seen for 4T1-RLuc cells when conditioned media from 4T1-RLuc cells was used compared to unconditioned media *(p<0.01*; Suppl. 4.1F*)*.

4T1-RLuc cells were then implanted into the right MFP of nude mice (n=5) and 4T1BR5-FLuc cells were implanted into the contralateral (left) MFP (Figure 4.1A). This allowed us to validate the lack of substrate cross-reactivity *in vivo* at early time points after cell injection (Days 0 and 1; Figures 4.1 and Suppl. 4.2) as well as the ability to evaluate whether either of the cell lines migrated into the contralateral MFP tumour (Figure 4.1). On Day 0 after cell injection, 4T1-RLuc cells only showed signal after administration with h-coelenterazine and on Day 1, 4T1BR5-FLuc cells only showed signal after administration of D-Luciferin (Suppl. 4.2). By day 7, 4T1BR5-FLuc cells did not appear

128

to migrate as FLuc signal was not detected in the contralateral MFP (Figure 4.1D). In contrast, 4T1-RLuc cells could be detected in the contralateral MFP tumour, and RLuc signal was significantly higher in the contralateral compared to ipsilateral MFP (Figure 4.1C). The presence of both 4T1-RLuc and 4T1BR5-FLuc cells in the left MFP was confirmed histologically (Figure 4.1E, 4.1F), supporting our non-invasive imaging results and validating that the 4T1-RLuc cells left their initial site of implantation and homed to the contralateral MFP tumour.
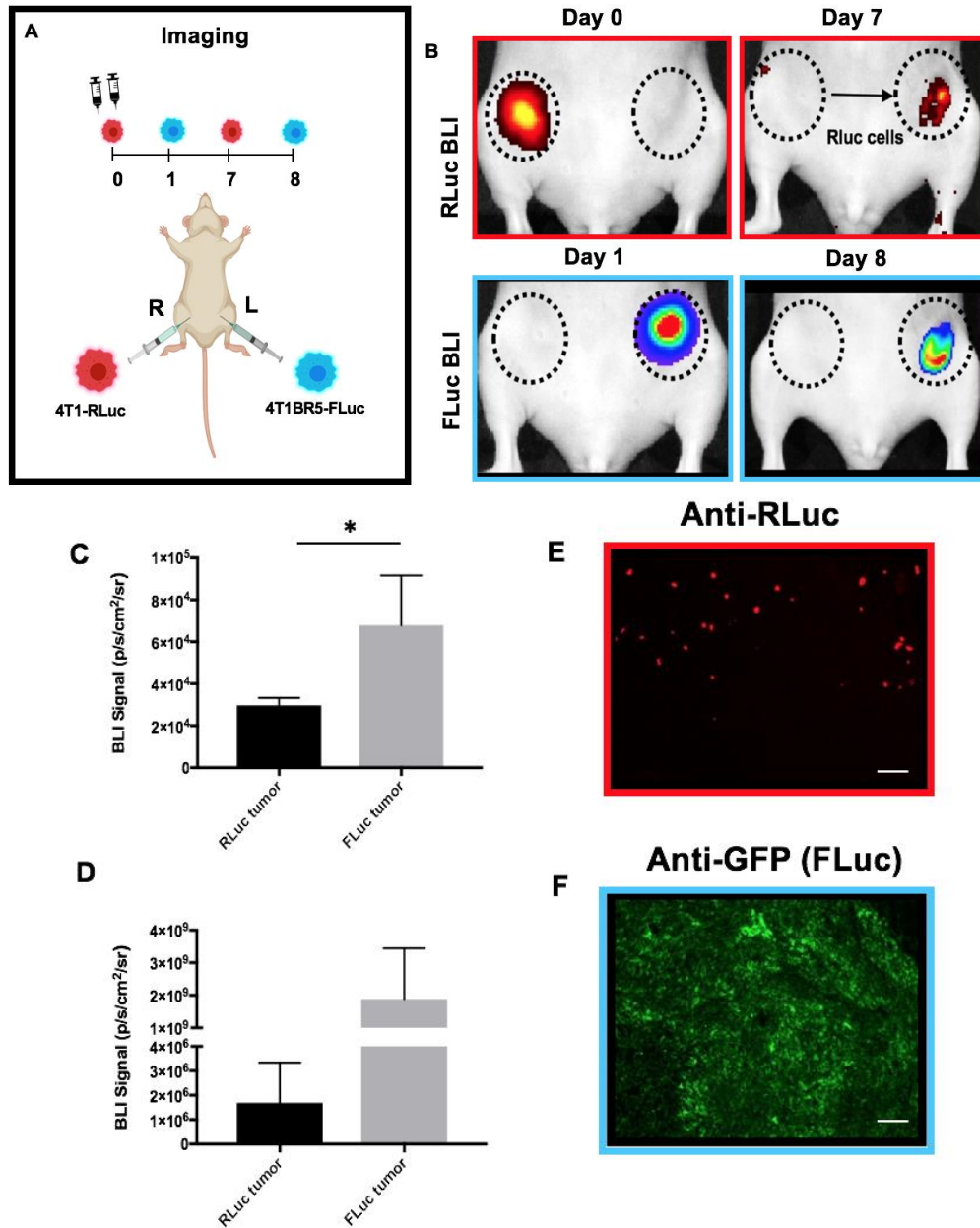
Figure 4.1 Experimental timeline for contralateral tumour self-homing model (n=5): On Day 0 after cell injection, 4T1-RLuc cells only showed signal after administration with h-coelenterazine and on Day 1, 4T1BR5-FLuc cells only showed signal after administration of D-Luciferin. By day 7, 4T1BR5-FLuc cells did not appear to migrate as FLuc signal was not detected in the contralateral MFP but 4T1-RLuc cells could be detected in the contralateral MFP tumour (B). RLuc signal on day 7 was significantly higher in the contralateral MFP compared to the ipsilateral MFP on day 8 (C/D). The presence of both 4T1-RLuc and 4T1BR5-FLuc cells in the left MFP was confirmed histologically (scale bars= 500 microns) (E/F).

4.2.2 Monitoring Self-Targeted Therapy in a Contralateral Orthotopic Tumour Model

We next evaluated the ability of self-homing 4T1-RLuc cells expressing the therapeutic prodrug converting fusion enzyme cytosine deaminase-uracil phosphoribosyltransferase (CD:UPRT) to treat contralateral MFP tumours. CD:UPRT converts non-toxic 5'-fluorocytosine (5'FC) into the cytotoxic compound 5'fluoruridine monophosphate (5'FUMP) and was chosen as a suicide switch to eliminate the therapeutic cells as well as a way to kill adjacent non-engineered cancer cells via the bystander effect [34-37]. 4T1-RLuc and 4T1BR5-FLuc cells were transduced with a lentiviral vector co-expressing CD:UPRT (CD for brevity) and tdTomato (tdT), and sorted via tdT to obtain 4T1-RLuc/CD (4T1-CD) cells and 4T1BR5-FLuc/CD (4T1BR5-CD) cells (Figures 4.2A and Suppl. 4.3A). After 96 hours of incubation with 5'FC (5mM), CD expressing cells showed significantly less survival than cells without drug as well as significantly less survival than 4T1-RLuc and 4T1BR5-FLuc cells with or without drug (Figures 4.2B and Suppl. 4.3B). At all doses (0.005mM, 0.05mM, 0.5mM, 5mM), CD expressing cells show significantly less survival than cells without drug (Figures 4.2C and Suppl. 4.3C).

Figure 4.2 Therapeutic cell characterization: 4T1-RLuc cells were transduced with a lentiviral vector co-expressing the therapeutic prodrug converting fusion enzyme cytosine deaminase-uracil phosphoribosyltransferase (CD:UPRT) and tdTomato (tdT), and sorted via tdT to obtain 4T1-RLuc/CD cells (A). After 96 hours of incubation with 5'FC (5mM), CD expressing cells showed significantly less survival than cells without drug as well as significantly less survival than 4T1-RLuc cells with or without drug (B). At all doses, CD expressing cells show significantly less survival than cells without drug (C).

Next, we performed *in vivo* experiments whereby either 4T1-RLuc (n=4) or 4T1-CD (n=4) cells were implanted into the right MFP and 4T1BR5-FLuc into the contralateral MFP. All mice were treated with 5'FC daily from days 8 to 14 (Figure 4.3A). As visualized with RLuc BLI, on day 7 before treatment, both 4T1-CD and 4T1-RLuc cells can be seen in the contralateral MFP tumour and RLuc signal at this site was not significantly different between mouse cohorts (Figure 4.3B, 4.3C). At day 14 following treatment, FLuc BLI signal was observed in both contralateral and ipsilateral MFPs and signal was not significantly different between the two mouse groups in both MFPs (Figure 4.3E, 4.3F). At endpoint, areas of necrosis were evident in MFP tumours from both mouse cohorts using hematoxylin and eosin (H&E) staining (Figure 4.3G).
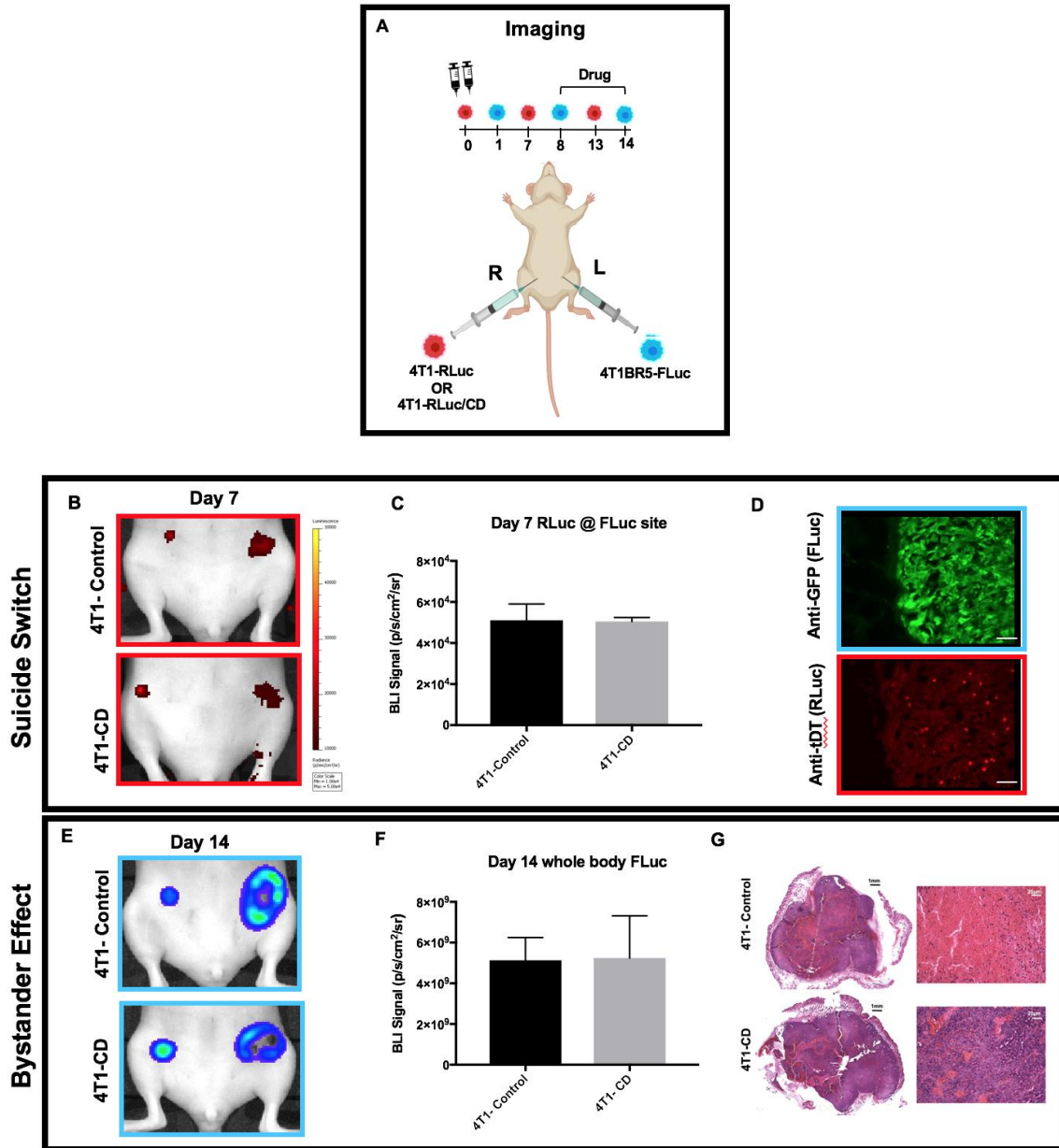
Figure 4.3 Experimental timeline for contralateral tumour treatment (n=8): All mice were treated with 5'FC daily from days 8 to 14. As visualized with RLuc BLI, on day 7 before treatment, both 4T1-RLuc/CD and 4T1-RLuc cells can be seen in the contralateral MFP tumour and RLuc signal at this site was not significantly different between mouse cohorts (B/C). tDT expressing therapeutic cells were visualized in the contralateral MFP using fluorescence microscopy at day 7 before drug administration (scale bars=200 microns). At day 14 following treatment, FLuc BLI signal was observed in both contralateral and ipsilateral MFPs and signal was not significantly different between the two mouse groups (E/F). At endpoint, areas of necrosis were evident in MFP tumours from both mouse cohorts using hematoxylin and eosin (H&E) staining (black scale bars= 1mm; white scale bars= 20 microns) (G).

134

4.2.3 Intratumoural Injection of Therapeutic Cancer Cells Can Treat Orthotopic Tumours

We hypothesized the lack of therapeutic effect in the previous experiment may have been due to insufficient numbers of 4T1-CD cells migrating into the contralateral MFP tumour. Immunostaining of mice sacrificed on day 7 confirmed the presence of both 4T1BR5-FLuc and 4T1-CD cells in the left MFP, but a relatively low ratio of 4T1-CD to 4T1BR5-FLuc cells was noted (Figure 4.3D). To further test our hypothesis, we allowed the 4T1BR5-FLuc tumours to grow for 7 days prior to injecting $3x10^5$ 4T1-RLuc or 4T1-CD cells intratumourally and treated all mice with 5'FC daily from days 8 to 16 (Figure 4.4). 4T1 cells were visualized with RLuc BLI on days 7 and 15, and 4T1BR5 cells with FLuc BLI on days 0, 4, 8 and 16 (Figure 4.4A). Importantly, RLuc BLI of mice intratumourally injected with 4T1-CD cells was significantly higher than in mice that had the same cells home from the contralateral MFP the day prior to treatment initiation (Figure 4.4B, 4.4C). At day 15 after treatment, mice that received 4T1-CD cells intratumourally had a larger percent signal loss of RLuc signal compared to mice that received 4T1-RLuc cells, indicating the ability to mitigate therapeutic cancer cell growth via suicide switch activation (Figure 4.4B, 4.4D). Furthermore, by day 16, mice that received 4T1-CD cells had significantly less FLuc signal compared to mice that received 4T1-RLuc cells, indicating kill of adjacent cells via the bystander effect (Figure 4.4E, 4.4F). Measuring FLuc signal by BLI was complicated by the development of tumour ulcerations in both groups, which partially blocked signal. Large areas of necrosis were seen in histological sections of MFP tumours from both mouse cohorts (Figure 4.4G). Therefore, we also assessed treatment response by measuring MFP tumour volumes over time with calipers. Mice that received 4T1-CD cancer cells had significantly smaller tumour volumes than

control mice at both days 14 and 17 (Figure 4.4H, 4.4I). Of the 4 control mice, 3 had to be sacrificed prior to the day 21 due to predetermined endpoints, either the size of the tumour (> 2cm^3) and/or the presence of excessive ulceration. As a result, 5'FC treated mice that received 4T1-RLuc/CD cells showed significantly improved survival times compared to mice receiving 4T1-RLuc cells (p<0.01; Figure 4.4J).
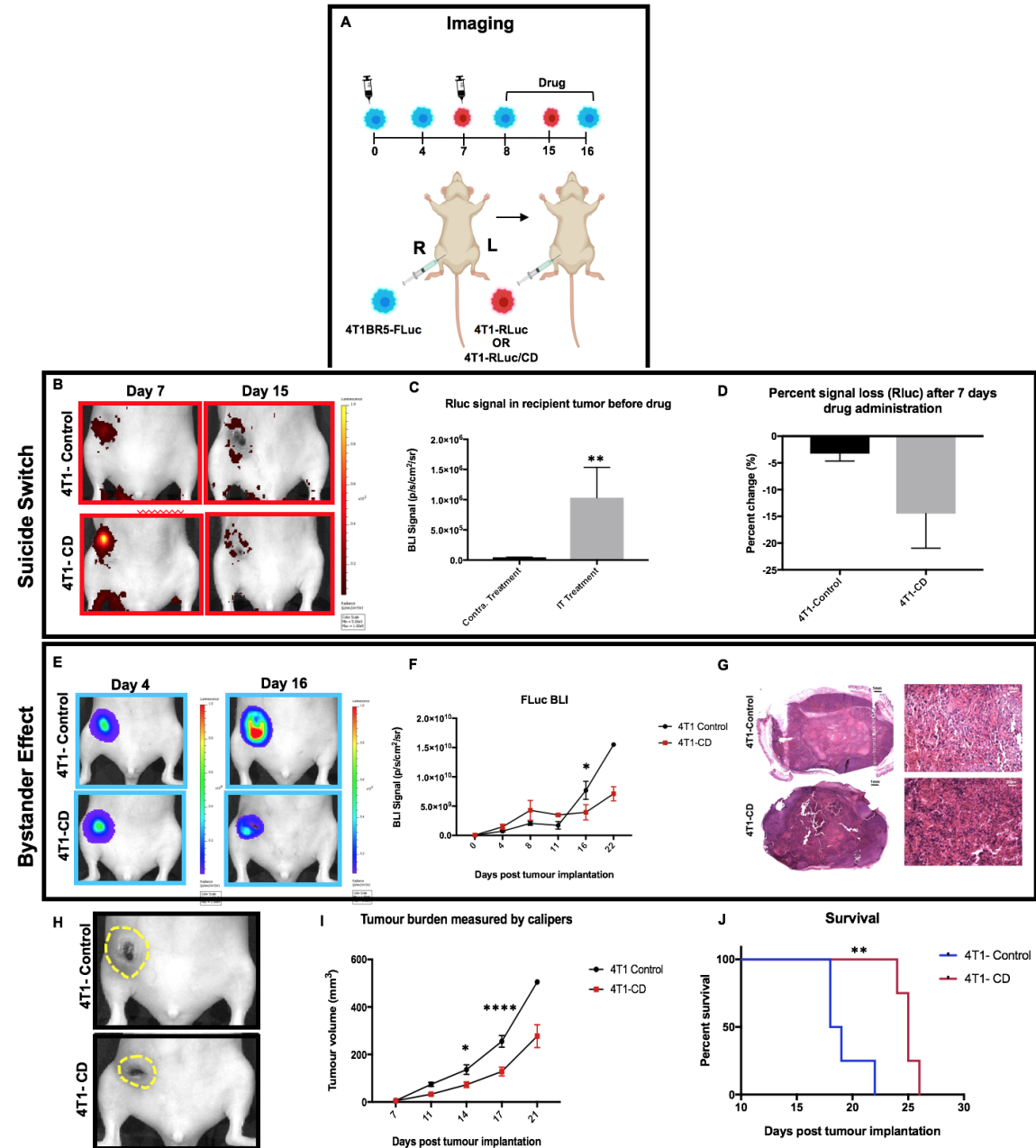
Figure 4.4 Experimental timeline for intratumoural injection of therapeutic cancer cells (n=8): All mice were treated with 5'FC daily from days 8 to 16. 4T1-Rluc and 4T1-RLuc/CD cells were visualized in the left MFP with BLI on days 7 and 15 (B) RLuc BLI of mice intratumourally injected with 4T1-RLuc/CD cells was significantly higher than in mice that had the same cells home from the contralateral MFP the day prior to treatment initiation (C). Mice that received 4T1-RLuc/CD cells intratumourally had a larger percent signal loss of RLuc signal compared to mice that received 4T1-RLuc cells, indicating the ability to mitigate therapeutic cancer cell growth via suicide switch activation (D). Furthermore, by day 16, mice that received 4T1-RLuc/CD cells had significantly less FLuc signal compared to mice that received

4T1-RLuc cells, indicating kill of adjacent cells via the bystander effect (E/F). At endpoint, areas of necrosis were evident in MFP tumours from both mouse cohorts using hematoxylin and eosin (H&E) staining (black scale bars= 1mm; white scale bars= 20 microns) (G). Treatment response was also assessed by measuring MFP tumour volumes over time with calipers. Mice that received 4T1-RLuc/CD cancer cells had significantly smaller tumour volumes than control mice at both days 14 and 17 (H/I). 5'FC treated mice that received 4T1-RLuc/CD cells showed significantly improved survival times compared to mice receiving 4T1-RLuc cells (J).

4.2.4 Primary Tumours and Spontaneous Metastases can be Visualized with Systemically-Administered "Diagnostic" CTCs

We next assessed the ability of systemically-administered CTCs to home to primary tumours and spontaneous metastases. We implanted 4T1-RLuc cells into the right MFP of nude mice (n=5) and allowed tumours to grow for 7 days prior to injecting 4T1BR5-FLuc CTCs via an intracardiac injection under ultrasound guidance (Figure 4.5A). RLuc BLI was performed on days 0, 6, 13 and 19 to visualize cells in the right MFP and any spontaneous metastases and FLuc BLI was performed on days 7, 14 and 20 to visualize CTCs (Figure 4.5A, 4.5B). RLuc BLI showed the presence of metastases in 1 of 5 mice on day 6 prior to CTC injection. RLuc tumours were often found in the brain and/or hind limbs. FLuc BLI over time revealed the ability of FLuc-expressing CTCs to home to RLuc-expressing primary tumours and spontaneous metastases throughout the body (Figure 4.5B). Quantitative analysis of endpoint BLI images (day 19 and 20) revealed that the vast majority of metastases were composed of both 4T1-RLuc and 4T1BR5-FLuc cells (M=9.8±1.9), which was significantly higher than the number of metastases that were either 4T1-RLuc-positive only (M=0.6±0.4; *p<0.01*) or 4T1BR5-FLuc-positive only (M=0.2±0.2; *p<0.001*) (Figures 4.5C, 4.5D, Suppl. 4.4). The presence of both 4T1-RLuc and 4T1BR5-FLuc cells in numerous metastases was confirmed histologically (Figures 4.5E, Suppl. 4.4B), supporting our non-invasive imaging results.
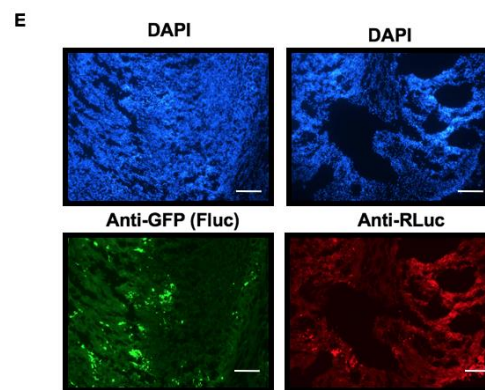
A Imaging

0 6 7 13 14 19 20

R L

4T1-RLuc   4T1BR5-FLuc

B

| | Day 0 RLuc | Day 6 RLuc | Day 7 FLuc | Day 13 RLuc | Day 14 FLuc | Day 19 RLuc | Day 20 FLuc |

Mouse 1
Mouse 2
Mouse 3
Mouse 4
Mouse 5

C

RLuc (Day 19)

FLuc (Day 20)

Mouse 1   Mouse 2   Mouse 3   Mouse 4   Mouse 5

D

Whole body metastasis detected with BLI

● RLuc only   ■ FLuc only   ▲ RLuc/FLuc

Tumor Number

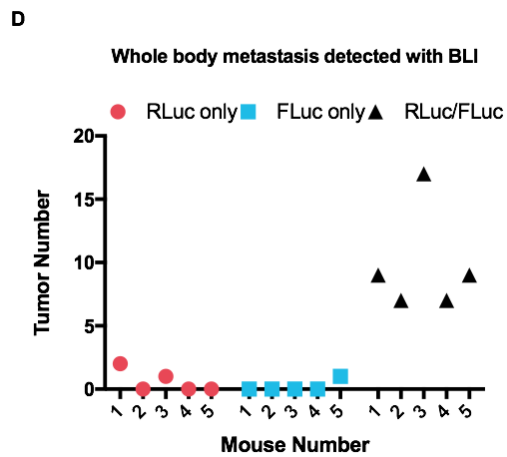Mouse Number

E

DAPI   DAPI
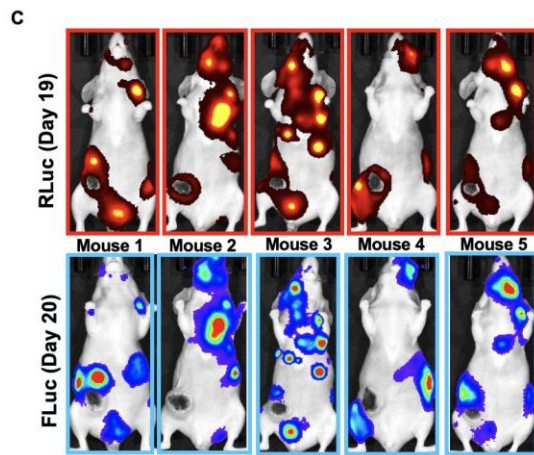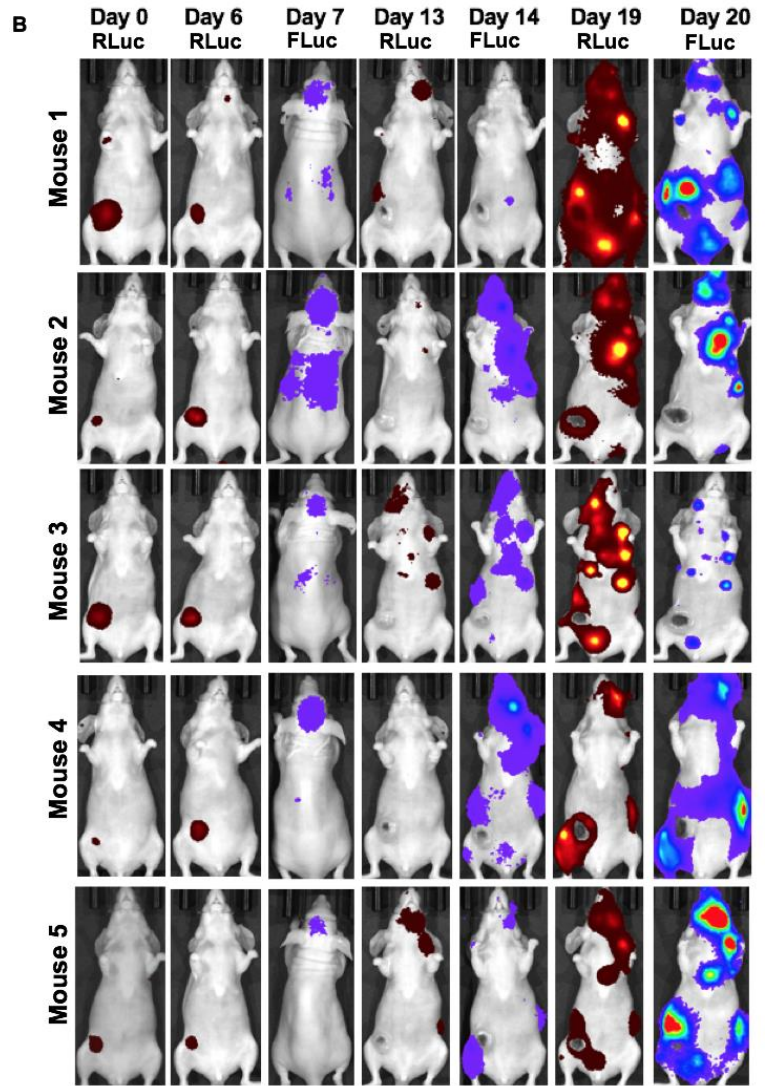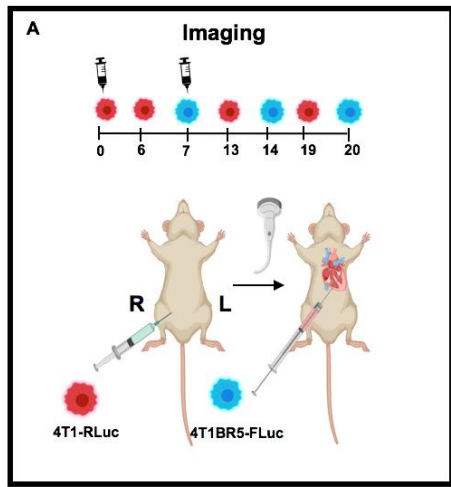
Anti-GFP (Fluc)   Anti-RLuc

140

Figure 4.5 Experimental timeline for visualizing diagnostic CTCs (n=5): RLuc BLI was performed on days 0, 6, 13 and 19 to visualize cells in the right MFP and any spontaneous metastases and FLuc BLI was performed on days 7, 14 and 20 to visualize CTCs (B). FLuc-expressing CTCs efficiently homed to RLuc-expressing primary tumours and spontaneous metastases throughout the body (C). Quantitative analysis of endpoint BLI images (day 19 and 20) revealed that the vast majority of metastases were composed of both 4T1-RLuc and 4T1BR5-FLuc cells, which was significantly higher than the number of metastases that were either 4T1-RLuc-positive only or 4T1BR5-FLuc-positive only (p< 0.001) (C/D). The presence of both 4T1-RLuc and 4T1BR5-FLuc cells in metastases was confirmed histologically (scale bars= 500 microns) (E).

4.2.5 Self-Homing "Theranostic" CTCs Efficiently Migrate into and Treat Primary Tumours and Spontaneous Metastases

Finally, we investigated whether theranostic CTCs could be systemically administered to treat primary and disseminated lesions. Again, 4T1-RLuc cells were implanted into the right MFP of nude mice and allowed 7 days of tumour growth prior to intracardiac injection of either 4T1BR5-CD cells (n=6) or 4T1BR5-FLuc cells (n=6). These mice were treated with 5'FC daily from days 10 to 20. We also included an additional cohort of mice (n=4) who received an MFP injection of 4T1-RLuc cells only and were not administered 5'FC ("4T1 Only mice" in Figure 4.6). In our first cohort (n=4), all mice had primary tumour growth similar to our data with our "diagnostic" CTCs and also developed sufficient metastases to assess therapeutic effects on metastases (Figure 4.7). In our second cohort, 12/12 mice had MFP tumours that did not develop as well as in previous cohorts at the time of secondary injection and thus, did not develop more than one or two metastases per mouse by endpoint. For these mice, we only assessed the effects of treatment on primary tumour growth (Figure 4.6). RLuc BLI was performed on days 0, 6, 13 and 19 to visualize cells in the right MFP and any spontaneous metastases and FLuc BLI was performed on days 7, 14 and 20 to visualize CTCs (Fig. 6A). As visualized by RLuc BLI, by day 6 (prior to drug administration), mice receiving 4T1BR5-CD cells had MFP RLuc signal that was not significantly different than mice receiving 4T1BR5-FLuc cells or mice receiving 4T1 cells only (Figure 4.6B, 4.6C). However, by day 19, mice receiving 4T1 cells only, had a significantly higher percent increase of RLuc signal in the MFP compared to mice that received 4T1BR5-CD cells (Figure 4.6B, 4.6D). At endpoint, primary tumours were not palpable in mice that received 4T1BR5-CD expressing cells (Figure 4.6E, 4.6F). These

data support the notion that systemically administered "theranostic" CTCs are capable of returning to and effectively treating the primary tumour. Of the 6 mice that received 4T1BR5-FLuc cells, 2 had to be sacrificed prior to endpoint due to both the size of the tumours and presence of ulceration. Overall, mice that received 4T1BR5-CD cells showed significantly improved survival compared to mice receiving 4T1BR5-FLuc cells and mice receiving 4T1 cells only ($p < 0.01$; Figure 4.6G). In the 4 mice that developed notable metastases, mice receiving 4T1BR5-CD CTCs (n=2) and 4T1BR5-FLuc CTCs (n=2) had near equivalent FLuc signal on the day of CTC injection, but by day 14, mice receiving 4T1BR5-CD CTCs had visibly less FLuc signal (Figure 4.7B, 4.7C). Both mice that received 4T1BR5-FLuc cells had to be sacrificed prior to endpoint due to both the size of primary tumours and presence of ulceration, and thus, FLuc imaging on days 20 and 29 was only performed on mice that received 4T1BR5-CD cells. Importantly, mice in each cohort had similar RLuc signal on days 0 and 6 prior to CTC administration (Figure 4.7D, 4.7E), but by day 19, the single mouse that received 4T1BR5-FLuc cells and survived until day 19, had visibly more RLuc metastases than both mice that received 4T1BR5-CD cells (Figure 4.7D, 4.7E).
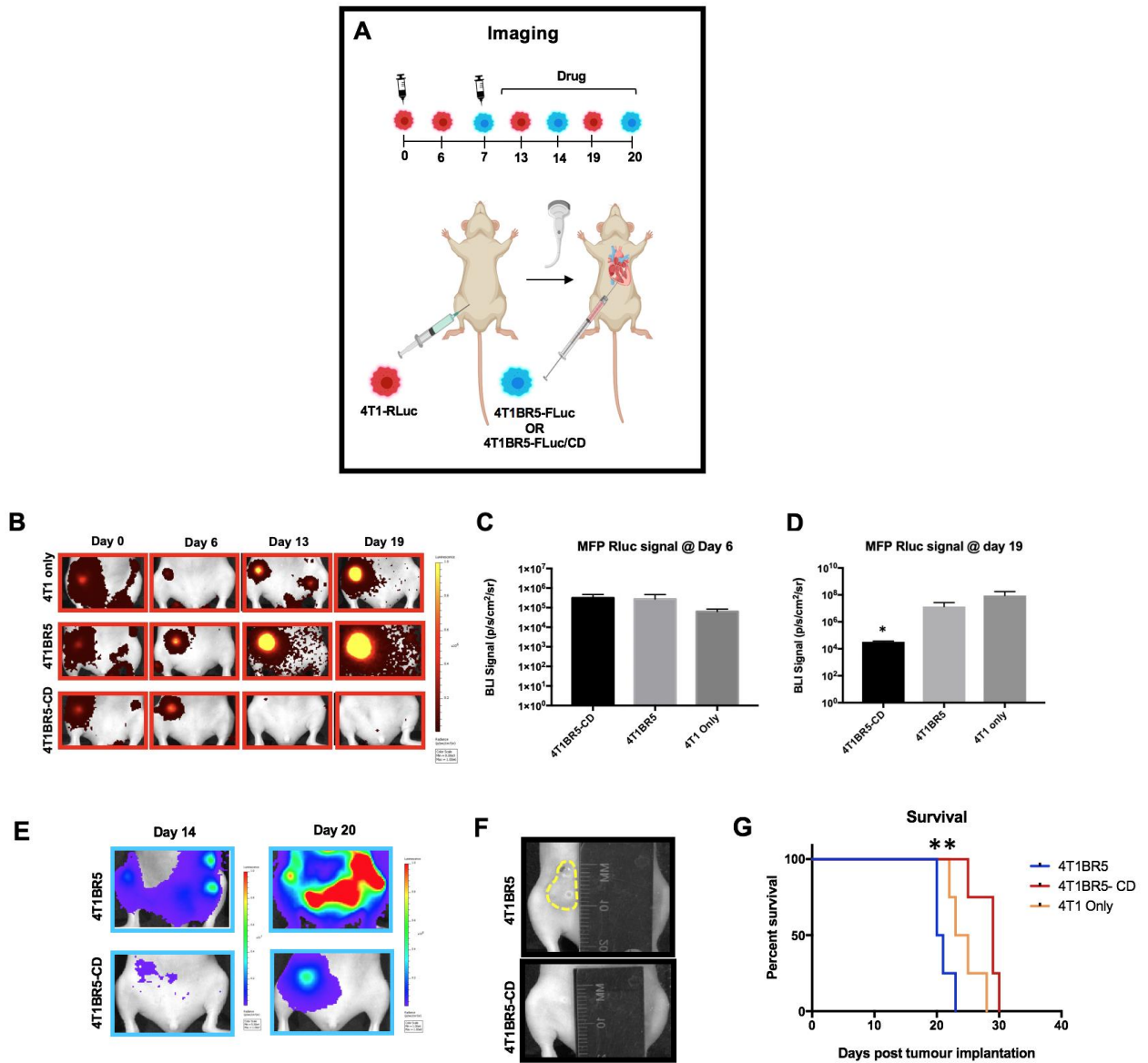
Figure 4.6 Experimental timeline for visualizing self-homing theranostic CTCs (n=16): 4T1BR5-CD and 4T1BR5 mice were treated with 5'FC daily from days 10 to 20. RLuc BLI was performed on days 0, 6, 13 and 19 to visualize cells in the right MFP and FLuc BLI was performed on days 7, 14 and 20 to visualize CTCs (B/E). By day 6 (prior to drug administration), mice receiving 4T1BR5-CD cells had MFP RLuc signal that was not significantly different than mice receiving 4T1BR5 cells or 4T1 cells only (C). However, by day 19, mice receiving only 4T1-RLuc cells had a significantly higher percent increase of RLuc signal in the MFP compared to mice that received 4T1BR5-CD cells (D). At endpoint, primary tumours were not palpable in mice that received 4T1BR5-CD cells (F). These data support the notion that systemically administered "theranostic" CTCs are capable of returning to and

effectively treating the primary tumour (E). Mice that received 4T1BR5-CD cells showed significantly improved survival compared to mice receiving 4T1BR5 cells and mice receiving 4T1 cells only (G).
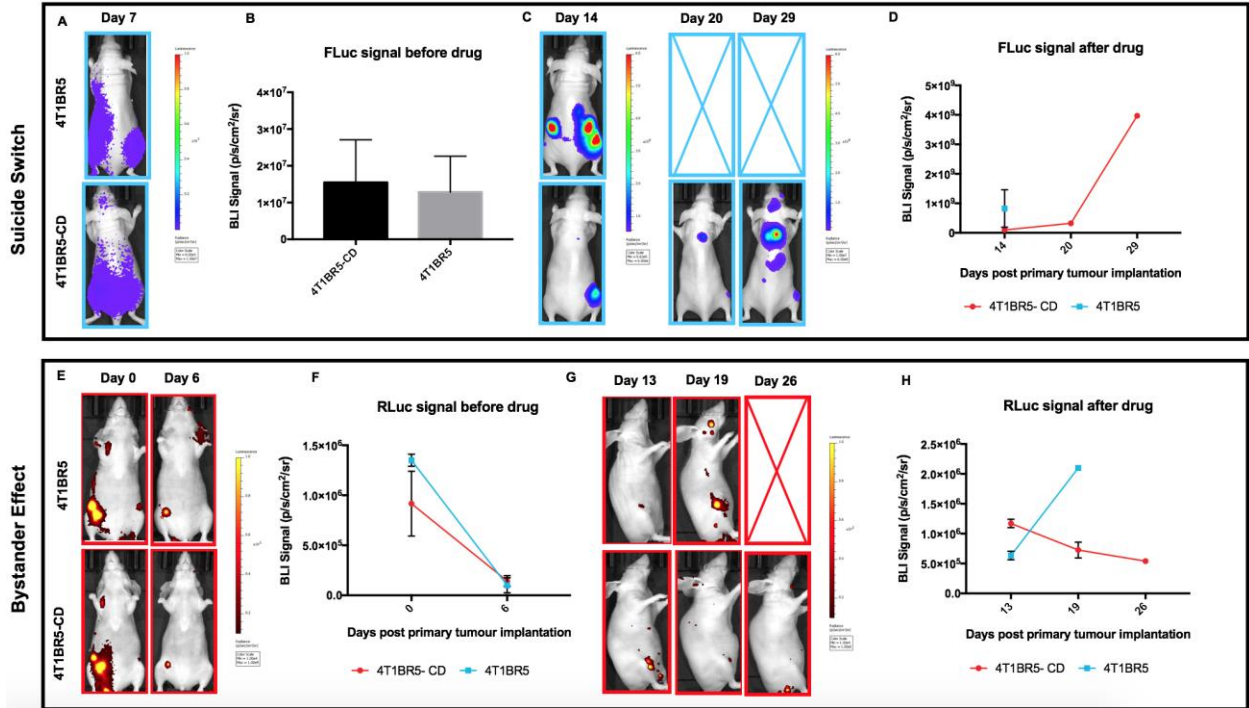
Figure 4.7 Treating metastases: On the day of intracardiac injection (day 7), mice receiving 4T1BR5-CD CTCs (n=2) and 4T1BR5 CTCs (n=2) had near equivalent FLuc signal (A/B), but by day 14, mice receiving 4T1BR5-CD CTCs had visibly less FLuc signal (C/D). Both mice that received 4T1BR5 cells had to be sacrificed prior to endpoint due to both the size of primary tumours and presence of ulceration, and thus, FLuc imaging on days 20 and 29 was only performed on mice that received 4T1BR5-CD cells. Importantly, mice in each cohort had similar RLuc signal on days 0 and 6 prior to CTC administration (E/F), but by day 19, the single mouse that received 4T1BR5 cells and survived until day 19, had visibly more RLuc metastases than both mice that received 4T1BR5-CD cells (G/H).

4.3 Discussion

This study demonstrates that engineered "self-homing" CTCs co-expressing an imaging reporter and a therapeutic transgene can be used as a novel theranostic cellular vector to visualize and treat both primary tumours and disseminated spontaneous breast cancer metastases in mice. We first show using dual-luciferase BLI the remarkable ability of systemically-administered CTCs to preferentially home to pre-established spontaneous metastases in various organs throughout the body with minimal formation of new tumours. Leveraging on this highly preferential homing capability, we then show that CTCs co-expressing the prodrug converting fusion enzyme system CD:UPRT, to kill neighboring cells via the bystander effect as well as act as a suicide switch, was able to decrease tumour burden and extend survival.

Cancer, particularly in patients with metastatic disease, remains a leading cause of death in the world [38, 39]. Treatments that often work on localized disease are often not an option or fail in the patients with significant metastatic spread. Thus, the development of technologies for earlier detection and treatment of metastatic disease remains at the forefront of cancer research. Therapeutics that have natural tumour tropism or are designed to target lesions offer potential benefits of improved therapeutic effectiveness due to high intratumoural concentration of therapeutic payloads, as well as increased safety due to minimization of off-target cytotoxicity in normal tissues [4-19, 27-32]. The incorporation of imaging probes (e.g., radiolabels, iron oxides, etc.) into these targeted agents has been used to allow one to track their whole-body biodistribution to on-tumour and off-tumour sites [28-30, 32]. An agent that is very effective at naturally localizing to metastases with

147

little off-target accumulation could theoretically also be used as an effective agent for the early diagnosis and treatment of metastatic disease.

In recent years, numerous classes of tumour-targeting agents have been developed including small molecules [40], antibodies [41-43], nanoparticles [44, 45], viral [46-48] and non-viral gene vectors [49-51], and cell-based vectors [4-19, 27-32]. Traditionally, the development of cell-based therapies has focused on the use of stem-cells including tissue-specific stem cells, pluripotent stem cells or mesenchymal stem cells [5,6,8-14]. These approaches offer many important benefits including their innate homing capabilities and natural anti-tumour effects; however, they suffer from limited passaging in culture resulting in roadblocks throughout the engineering process as well as limited therapeutic potential *in vivo*. Similarly, others have used immune cell-based vectors in efforts to target and treat a variety of tumours including tumour-infiltrating lymphocytes (TILs) [52, 53] and cytokine induced killer (CIK) cells [54, 55]. CIK cells are a group of immune effector cells with a mixed T- and natural killer (NK) cell phenotype. Thorne and colleagues successfully showed this effector cell population could be loaded with an oncolytic virus for targeted delivery and treatment of murine tumours [55]. Currently, one of the most employed cell-based tumour-targeting strategies is the engineering of T lymphocytes with chimeric antigen receptors (CARs) in efforts to selectively recognize and kill cancer cells expressing the B cell antigen CD19, while sparing healthy tissue [15-18]. This strategy has shown tremendous promise in the clinic in upwards of 70% of patients with otherwise treatment-refractory B cell leukemia and other B cell malignancies such as diffuse large B-cell lymphoma. However, in some cases, CAR-T cell therapy has shown no effect at all,

and in many cases, patients experience potentially lethal side effects as a result of CAR-T cells not proliferating and persisting in the body over time, proliferating and activating excessively, or nonspecific homing to healthy organs [19, 56]. CAR-T cells have also shown minimal therapeutic effectiveness for solid tumours due to less than ideal homing capacity. Thus, there remains a need for novel cell-based delivery vehicles that are capable of homing to solid tumours.

In 2009, Kim and colleagues demonstrated the ability of cancer cells from an established lesion to enter the circulation and then return to this lesion to continue to survive and proliferate, a process they termed "self-seeding" [25]. The self-seeding capabilities of cancer cells was attributed to both the recruitment potential of the established tumour microenvironment as well as the seeding capabilities of cancer cells themselves. As a result, several groups have attempted to repurpose the self-homing properties of cancer cells to use them as "self-targeted" cell-based delivery vehicles for anti-cancer therapeutics [27-32]. In comparison to previously discussed cell-based vectors (i.e., stem cells and immune cells), cancer cells can be continuously grown *in vitro* enabling extensive cell engineering, may have superior homing capability to lesions, and may have prolonged survival and expansion once in tumours. Past studies have included using cancer cells as a vehicle to deliver oncolytic viruses [27, 28], engineering cancer cells to express suicide genes [29, 30] or apoptosis-inducing ligands [32] to transfer death signals to neighboring non-engineered tumour cells, and engineering cancer cells to express therapeutic agents that influence the tumour microenvironment [31], specifically angiogenesis. In this work, we exploit the innate self-homing properties of CTCs to investigate their potential as an

efficient diagnostic probe and drug delivery vehicle for self-targeted therapy of primary and metastatic tumours. In our model, the primary tumour had a week to grow and spontaneously metastasize prior to the injection of experimental CTCs and thus, we assume it is the experimental CTCs homing to those pre-established sites and not the alternative. Our imaging data from early time points supports this theory such that some animals displayed spontaneous metastases prior to the injection of CTCs. Furthermore, our transwell migration assay data shows that conditioned media from our primary 4T1 cells, causes increased migration compared to media from our experimental CTC 4T1BR5 cell line. Previous work using the MDA-MB-231 breast cancer model showed that the cytokines IL-6 and IL-8 produced by the primary tumour acted as chemoattractants to efficiently recruit CTCs[25]. Future work will look to investigate whether the production of these cytokines is enhanced in 4T1 conditioned media and whether they may contribute to the self-homing efficiency seen in this model.

Based on our initial imaging results, we engineered our experimental CTCs to express a suicide gene and used noninvasive imaging to monitor the effects of self-targeted therapy in contralateral, intratumoural, and metastatic models. In a prodrug converting enzyme suicide gene therapy system, cancer cells are transfected with a gene that can express an enzyme with the ability to convert a nontoxic prodrug into an active chemotherapeutic [37]. By incorporating a suicide switch, we can visualize the killing of engineered therapeutic cancer cells as well as a bystander effect whereby adjacent non-engineered cancer cells are killed. While there are numerous enzyme/prodrug systems available, we chose to use the CD:UPRT fusion gene, due to the ability of 5'FU (the active form) to interrogate

150

neighbouring cells independently of gap junctions, as well as readily diffuse the blood brain barrier [34-36]. As a result, the CD/5'FC system has shown to have a more potent bystander effect than the commonly used HSV-TK/GCV system [57-60]. Furthermore, in comparison to the traditional CD/5'FC system, we used the CD:UPRT fusion gene, as UPRT can further convert 5'FU into 5'FUMP, which has shown to have significantly enhanced cancer killing efficiency in prostate, ovarian and breast cancer subtypes [61, 62]. In the current study, we were able to visualize therapeutic CTCs that had successfully migrated from the original to the contralateral MFP but did not observe a significant therapeutic effect. However, we did observe a decrease in tumour burden when our therapeutic cells were administered intratumourally (3×10^5 cells). These findings suggest the ratio of therapeutic cells to cancer cells may be crucial in generating a significant therapeutic effect *in vivo*. By using dual BLI, we also show effective homing and treatment of primary tumours when therapeutic CTCs were administered systemically and as a result, demonstrate extended survival in mice treated with 5'FC. Our preliminary data suggests systemically administered CTCs may also be capable of homing to and treating disseminated breast cancer metastases. Future work will look to validate these findings in additional mouse cohorts.

While our findings suggest CTCs have potential as highly-efficient carriers of therapeutic cargo to primary and metastatic tumour sites, our approach has some limitations to consider. Most importantly, while CD:UPRT expression was able to kill off many of the engineered 4T1BR5 cells, some of these cells were capable of avoiding cell death and generated new tumours. Additionally, while we demonstrate the ability to kill off

neighbouring non-engineered cancer cells through a bystander effect, some mice show residual spontaneous metastases following treatment. Future work will explore incorporating more than one therapeutic gene into the engineered cells. For example, a CD/HSV-TK system, would allow the administration of two different pro-drugs, creating a higher likelihood of targeting and treating engineered CTCs while possibly also enhancing the bystander effect. Additionally, timing of CTC self-homing to pre-established tumours should be further explored. Our data suggests that three days may not be the optimal window for systemically administered CTCs to efficiently home to established metastases. If we administer the pro-drug too early, we may lose some of our therapeutic CTCs to self-induced toxicity prior to receiving any therapeutic effects on neighbouring non-engineered cancer cells. Furthermore, a larger window would allow time for therapeutic cells to proliferate and expand the therapeutic population once they have reached their tumour target.

In conclusion, our work provides evidence that CTCs are a novel theranostic vector platform for the visualization and treatment of pre-established tumour sites throughout the body. Overall, while further refinement is needed, this unorthodox strategy may have tremendous long term translational potential as a highly effective theranostic platform, specifically in patient populations presenting with metastatic disease at initial diagnosis, and those at high risk of cancer recurrence or metastatic relapse.

4.4 Materials and methods

4.4.1 Cell Engineering

The 4T1BR5 cells were a kind gift from Dr. Patricia Steeg's lab and engineered to stably co-express red-shifted *Luciola italica* luciferase (FLuc) and green fluorescent protein (GFP) using a commercial lentiviral vector (RediFect Red-FLuc-GFP; PerkinElmer, USA). Cells were transduced and FACS sorted based on GFP expression using a FACSAria III flow cytometric cell sorter (BD Biosciences). The parental 4T1 cells were also received from Dr. Patricia Steeg's lab and engineered to stably co-express *Renilla* luciferase-8 (RLuc) and ZsGreen (ZsG) using a virus made in house. Cells were transduced and sorted based on ZsG expression using FACS. The resultant 4T1BR5-FLuc/GFP (4T1BR5-Fluc) and 4T1-RLuc/ZsG (4T1-Rluc) cells were maintained in DMEM containing 10% FBS and 1% antibiotics, at 37°C and 5% CO_2. The 4T1BR5-FLuc and 4T1-RLuc cells were then engineered a second time to stably express cytosine deaminase-uracil phosphoribosyl transferase (CD-UPRT) and tdTomato (tdT). Both cell lines were transduced and FACS sorted based on tdT expression. Cells were washed three times with Hanks balanced salt solution (HBSS) and collected for *in vitro* evaluation or injection into animals.

4.4.2 In Vitro Studies

Cell line characterization

All *in vitro* results are from three independent experiments with three replicates of each condition. To evaluate the relationship between cell number and BLI signal, 1×10^4, 5×10^4, 1×10^5, 1.5×10^5, and 5×10^5 4T1BR5-FLuc or 4T1-RLuc cells were seeded in each well of

24-well plates. We acquired fluorescent images of each plate. We then added 10 μL of D-luciferin (30 mg/mL; Syd Labs, Inc., MA, USA) or 10 μL of h-Coelenterazine (150μg/mL; NanoLight Technology, Prolume, AZ, USA) to the growth medium in each well and BLI images were collected for up to 35 minutes. All images were acquired using a hybrid optical/X-ray scanner (IVIS Lumina XRMS In Vivo Imaging System, PerkinElmer). Signal was measured with region-of-interest (ROI) analysis using LivingImage Software (Perkin Elmer). An ROI was drawn around each well to measure the radiant efficiency $(p/s/cm^2/sr/uW/cm^2)$ for fluorescence images and average radiance $(p/s/mm^2/sr)$ for bioluminescence images. The mean signal across replicates was determined for each independent experiment.

Cross reactivity

To assess *in vitro* cross reactivity, we seeded two identical 24-well plates with 1×10^5 4T1-RLuc, 4T1BR5-Fluc, 4T1 naïve cells, and equivalent volume of media. We added 10uL of d-Luciferin to each well in plate 1 and 10uL of h-Coelenterazine to each well in plate 2. Images were acquired for up to 35 minutes and an ROI was drawn around each well to measure the average radiance $(p/s/mm^2/sr)$. The mean signal across replicates was determined for each independent experiment.

Transwell Migration Assay

A FluoroBlok™ Multiwell Insert System was used with an 8um porous polyethylene terephthalate membrane (Corning, Corning NY, USA). We seeded 5×10^4 cells (4T1-RLuc or 4T1BR5-Fluc) in 75cm^2 flasks. At 48 hours post seeding, 650uL of new or conditioned

DMEM was collected and used for the bottom chamber of the transwell plate. We then seeded 2.5×10^4 cells (4T1-RLuc or 4T1BR5-Fluc) in the upper chamber of the transwell insert in 100ul of new DMEM. After 24 hours, the membranes were fixed in ethanol for 5 minutes, washed with PBS, and stained with Hoechst 33342 (10ug/ml in water) for 5 minutes. Membranes were cut out with a scalpel and mounted in 90% glycerol onto slides. Three random images were taken of the lower side of each membrane using an Invitrogen EVOS FL Auto Cell Imaging System and the mean fluorescence signal was calculated.

CD:UPRT Functionality Testing

To assess the functionality of the CD-UPRT gene *in vitro*, Vybrant MTT assays were used. 2×10^4 4T1-RLuc or 4T1-CD cells were seeded in each well of 96-well plates and incubated in either the desired concentration of 5'FC (diluted in DMEM) or incubated in DMEM alone. Ten microliters of MTT solution was added to each well and absorbance at 450nm was measured using a microplate spectrophotometer (Fluoroskan Ascent FL, ThermoLabSystems) at 24, 48, 72 and 96 hours. This experiment was repeated for 4T1BR5-FLuc and 4T1BR5-FLuc/CD cells.

4.4.3 In Vivo Studies

Animals were cared for in accordance with the standards of the Canadian Council on Animal Care, and under an approved protocol of the University of Western Ontario's Council on Animal Care (2015-0558). Six to eight-week-old female nu/nu mice were obtained from Charles River Laboratories (Willington, MA, USA).

Contralateral tumour model

Mice received a lower right mammary fat pad (MFP) injection of 300,000 4T1-Rluc or 4T1-CD cells and a lower left MFP injection of 300,000 4T1BR5-Fluc cells on day 0 (Figure 4.1A; n=5). RLuc BLI was performed on days 0 and 7 and FLuc BLI performed on days 1 and 8. Additional BLI was performed for experiments with CD expressing cells on days 15 (RLuc) and 16 (FLuc). For experiments with CD expressing cells, mice receiving 4T1-Rluc and 4T1-CD cells both received intraperitoneal injections of 5'FC (250mg/kg/day) on days 7 to 14 (Figure 4.3A; n=8).

Intratumoural model

Mice received a lower right mammary fat pad (MFP) injection of 300,000 4T1BR5-Fluc cells on day 0 and an intratumoural injection of 300,000 4T1-Rluc or 4T1-CD cells on day 7 (Figure 4.4A; n=8). FLuc BLI was performed on days 0, 4, 8 and 16 and RLuc BLI performed on days 7 and 15. Mice receiving 4T1BR5-Fluc and 4T1BR5-CD cells both received intraperitoneal injections of 5'FC (250mg/kg/day) on days 8 to 16.

Metastatic tumour model

Mice received a lower right MFP injection of 300,000 4T1-Rluc cells. MFP tumours grew for seven days prior to all mice receiving an intracardiac injection of 2×10^4 4T1BR5-FLuc or 4T1BR5-CD cells in 0.1mL of HBSS (Figure 4.5A; n=5). Injections were performed under image guidance using a Vevo 2100 ultrasound system (VisualSonics Inc.). RLuc BLI was performed on days 0, 6, 13 and 19. FLuc BLI was performed on days 7, 14 and 20. For experiments with CD expressing cells, mice receiving 4T1BR5-FLuc and 4T1BR5-

CD cells both received intraperitoneal injections of 5'FC (250mg/kg/day) on days 10 to 20 (Figure 4.6A; n=12).

BLI Procedure

BLI was performed using a hybrid optical/X-ray scanner (IVIS Lumina XRMS In Vivo Imaging System, PerkinElmer). Mice were anesthetized with isofluorane (2% in 100% oxygen) using a nose cone attached to an activated carbon charcoal filter for passive scavenging. For RLuc BLI, anesthetized mice received a 20 μL intravenous injection of h-Coelenterazine (150μg/mL) and BLI images were captured for up to 30 minutes. For FLuc BLI, anesthetized mice received a 100 μL intraperitoneal injection of d-Luciferin (30 mg/mL) and BLI images were captured for up to 35 minutes.

Image Analysis

BLI signal was measured with region-of-interest (ROI) analysis using LivingImage Software (Perkin Elmer). ROIs were drawn throughout the mouse body of RLuc and FLuc image sets for each mouse.

Histology

At endpoint, mice were sacrificed by isoflurane overdose and perfused with 4% paraformaldehyde via the left ventricle. Tissues were removed and cryopreserved in ascending concentrations of sucrose (10, 20, and 30% w/v) for 24 hours each, then immersed in optimal cutting temperature (OCT) compound, and frozen using liquid nitrogen. Contiguous 10-μm frozen sections were collected and select sections were stained

with hematoxylin and eosin (H&E), DAPI, Anti-GFP, Anti-Rluc. Stained sections were imaged using an Invitrogen EVOS FL Auto Cell Imaging System.

Statistics

All statistics were calculated using GraphPad Prism 7 Software. Data were expressed as mean ± SEM for *in vitro* and *in vivo* studies and analyzed by Student's t test when comparing two groups. Survival times of mouse groups were analyzed using a log-rank test. Differences were considered statistically significant at $*p < 0.05$, $**p < 0.01$, $***p < 0.001$, and $****p < 0.0001$.

4.5 References

1. DeVita, VT. Jr., Eggermont, AMM., Hellman, S., Kerr, DJ. Clinical cancer research: The past, present and the future. Nat. Rev. Clin. Oncol. 11, 663–669 (2014).

2. Kalinich, M., & Haber, D. A. (2018). Cancer detection: Seeking signals in blood. *Science*, *359*(6378), 866-867.Haber, DA., Gray, NS., Baselga, J. *Cell*145,19 (2011).

3. Fliervoet, LA., Mastrobattista, E. Drug delivery with living cells. Adv. Drug Deliv. Rev. 106, 63–72 (2016).

4. Squillaro, T., Peluso, G., Galderisi, U. Clinical trials with mesenchymal stem cells: An update. Cell Transplant. 25, 829–848 (2016).

5. Stuckey, DW., Shah, K. Stem cell-based therapies for cancer treatment: Separating hope from hype. Nat. Rev. Cancer 14, 683–691 (2014).

6. Tsai, AK., Davila, E. Producer T cells: Using genetically engineered T cells as vehicles to generate and deliver therapeutics to tumors. Oncoimmunology 5, e1122158 (2016).

7. Mimeault, M., Hauke, R., Batra, SK. Stem cells: A revolution in therapeutics— Recent advances in stem cell biology and their therapeutic applications in regenerative medicine and cancer therapies. Clin. Pharmacol. Ther. 82, 252–264 (2007).

8. Ankrum, J., Karp, JM. Mesenchymal stem cell therapy: two steps forward, one step back, Trends Mol. Med. 16; 203–209. (2010).

9. Aboody, K., et al., Neural stem cells display extensive tropism for pathology in adult brain: evidence from intracranial gliomas, Proc. Natl. Acad. Sci. U. S. A. 97 ;12846–12851. (2001).

10. Park, KI., et al., Neural stem cells may be uniquely suited for combined gene therapy and cell replacement: evidence from engraftment of Neurotrophin-3-expressing stem cells in hypoxic–ischemic brain injury, Exp. Neurol. 199; 179–190. (2006).

11. Alieva, M., et al., Glioblastoma therapy with cytotoxic mesenchymal stromal cells optimized by bioluminescence imaging of tumor and therapeutic cell response, PLoS One 7; 1–11. (2012).

12. Bagó, JR., Sheets, KT., Hingtgen, SD. Neural stem cell therapy for cancer, Methods. 99; 37–43. (2016).

13. Song, K., Benhaga, N., Anderson, RL., Khosravi-Far, R. Transduction of tumor necrosis factor-related apoptosis-inducing ligand into hematopoietic cells leads to inhibi- tion of syngeneic tumor growth in vivo, Cancer Res. 66; 6304–6311. (2006).

14. Maude, S. L., Frey, N., Shaw, P. A., Aplenc, R., Barrett, D. M., Bunin, N. J., ... & Mahnke, Y. D. Chimeric antigen receptor T cells for sustained remissions in leukemia. *New England Journal of Medicine*, *371*(16), 1507-1517. (2014).

15. Porter, D. L., Kalos, M., Zheng, Z., Levine, B., & June, C. Chimeric antigen receptor therapy for B-cell malignancies. *Journal of Cancer*, *2*, 331. (2011).

16. Grupp, S. A., Kalos, M., Barrett, D., Aplenc, R., Porter, D. L., Rheingold, S. R., & Milone, M. C. Chimeric antigen receptor–modified T cells for acute lymphoid leukemia. *New England Journal of Medicine*, *368*(16), 1509-1518. (2013).

17. Davila, M. L., Bouhassira, D. C., Park, J. H., Curran, K. J., Smith, E. L., Pegram, H. J., & Brentjens, R. Chimeric antigen receptors for the adoptive T cell therapy of hematologic malignancies. *International journal of hematology*, *99*(4), 361-371. (2014).

18. June, C. H., O'Connor, R. S., Kawalekar, O. U., Ghassemi, S., & Milone, M. C. CAR T cell immunotherapy for human cancer. *Science*, *359*(6382), 1361-1365. (2018).

19. Paget, S. Distribution of secondary growths in cancer of the breast. *Lancet, I*, *571*.1989. (1989).

20. Chambers, A F., Groom, A C., and MacDonald, I C. Dissemination and growth of cancer cells in metastatic sites Nat. Rev. Cancer 2 563–72. (2002).

21. Weiss, L. Metastatic inefficiency *Adv. Cancer Res.* 54 159–211. (1990).

22. Tarin, D., Price, J E., Kettlewell, M G., Souter, R G., Vass, A C., and Crossley, B. Clinicopathological observations on metastasis in man studied in patients treated with peritoneovenous shunts *Br. Med. J. (Clin. Res. Ed.)* 288 749–51. (1984).

23. Nguyen, DX., Bos, PD., Massague, J. Metastasis: from dissemination to organ-specific colonization. Nat Rev Cancer. 9:274–284. (2009).

24. Norton, L., Massague, J. Is cancer a disease of self-seeding? Nat Med. 12:875–878. (2006).

25. Carmeliet, P., Jain, RK. Angiogenesis in cancer and other diseases. Nature. 407:249–257. (2000).

26. Raykov, Z., Balboni, G., Aprahamian, M., Rommelaere, J. Carrier cell-mediated delivery of oncolytic parvoviruses for targeting metastases. Int. J. Cancer 109, 742–749 (2004).

27. Power, AT., Wang, J., Falls, TJ., Paterson, JM., Parato, KA., Lichty, BD., Stojdl, DF. Forsyth, PA., Atkins, H., Bell, JC. Carrier cell-based delivery of an oncolytic virus circumvents antiviral immunity. Mol. Ther. 15, 123–130 (2007).

28. Freeman, SM., Abboud, CN., Whartenby, KA., Packman, CH., Koeplin, DS., Moolten, FL., Abraham, GN. The "bystander effect": Tumor regression when a fraction of the tumor mass is genetically modified. Cancer Res. 53, 5274–5283 (1993).

29. Garcia-Castro, J., Mart.nez-Palacio, J., Lillo, R., Garc.a-S.nchez, F., Alemany, R., Madero, L., Bueren, JA., Ramrez, M.Tumor cells as cellular vehicles to deliver gene therapies to metastatic tumors. Cancer Gene Ther. 12, 341–349 (2005).

30. Dondossola, E., Dobroff, AS., Marchi, S., Card.-Vila, M., Hosoya, H., Libutti, SK., Corti, A., Sidman, RL., Arap, W., Pasqualini, R. Self-targeting of TNF-releasing cancer cells in preclinical models of primary and metastatic tumors. Proc. Natl. Acad. Sci. U.S.A. 113, 2223–2228 (2016).

31. Reinshagen, C., Bhere, D., Choi, S.H., Hutten, S., Nesterenko, I., Wakimoto, H., Le Roux, E., Rizvi, A., Du, W., Minicucci, C. and Shah, K. CRISPR-enhanced

engineering of therapy-sensitive cancer cells for self-targeting of primary and metastatic tumors. *Science translational medicine*, *10*(449), p.eaao3240. (2018).

32. Parkins, KM., Hamilton, AM., Dubois, VP., Wong, SM., Foster, PJ., and Ronald, JA. "Cellular MRI Reveals Altered Brain Arrest of Genetically Engineered Metastatic Breast Cancer Cells," Contrast Media & Molecular Imaging, vol. 2019, Article ID 6501231, (2019).

33. Kanai, F., Lan, K. H., Shiratori, Y., Tanaka, T., Ohashi, M., Okudaria, T & Tamaoki, T. In vivo gene therapy for α-fetoprotein-producing hepatocellular carcinoma by adenovirus-mediated transfer of cytosine deaminase gene. *Cancer research*, *57*(3), 461-465. (1997).

34. Ichikawa, T., Tamiya, T., Adachi, Y., Ono, Y., Matsumoto, K., Furuta, T., ... & Ohmoto, T. In vivo efficacy and toxicity of 5-fluorocytosine/cytosine deaminase gene therapy for malignant gliomas mediated by adenovirus. *Cancer gene therapy*, *7*(1), 74. (2000).

35. Chai, L. P., Wang, Z. F., Liang, W. Y., Chen, L., Chen, D., Wang, A. X., & Zhang, Z. Q. In vitro and in vivo effect of 5-FC combined gene therapy with TNF-α and CD suicide gene on human laryngeal carcinoma cell line Hep-2. *PLoS One*, *8*(4), e61136. (2013).

36. Altaner, C. Prodrug cancer gene therapy. *Cancer letters*, *270*(2), 191-201. (2008).

37. American Cancer Society, Cancer Facts & Figures 2014 (American Cancer Society). (2014).

38. Bray, F., Ferlay, J., Soerjomataram, I., Siegel, R. L., Torre, L. A., & Jemal, A. Global cancer statistics 2018: GLOBOCAN estimates of incidence and mortality

worldwide for 36 cancers in 185 countries. *CA: a cancer journal for clinicians*, *68*(6), 394-424. (2018).

39. Hwang, J. Y., Li, Z., & Loh, X. J. Small molecule therapeutic-loaded liposomes as therapeutic carriers: from development to clinical applications. *RSC Advances*, *6*(74), 70592-70615. (2016).

40. Patel, J., Amrutiya, J., Bhatt, P., Javia, A., Jain, M., & Misra, A. Targeted delivery of monoclonal antibody conjugated docetaxel loaded PLGA nanoparticles into EGFR overexpressed lung tumour cells. *Journal of microencapsulation*, *35*(2), 204-217. (2018).

41. Weiner, L.M. et al. New approaches to antibody therapy. Oncogene. V.19., p.6144, (2000).

42. Weiner, L.M. et al. Monoclonal antibodies: versatile platforms for cancer immunotherapy. Nat. Rev. Immunol., v.10, p.317. (2010).

43. Vrignaud, S., Benoit, J. P., & Saulnier, P. Strategies for the nanoencapsulation of hydrophilic molecules in polymer-based nanoparticles. *Biomaterials*, *32*(33), 8593-8604. (2011).

44. Vasir, J. K., & Labhasetwar, V. Biodegradable nanoparticles for cytosolic delivery of therapeutics. *Advanced drug delivery reviews*, *59*(8), 718-728. (2007).

45. Lu, Y., Madu, CO. Viral-based gene delivery and regulated gene expression for targeted cancer therapy. Expert Opin Drug Deliv. 7:19-35. (2010).

46. Kohn, DB., Sadelain, M., Glorioso, JC. Occurrence of leukaemia following gene therapy of X-linked SCID. Nat Rev Cancer. ;3:477-88. (2003).

47. Marshall, E. Gene therapy death prompts review of adenovirus vector. Science. 286:2244-5. (1999).

48. Kaneda, Y., Tabata, Y. Non-viral vectors for cancer therapy. Cancer Sci. 97:348-54. (2006).

49. Morille, M., Passirani, C., Vonalbourg, A. Progress in developing cationic vectors for non-viral systemic gene therapy against cancer. Biomaterials. 29:3477-96

50. Al-Dosari, MS., Gao, X. Nonviral gene delivery: principle, limitations, and recent progress. AAPS J 2009;11:671-81. (2008).

51. Rosenberg, SA., Yannelli, JR., Yang, JC., Topalian, SL., Schwartzentruber, DJ., Weber, JS., Parkinson, DR., Seipp, CA., Einhorn, JH., White, DE. Treatment of patients with metastatic melanoma with autologous tumor-infiltrating lymphocytes and interleukin 2. *J Natl Cancer Inst* **86**: 1159–1166. (1994).

52. Dudley, ME., Wunderlich, JR., Robbins, PF., Yang, JC., Hwu, P., Schwartzentruber, DJ., Topalian, SL., Sherry, R., Restifo, NP., Hubicki, AM., Robinson, MR., Raffeld, M., Duray, P., Seipp, CA., Rogers-Freezer, L., Morton, KE., Mavroukakis, SA., White, DE., Rosenberg, SA. Cancer regression and autoimmunity in patients after clonal repopulation with antitumor lymphocytes. *Science* **298**: 850–854. (2002).

53. Edinger, M., Cao, Y. A., Verneris, M. R., Bachmann, M. H., Contag, C. H., & Negrin, R. S. Revealing lymphoma growth and the efficacy of immune cell therapies using in vivo bioluminescence imaging. *Blood*, *101*(2), 640-648. (2003).

54. Thorne, S. H., Negrin, R. S., & Contag, C. H. Synergistic antitumor effects of immune cell-viral biotherapy. *Science*, *311*(5768), 1780-1784. (2006).

55. Labanieh, L., Majzner, R. G., & Mackall, C. L. Programming CAR-T cells to kill cancer. *Nature biomedical engineering*, *2*(6), 377. (2018).

56. Fischer, U., Steffens, S., Frank, S., Rainov, NG., Schulze-Osthoff, K., Kramm, CM. Mechanisms of thymidine kinase/ganciclovir and cytosine deaminase/5-fluorocytosine suicide gene therapy-induced cell death in glioma cells. Oncogene. 24(7):1231–43. (2005).

57. Kerr, IG., Zimm, S., Collins, JM., O'Neill, D., Poplack, DG. Effect of intravenous dose and schedule on cerebrospinal fluid pharmacokinetics of 5-fluorouracil in the monkey. Cancer Res. 44:4929–32. (1984).

58. Shirakawa, T., Gardner, TA., Ko, S-C., Bander, N., Woo, S., Gotoh, A., et al. Cytotoxicity of adenoviral-mediated cytosine deaminase plus 5-fluorocytosine gene therapy is superior to thymidine kinase plus acyclovir in a human renal cell carcinoma model. J Urol. 162(3 Pt 1):949–54. (1999).

59. Trinh, QT., Austin, EA., Murray, DM., Knick, VC., E, HB. Enzyme/prodrug gene therapy: comparison of cytosine deaminase/5-fluorocytosine versus thymidine kinase/ganciclovir enzyme/prodrug systems in a human colorectal carcinoma cell line. Cancer Res. 55(21):4808–12. (1995).

60. Miyagi, T., Koshida, K., Hori, O., Konaka, H., Katoh, H., Kitagawa, Y., et al. Gene therapy for prostate cancer using the cytosine deaminase/uracil phosphoribosyltransferase suicide system. J Gene Med. 5(1):30–7. (2003).

61. Richard, C., Duivenvoorden, W., Bourbeau, D., Massie, B., Roa, W., Yau, J. et al. Sensitivity of 5-fluorouracil-resistant cancer cells to adenovirus suicide gene therapy. Cancer Gene Ther. 14(1):57–65. (2006).

Chapter 5

5 Summary and Future Work

In this thesis, we present the first study to use both iron-based cellular MRI and BLI to longitudinally track cancer metastasis *in vivo*. Further, we present the first application of this imaging model to study concomitant tumour enhancement in an immune competent mouse model of breast cancer metastasis. This is the first application of dual-luciferase BLI to monitor the long-term fate of two different cancer populations in the same animal and the first study to use molecular-genetic imaging to visualize whole body tumour self-homing and effective self-targeted treatment of disseminated metastases.

5.1 Discussion and Conclusions

Tumour self-homing and CTR/CTE are potential mechanisms contributing to cancer metastasis whereby an existing primary tumour can influence the growth of secondary tumours at distant sites. The majority of studies have relied on endpoint histology to study these mechanisms. This thesis employed numerous imaging technologies to noninvasively

study these biological processes and the impact they may have on the progression of breast cancer metastasis.

5.1.1 Chapter 2- A multimodality imaging model to track viable breast cancer cells from single arrest to metastasis in the mouse brain

In Chapter 2, we combined iron-based cellular MRI with longitudinal BLI to track the fate of iron-labeled, luciferase expressing brain trophic breast cancer cells in nude mice. This is the first study demonstrating these complementary technologies can be used together to get a more holistic view of cancer cell fate in a model of experimental metastasis. In this work, BLI allowed for repetitive, non-invasive, whole body imaging and MRI based measurements of single cell arrest and tumour burden were used to validate BLI measurements. The main findings were:

1. The number of iron labeled cells that arrested throughout the brain on day 0 correlated with BLI measurements of cell viability

2. The decrease in MR void number from day 0 to day 8 correlated with changes in BLI signal

3. Total brain tumour burden measured with MRI correlated with BLI measurements of cell viability at endpoint

These findings demonstrate the value in using both technologies to noninvasively monitor the different stages of the metastatic cascade *in vivo*. The correlation seen between

modalities on the day of cell injection suggests that the majority of iron labeled cells that arrested in the brain are viable. The correlation seen between modalities at endpoint suggests that the majority of tumour burden visualized with MRI is viable tumour tissue. Our goal for the following experiment was to investigate the impact of a primary breast tumour on metastatic growth; thus, we chose to continue with this imaging model to acquire measurements of cell arrest, tumour burden and cellular viability over time. We predict this novel multimodality imaging framework will be broadly applicable to other experimental models of cancer metastasis and useful for evaluating the efficacy of emerging anti-cancer drugs at different stages of the metastatic cascade.

5.1.2 Chapter 3- Multimodality cellular and molecular imaging of concomitant tumour enhancement in a syngeneic mouse model of breast cancer metastasis

In Chapter 3, we successfully applied our multimodality imaging model to study the impact of a primary 4T1 breast tumour on the growth of 4T1BR5 derived metastases. Previous literature suggested the size of the primary tumour may influence whether CTR or CTE occurs [1]; thus, we investigated the impact of both a small and large primary tumour. While our MR analysis indicated a strong CTE effect regardless of primary tumour size, our BLI measurements suggested a significant effect on metastasis in mice with large primary tumours only. The main findings were:

1. The initial arrest and clearance of 4T1BR5 cells in the brain was not significantly different between mice that had primary tumours and control mice.

2. Mice bearing small primary tumours had significantly more MR detectable brain tumour burden at endpoint compared to mice without primary tumours; however, BLI signal was not significantly different between groups.

3. Mice bearing large primary tumours had significantly more MR detectable brain tumour burden and BLI signal at endpoint compared to mice without primary tumours.

These findings further validate the importance of using more than one technology to evaluate tumour burden in models of metastasis. While we demonstrate strong agreement between these modalities in our previous study, others have shown that measurements of tumor size (MRI) and tumor viability (BLI) do not always correlate [2]. With MRI, we are measuring tumour volume which can include areas of edema, immune cells etc., whereas BLI is a direct measure of viable engineered cells. Thus, acquiring measurements from both MRI and BLI can offer valuable insight into the disease state. In this study, by using *in vivo* BLI and MRI we could determine differences in endpoint tumour burden were not related to differences in the initial arrest or clearance of viable cells in the brain, which suggests that the presence of a primary tumour can increase the proliferative growth of brain metastases in this syngeneic 4T1 mouse model.

5.1.3   Chapter 4- Engineering self-homing circulating tumour cells as novel cancer theranostics

In chapter 4, we employed dual-luciferase BLI to evaluate the efficiency of experimental CTCs to home to disseminated metastases throughout the mouse body. Our imaging data

supported extremely efficient self-homing of systemically administered CTCs to disseminated metastases. Based on these results, we next engineered our CTCs to express a suicide gene to investigate their potential as drug delivery vehicles for self-targeted therapy of primary and metastatic tumours. The main findings of this study were:

1. Experimental CTCs home to disseminated spontaneous metastases.

2. Systemically administered therapeutic CTCs can effectively home to and treat pre-existing primary and metastatic tumours.

3. Dual-luciferase BLI allowed for sensitive visualization of CTC arrest, homing efficiency, treatment efficacy and long-term fate.

The application of dual-luciferase BLI allowed for sensitive tracking of both cell populations: metastatic breast cancer cells as well as engineered therapeutic cancer cells. By incorporating a suicide switch, we show efficient killing of engineered therapeutic cancer cells as well as a strong bystander effect whereby adjacent non-engineered cancer cells are killed. Together our findings suggest CTCs should continue to be investigated as highly-efficient carriers of therapeutic cargo to metastatic tumour sites.

5.2   Limitations

5.2.1   The use of cell lines

The results presented in this thesis are based on observations of preclinical mouse models of breast cancer metastasis. We employed three commonly used authenticated cell lines, the murine 4T1/4T1BR5 model and the human derived JIMT1BR model. The use of cell

lines in preclinical studies provides many advantages. Cell lines are relatively easy and inexpensive to maintain. Furthermore, the specific models that were used in this thesis are quite aggressive, providing a reasonable timeline for longitudinal imaging studies. However, previous studies have shown that cell lines may not accurately represent the heterogeneity of tumours that is seen in the clinic [3]. As a result, preclinical findings based on cell lines do not always translate accordingly. This limitation can be addressed by implementing patient derived xenograft (PDX) models for preclinical cancer studies. This involves implanting a tumour fragment or suspension from a patient directly into an immune compromised animal and continued passaging of any resultant tumours in additional mice cohorts [4]. In recent years, it has been shown that PDX models have similar tumour characteristics to those observed in the clinic and as a result, have more predictive value when translating to patient studies [5,6]. While our group is transitioning towards the use of PDX models, the aggressive cancer cell lines used in this thesis provided models of consistent and timely breast cancer brain metastasis that can take months to generate with PDX models, if at all in the majority of mice. In addition, the ease of expansion and stability of these cell lines in culture allowed us to genetically engineer them to express our imaging reporter genes with high efficiency. Moving forward, we will use the imaging framework and experimental techniques developed in this thesis to study metastasis in PDX models of breast cancer.

5.2.2 Preclinical imaging techniques

The imaging technologies presented in this thesis are extremely valuable tools for tracking cancer populations in preclinical animal models. Iron-based cellular MRI enables single

cell detection throughout the brain providing measurements of cell arrest, cell clearance, and cell dormancy [7,8]. BLI enables sensitive detection of whole-body metastatic burden and provides longitudinal measurements of cancer cell viability [9,10]. However, these cell tracking technologies are limited to preclinical use since they rely on the cancer cells being labeled in culture. We chose to use these modalities to visualize very early stages of the metastatic cascade that are not possible to study using clinically relevant modalities. In the future, we could use conventional MR and/or PET imaging to acquire both anatomical and functional tumour measurements that would be feasible to obtain in a clinical setting.

5.2.3   Genetically-engineered cells

In this thesis, we employ lentiviral transduction methods to engineer cancer cells to stably express various imaging reporter genes. While lentiviruses are commonly used due to their high transduction efficiency, they have some concerns regarding whether the labeling can change the biology of the engineered cells. Most lentiviral systems that are currently in use are derived from the human immunodeficiency viruses (HIV) and lentiviral cargo integrates randomly into the genome upon infection to permit stable expression in both dividing and non-dividing cell populations [11]. Random integration can cause unwanted detrimental effects such as transgene silencing, altered cell behavior, or insertional activation of oncogenes [12-15]. To overcome this, our lab is currently developing clustered regularly interspaced short palindromic repeats (CRISPR) and CRISPR-associated protein 9 (Cas9) tools to allow for precise editing of cells at the adeno-associated virus site 1 (AAVS1) safe harbour. Our group has shown successful AAVS1 integration of large gene constructs necessary for molecular-genetic imaging using the CRISPR/Cas9

system [16]. Future work is focused on improving the efficiency of this first system, which will allow us to use it reporter gene-based for cell tracking studies the lack the issues associated with random integration.

5.3   Future Work

This thesis includes some of the first studies using longitudinal imaging to study the mechanisms contributing to breast cancer metastasis. Future work will be focused on translational studies that bridge the gap between our initial findings presented here and future clinical studies. First, we will implement PDX models of breast cancer to better understand clinical cases of CTR versus CTE. In addition, future work will focus on developing more clinically relevant imaging models to visualize CTC self-homing *in vivo*.

5.3.1   Implementing PDX models to study CTR/CTE

The clinical evidence of CTR and CTE remains lacking due to the fact that investigation depends on the presence of an existing primary tumour. While there have been reported cases of both CTR and CTE [17-22], it is not clear what stratifies patients into experiencing one or the other. With the use of cell lines, we have previously demonstrated CTR in an immune deficient mouse model as well as CTE in an immune competent mouse model in the current work [23]. Others have also shown that both CTR and CTE can occur within the same animals depending on the ratio of the size of primary tumour to secondary tumour [1]. By implementing PDX models to study CTR/CTE, we may be able to better represent the tumour heterogeneity that is evident in the clinic to more accurately identify breast cancer patients that would benefit from tumour resection or alternative therapy.

174

5.3.2 Visualizing CTC tumour self-homing with a clinically - relevant imaging modality

In chapter 4, we employed dual-luciferase BLI to sensitively monitor CTC self-homing efficiency to primary and metastatic tumour sites. In future studies, we want to investigate whether CTC self-homing can be visualized with other technologies we use in our lab such as iron-based cellular MR and Fluorine-19 MR. Iron-based cellular MRI may enable detection of single iron labeled self-homing CTCs, while Fluorine-19 MR would provide a quantifiable technique to estimate the number of CTCs that home to a targeted tumour site.

We also plan to investigate the use of a human derived MR reporter gene to track the engineered CTCs in our mouse models. Our group has recently shown that the organic anion transporting polypeptide 1 (OATP1), a protein that is naturally expressed in the human liver, can be encoded into cancer cells for enhanced uptake of the gadolinium agent Gd-EOB-DTPA, and thus, improved detection by MR [24]. This reporter has high translational potential as it will avoid potential immune reactions in patients that may be caused by other reporter genes such as virally-derived HSV-TK, and Gd-EOB-DTPA is clinically used.

5.4   References

1. J. Bruzzo, P. Chiarella, R.P. Meiss, R.A. Ruggiero, Biphasic effect of a primary tumor on the growth of secondary tumor implants, J. Cancer Res. and Clin. Oncol. 136; 1605–1615. (2010).

2. Le, T. N., Lim, H., Hamilton, A. M., Parkins, K. M., Chen, Y., Scholl, T. J., & Ronald, J. A. Characterization of an orthotopic rat model of glioblastoma using multiparametric magnetic resonance imaging and bioluminescence imaging. *Tomography*, *4*(2), 55. (2018).

3. Gillet, J. P., Varma, S., & Gottesman, M. M. The clinical relevance of cancer cell lines. *Journal of the National Cancer Institute*, *105*(7), 452-458. (2013).

4. Hidalgo, M., Amant, F., Biankin, A. V., Budinská, E., Byrne, A. T., Caldas, C., ... & Roman-Roman, S. Patient-derived xenograft models: an emerging platform for translational cancer research. *Cancer discovery*, *4*(9), 998-1013. (2014).

5. Fiebig, HH., Neumann, HA., Henss, H., Koch, H., Kaiser, D., Arnold, H. Development of three human small cell lung cancer models in nude mice. Recent Results Cancer Res. 97:77–86. (1985).

6. Houghton, JA., Houghton, PJ., Green, AA. Chemotherapy of childhood rhabdomyosarcomas growing as xenografts in immune-deprived mice. Cancer Res. 42:535–9. (1982).

7. Heyn, C., Ronald, JA., Ramadan, SS., Snir, JA., Barry, AM., MacKenzie, LT. et al. In vivo MRI of cancer cell fate at the single-cell level in a mouse model of breast cancer metastasis to the brain. Magn Reson Med. 56:1001–10. (2006).

8. Heyn, C., Bowen, CV., Rutt, BK., Foster, PJ. Detection threshold of single SPIO labeled cells with FIESTA. Magn Reson Med. 53:312–20. (2005).

9. Contag, P. R., Olomu, I. N., Stevenson, D. K. & Contag, C. H. Bioluminescent indicators in living mammals. Nat. Med. 4, 245-247. (1998).

10. Contag, CH., Spilman, SD., Contag, PR., Oshiro, M., Eames, B. et al. Visualizing gene expression in living mammals using a bioluminescent reporter. *Photochem. Photobiol.* 66:523–31. (1997).

11. Tiscornia, G., Singer, O., & Verma, I. M. Production and purification of lentiviral vectors. *Nature protocols*, *1*(1), 241. (2006).

12. Martin, D. I. & Whitelaw, E. The vagaries of variegating transgenes. Bioessays 18, 919-923. (1996).

13. Kioussis, D. & Festenstein, R. Locus control regions: overcoming heterochromatin-induced gene inactivation in mammals. Curr. Opin. Genet. Dev. 7, 614-619. (1997).

14. Rivella, S. & Sadelain, M. Genetic treatment of severe hemoglobinopathies: the combat against transgene variegation and transgene silencing. Semin. Hematol. 35, 112-125. (1998).

15. Bestor, T. H. Gene silencing as a threat to the success of gene therapy. J. Clin. Invest. 105, 409-411. (2000).

16. Dubois, V. P., Zotova, D., Parkins, K. M., Swick, C., Hamilton, A. M., Kelly, J. J., & Ronald, J. A. Safe Harbor Targeted CRISPR-Cas9 Tools for Molecular-Genetic Imaging of Cells in Living Subjects. *The CRISPR Journal*, *1*(6), 440-449. (2018).

17. Vizel, M., Oster, MW., Austin, JH. Spontaneous regression of a pulmonary

metastasis after nephrectomy for renal cell carcinoma, J. Surg. Oncol. 12; 175–180. (1979).

18. Lokick, J. Spontaneous regression of metastatic renal cancer. Case report and literature review, Am. J. Clin. Oncol. 20 ; 416–418. (1997).

19. Wyczolkowski, M., Klima, W., Bieda, W., Walask, K. Spontaneous regression of hepatic metastases after nephrectomy and mastectomy of renal cell carcinoma, Urol. Int. 66;119–120. (2001).

20. Lekanidi, K., Vlachou, PA., Morgan, B., Vasanthan, S. Spontaneous regression of metastatic renal cell carcinoma: case report, J. Med. Case Reports 1; 89. (2007).

21. Lange, PH., Hekmat, K., Bosl, G., Kennedy, BJ., Fraley, EE. Accelerated growth of testicular cancer after cytoreductive surgery, Cancer 45; 1498–1506. (1980).

22. Qadri, SS., Wang, JH., Coffey, JC., Alam, M., O'Donnell, A., Aherne, T., Redmond, HP. Can surgery for cancer accelerate the progression of secondary tumors within residual minimal disease at both local and systemic levels? Ann Thorac. Surg. 80; 1046–1050. (2005).

23. Hamilton, A. M., Parkins, K. M., Murrell, D. H., Ronald, J. A., & Foster, P. J. Investigating the impact of a primary tumor on metastasis and dormancy using MRI: new insights into the mechanism of concomitant tumor resistance. *Tomography*, *2*(2), 79. (2016).

24. Nyström, N. N., Hamilton, A. M., Xia, W., Liu, S., Scholl, T. J., & Ronald, J. A. Longitudinal Visualization of Viable Cancer Cell Intratumoral Distribution in Mouse Models Using Oatp1a1-Enhanced Magnetic Resonance Imaging. *Invest Radiol*. (2019).

# Appendices

Appendix A: Supplementary Figures
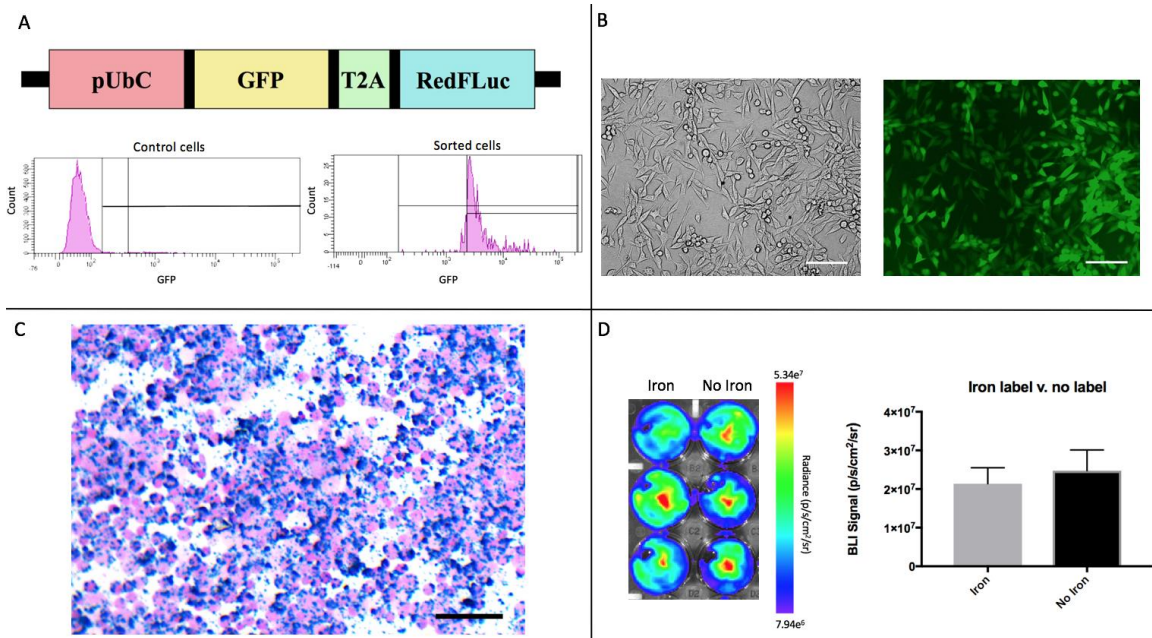
Supplementary Figure 3.1: A/B) 4T1-BR5 cells were transduced and sorted to stably co-express Red-FLuc/GFP using a commercial lentiviral vector (Scale bars = 100 microns). C) The resultant 4T1BR5-Red-FLuc/GFP cells were efficiently labeled with > 90% of cells labeled with MPIO prior to intracardiac injection (Scale bar = 200 microns). D) No significant difference in BLI signal was detected in 4T1BR5-Red-FLuc/GFP cells that were labeled with MPIO and cells that were not labeled. Data is presented as mean +/- SD.
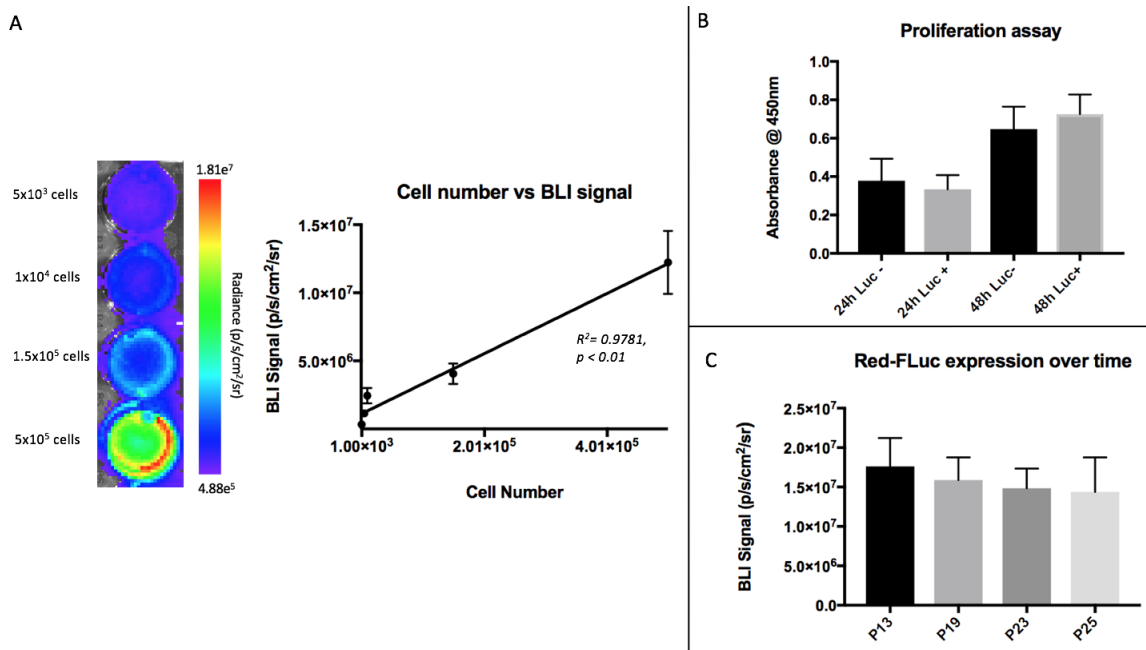
Supplementary Figure 3.2: A significant positive correlation was found between the number of 4T1BR5-Red-FLuc/GFP cells and BLI signal (A). There was not a significant difference in cellular proliferation detected between naïve 4T1-BR5 and 4T1BR5-Red-FLuc/GFP cells (B). 4T1-BR5-Red-Fluc/GFP cells showed no significant change in Red-Fluc expression over multiple passages in vitro (C).
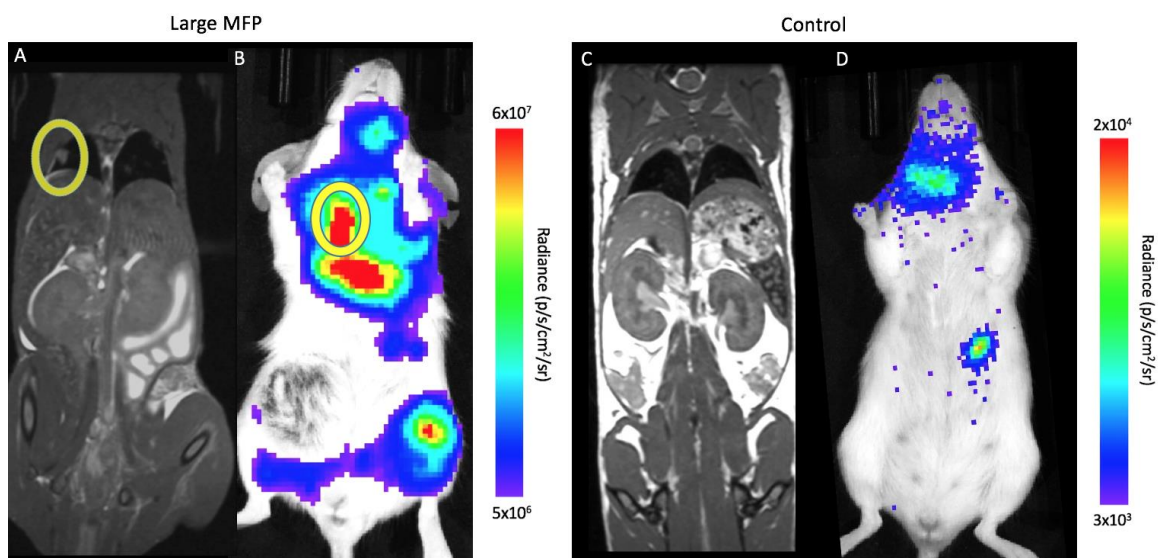
Supplementary Figure 3.3: A) Lung metastases (circled in yellow) were detectable at day 14 with whole body MRI in mice with a large MFP primary tumor, but C) not control mice. B) BLI signal was also detected in the lung region of large MFP mice on day 14, but D) not control mice.
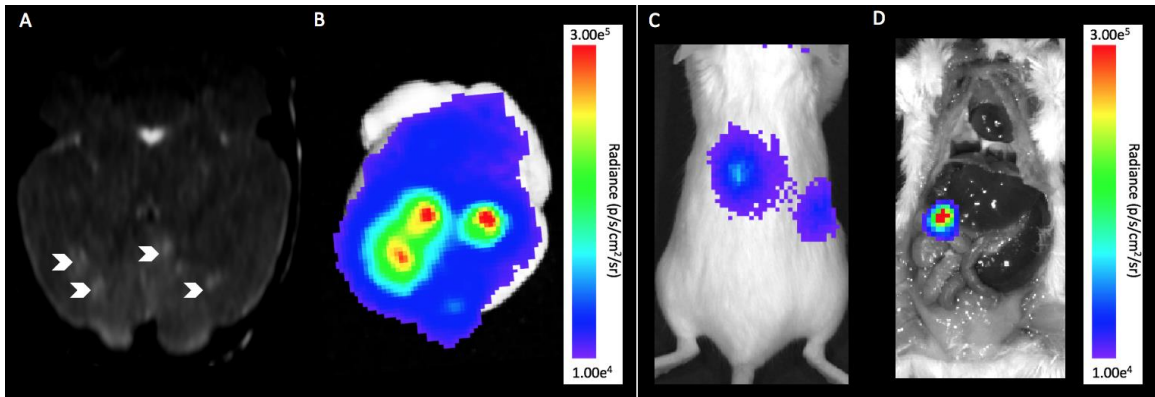
Supplementary Figure 3.4: A representative in vivo MR image of the brain (A) and corresponding ex vivo BLI (B); *in vivo (C)* **and** *ex vivo (D)* **whole body BLI were also matched presenting signal in the abdominal region.**
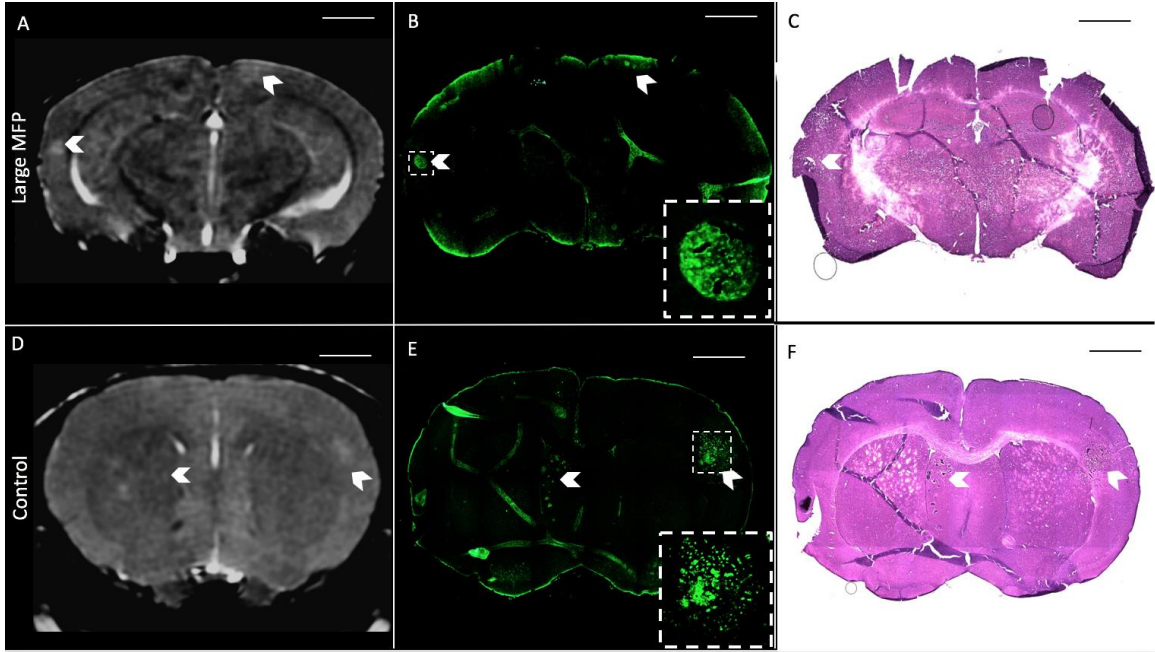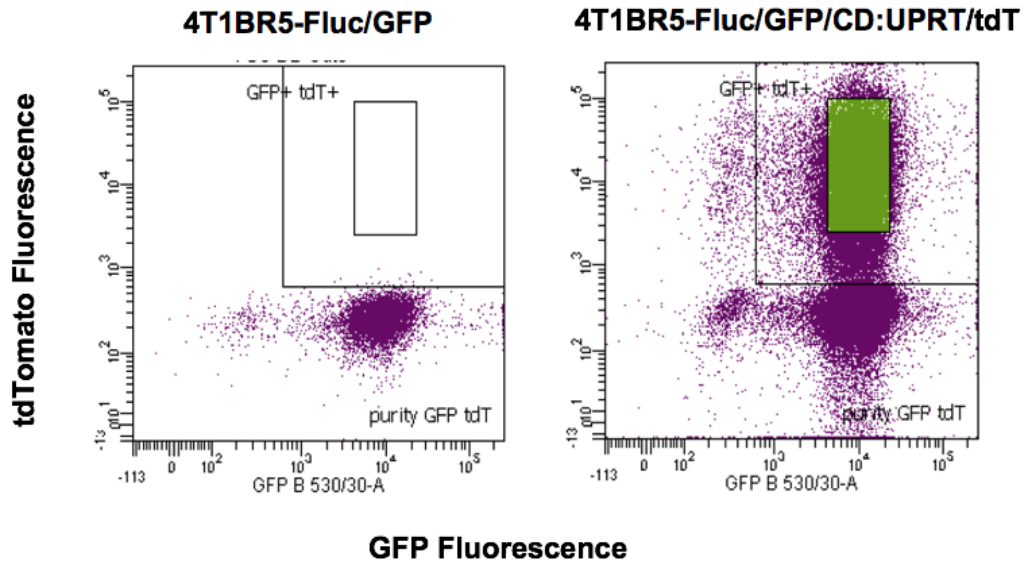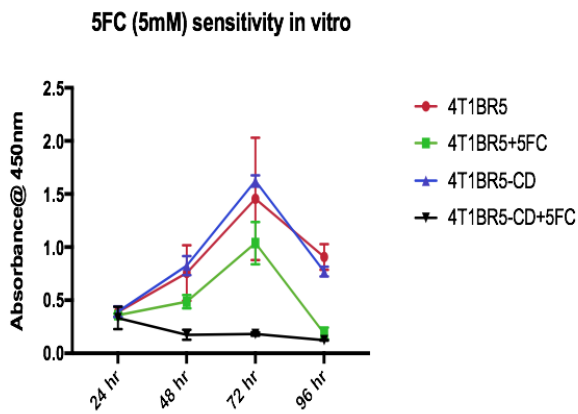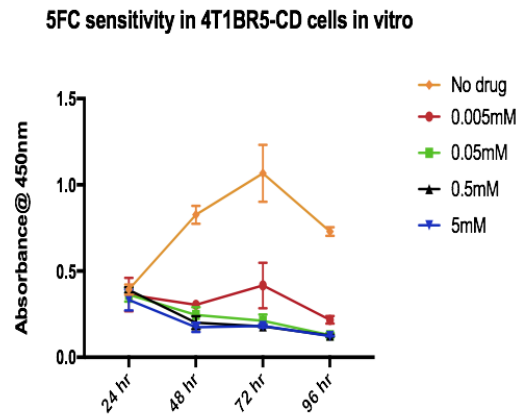
Supplementary Figure 3.5: A representative MR slice (A/D) corresponded well with GFP positive cells (B/E) and H&E staining (C/F) confirming that MR-detectable metastases contain 4T1BR5-Red-FLuc/GFP cells. Scale bars = 500 microns.
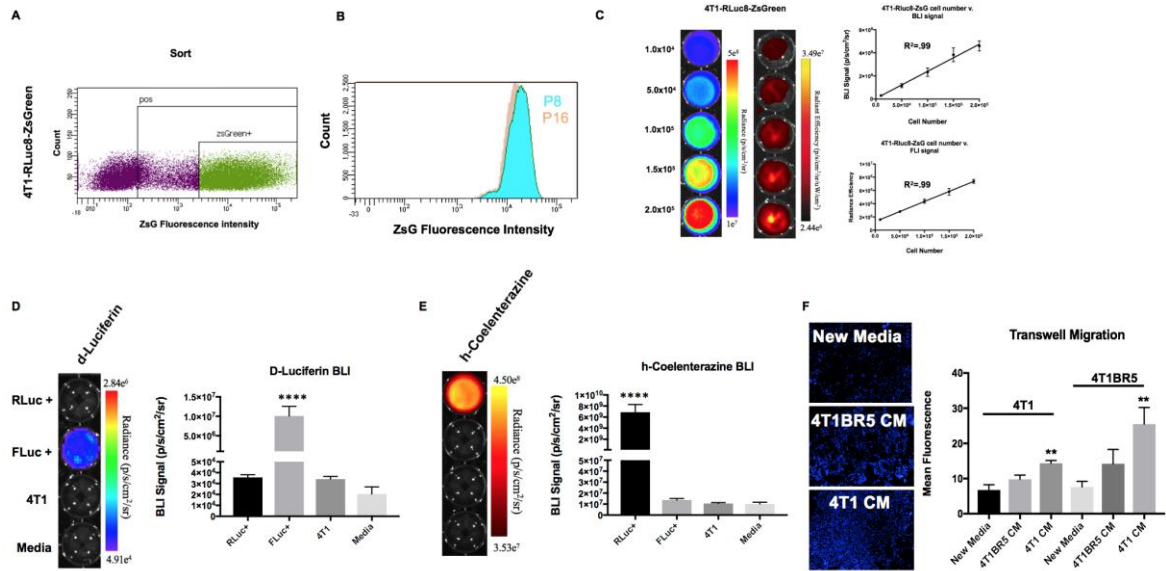
Supplementary Figure 4.1: 4T1 cells were transduced with a lentiviral vector encoding both RLuc and ZsGreen and sorted to obtain 4T1-RLuc cells (Suppl. Fig. 1A). No significant change in ZsGreen expression over multiple passages was seen (B). There was a significant positive correlation shown between the number of 4T1-RLuc cells and RLuc/ZsGreen signal (C). 4T1BR5-FLuc cells incubated with D-luciferin demonstrated significantly higher BLI signal than 4T1-RLuc cells, 4T1 parental cells, or equivalent volume of media, and 4T1-RLuc cells did not produce signal significantly different than 4T1 parental cells or media alone (D). Similarly, after the addition of h-coelenterazine, 4T1-RLuc cells had significantly higher signal than 4T1BR5-FLuc cells, 4T1 parental cells, or equivalent volume of media and 4T1BR5-FLuc cells did not produce signal significantly different than 4T1 parental cells or media alone (E). A significant increase in cell migration was seen for 4T1BR5 cells when conditioned media from 4T1 cells was used compared to conditioned media from 4T1BR5 cells or unconditioned media (F). A significant increase in cell migration was also seen for 4T1 cells when conditioned media from 4T1 cells was used compared to unconditioned media (F).
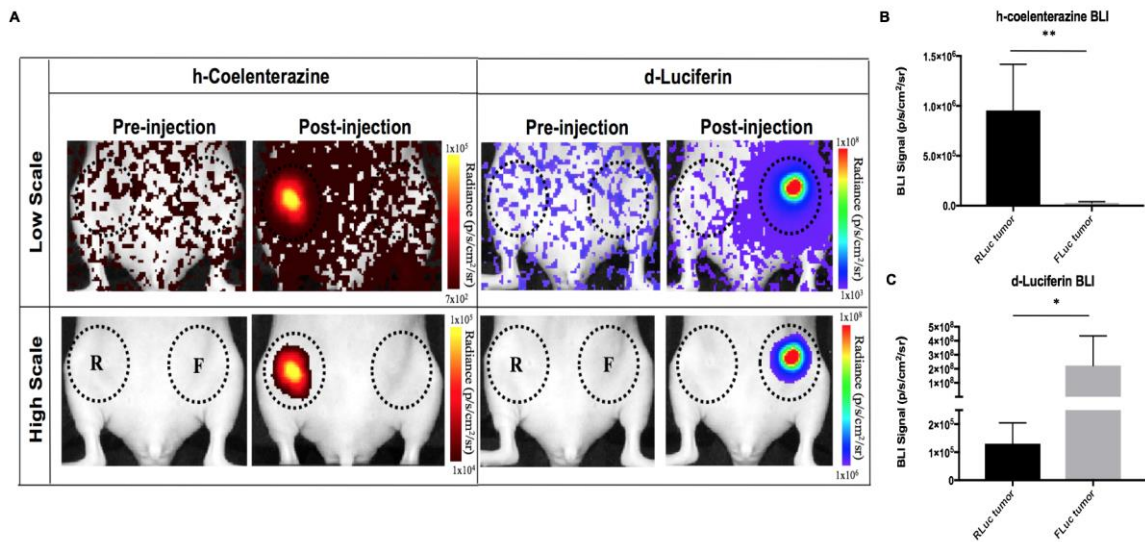
Supplementary Figure 4.2: In vivo cross reactivity: 4T1-RLuc cells were implanted into the right MFP of nude mice (n=5) and 4T1BR5-FLuc cells were implanted into the contralateral (left) MFP (A). This allowed us to validate the lack of substrate cross-reactivity *in vivo* at early time points after cell injection. On Day 0, 4T1-RLuc cells only showed signal after administration with h-coelenterazine and signal in the right MFP was significantly higher than the left (B). Similarly, on Day 1, 4T1BR5-FLuc cells only showed signal after administration of d-Luciferin and signal in the left MFP was significantly higher than in the right MFP (C).

A

4T1BR5-Fluc/GFP   4T1BR5-Fluc/GFP/CD:UPRT/tdT

tdTomato Fluorescence

GFP+ tdT+   GFP+ tdT+

purity GFP tdT   purity GFP tdT

GFP B 530/30-A

GFP Fluorescence

B

5FC (5mM) sensitivity in vitro

Absorbance@ 450nm

- 4T1BR5
- 4T1BR5+5FC
- 4T1BR5-CD
- 4T1BR5-CD+5FC

24 hr, 48 hr, 72 hr, 96 hr

C

5FC sensitivity in 4T1BR5-CD cells in vitro

Absorbance@ 450nm

- No drug
- 0.005mM
- 0.05mM
- 0.5mM
- 5mM

24 hr, 48 hr, 72 hr, 96 hr

Supplementary Figure 4.3: 4T1BR5-FLuc cells were transduced with a lentiviral vector co-expressing the therapeutic prodrug converting fusion enzyme cytosine deaminase-uracil phosphoribosyltransferase (CD:UPRT) and tdTomato (tdT), and sorted via tdT to obtain 4T1BR5-FLuc/CD cells (A). After 96 hours of incubation with 5'FC (5mM), CD expressing cells showed significantly less survival than cells without drug as well as significantly less survival than 4T1BR5-FLuc with or without drug

(B). At all doses, CD expressing cells show significantly less survival than cells without drug (C).

A

Belly up days 19/20	Mouse 1	Mouse 2	Mouse 3	Mouse 4	Mouse 5	Mean +/- SEM
Total tumors	11	18	7	7	10	10.6+/- 2.0
RLuc+/ Fluc-	2	1	0	0	0	0.6+/- 0.4
RLuc-/ Fluc+	0	0	0	0	1	0.2 +/- 0.2
Rluc +/Fluc+	9	17	7	7	9	9.8+/-1.86

B

C
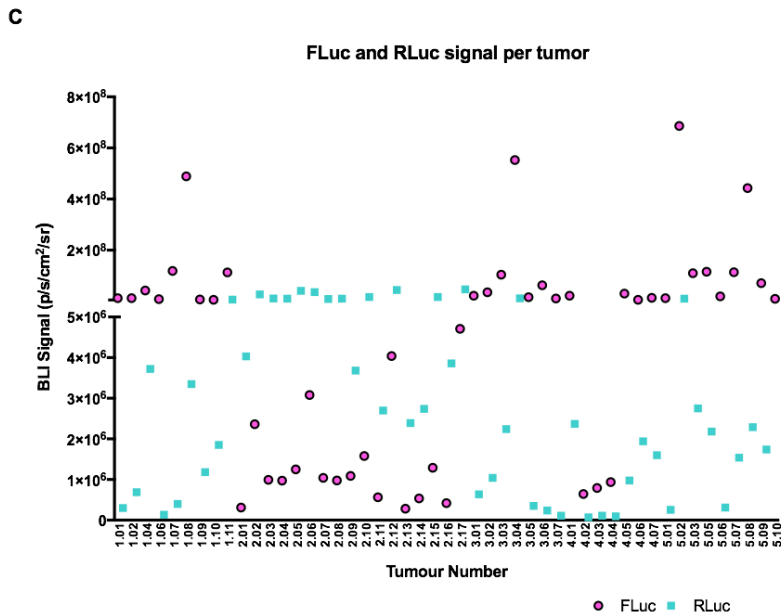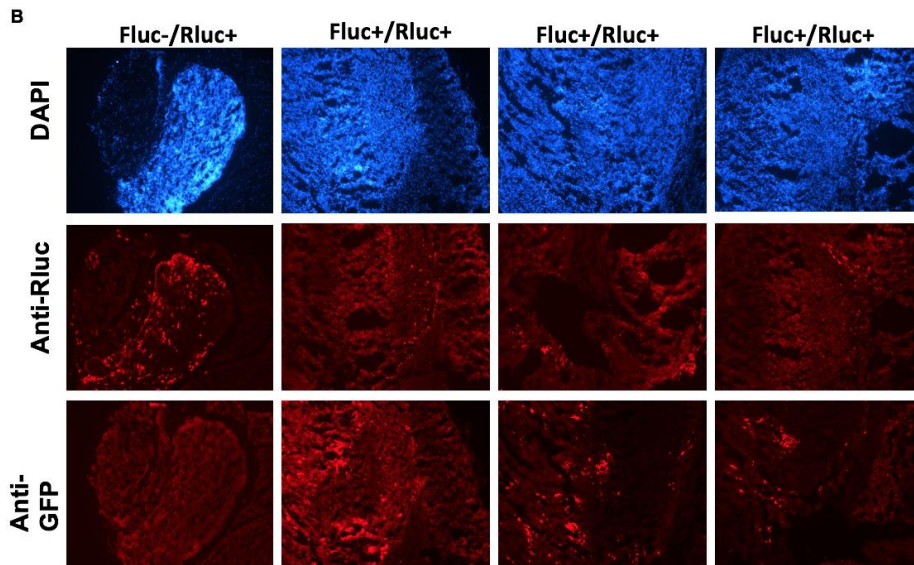
Supplementary Figure 4.4: At endpoint, the number of metastases that were composed of both 4T1-RLuc and 4T1BR5-FLuc cells was significantly higher than

the number of metastases that were either 4T1-RLuc-positive only or 4T1BR5-FLuc-positive only (A). The presence of both 4T1-RLuc and 4T1BR5-FLuc cells in numerous metastases was confirmed histologically (B). Using dual-BLI, we detected some whole-body metastases that had stronger FLuc signal than RLuc signal as well as metastases that had stronger RLuc signal than FLuc signal (X-axis values= mouse number followed by tumour number) (C).

Appendix B: Permissions

Copyright Clearance Center

RightsLink®

SPRINGER NATURE

Title:	A multimodality imaging model to track viable breast cancer cells from single arrest to metastasis in the mouse brain
Author:	Katie M. Parkins, Amanda M. Hamilton, Ashley V. Makela, Yuanxin Chen, Paula J. Foster et al.
Publication:	Scientific Reports
Publisher:	Springer Nature
Date:	Oct 21, 2016

Copyright © 2016, Springer Nature

Creative Commons

RightsLink

Katie M. Parkins

EDUCATION

09/15-08/19	**PhD Medical Biophysics (Molecular Imaging)** University of Western Ontario, London, Ontario
09/11-06/15	**BSc (Hons) Brain and Cognition Specialization** The University of Guelph, Guelph, Ontario

SCHOLARSHIPS AND AWARDS

06/19	**World Molecular Imaging Congress 2019** Trainee Travel Award ($350 USD)
04/19	**London Health Research Day 2019** Top oral presentation award ($650)
03/19	**Imaging Network of Ontario Conference 2019** 1st Place Oral Presentation Award ($350)
06/18	**International Society for Magnetic Resonance in Medicine 2018** 1st Place Oral Presentation: Cellular and Molecular Imaging (300 Euros)
05/18	**Natural Sciences and Engineering Research Council-PGS-Doctoral Award** $63,000 over thirty-six months
03/18	**Imaging Network of Ontario Conference 2018** 1st Place Poster Presentation Award ($350)
02/18	**International Society for Magnetic Resonance in Medicine 2018** Trainee Travel Award ($525)
01/18	**Western Molecular Imaging Program Exchange Travel Award 2018** Held at Stanford Molecular Imaging Program ($1500)
09/17	**Cancer Research and Technology Transfer Scholar** Doctoral award ($26,500) (*Declined)

| 09/17 | **Ontario Graduate Scholarship: QEII-Science and Technology Award** |
| | Doctoral award ($15,000) |

| 06/17 | **Norma E. Nixon Marie Ramo Nixon Award 2017** |
| | Awarded based on academic achievement and research merit ($2600) |

| 06/17 | **Oncology Research and Education Day 2017** |
| | 1st Place Poster Presentation ($50) |

| 03/17 | **Lucille and Norton Wolf Publication Award 2017** |
| | Awarded to the top-scoring trainee peer-reviewed publication that appeared in press from January 1, 2016 to December 31, 2016 ($1,000) |

| 09/16 | **Translational Breast Cancer Studentship funded in part by the Breast Cancer Society of Canada-** Doctoral award ($18,000) |

| 09/16 | **Western Molecular Imaging Graduate Program Travel Award** ($400) |

| 09/15 | **Translational Breast Cancer Studentship funded in part by the Breast Cancer Society of Canada-** Masters award ($17,000) |

09/15	**Western Graduate Research Scholarship** ($4,500 per year)
	University of Western Ontario; Department of Medical Biophysics
	Students achieving >78% admission average

TEACHING

09/16-04/19	**Teaching Assistant, The University of Western Ontario**
	Department of Medical Biophysics
	Course ID: MEDBIO 3970Z: General Biophysics Laboratory
	Course Coordinator: Dr. John Ronald

| 05/16, 05/17 | **Let's Talk Cancer, Session Leader, Western University** |
| | Session title: *"Tracking cancer with novel imaging technologies"* |

| 10/14 | **Teaching Assistant, The Hospital for Sick Children, Toronto, Ontario** |
| | Pediatric Emergency Medicine Ultrasound Workshop |

MENTORING

09/17-04/18	**Supervisor/Mentor for Medical Biophysics 4970 Thesis**
	Student: Veronica Dubois
	Project Title: *"Genome editing of cell lines with reporter genes for in vivo*

cell tracking using CRISPR-Cas9 technology"

09/17-04/18	**Supervisor/Mentor for Biology 4999E Thesis** Student: Vyshnave Jeyabalan Project Title: "*Developing a non-integrating lentiviral- S/MAR vector system for safe molecular-genetic imaging of transplanted cells in vivo*"
09/16-04/17	**Supervisor/Mentor for Medical Biophysics 3970Z Independent Research Project** Student: Veronica Dubois Project Title: *"Towards In Vivo Multimodality Imaging of Cancer: Assessment of proliferation rate and imaging signal of reporter-gene expressing cancer cells in culture"*

PEER-REVIEWED JOURNAL ARTICLES

Parkins KM, Dubois VP, Kelly JJ, Chen Y, Foster PJ, Ronald JA. "Engineering self-homing circulating tumor cells as novel cancer theranostics". *In preparation*.

Ivanova A, Arulanantham S, Barr K, Cepeda M, **Parkins KM**, Hamilton AM, Johnston D, Penuela S, Hess DA Ronald JA, Dagnino L. "Targeting FER kinase inhibits melanoma growth and metastasis". *Cancers*. March 2019.

Dubois V*, Zotova D*, **Parkins KM**, Swick C, Kelly JJ, Hamilton AM, Ronald JA. "Safe harbor targeted CRISPR/Cas9 tools for molecular-genetic imaging of cells in living subjects". *The CRISPR Journal*. 1(6): 440-449. December 2018.

Parkins KM, Dubois V, Wong S, Hamilton AM, Foster PJ, Ronald JA. "Cellular MRI reveals altered brain arrest of genetically-engineered metastatic breast cancer cells". *Contrast Media and Molecular Imaging*. December 2018.

Parkins KM, Dubois V, Hamilton AM, Makela AV, Ronald JA, Foster PJ. "Multimodality cellular and molecular imaging of the impact of a primary tumor on metastatic growth in a syngeneic mouse model of breast cancer brain metastasis" *Scientific Reports*. June 2018.

Le TNT, Lim H, Hamilton AM, **Parkins KM**, Chen Y, Scholl TJ, Ronald JA. "Characterization of an Orthotopic Rat Model of Glioblastoma Using Multiparametric Magnetic Resonance Imaging and Bioluminescence Imaging" *Tomography*. July 2018.

Williams K, Cepeda M, Searle K, **Parkins K**, Makela A, Hamilton A, Kim Y, Ronald J, Foster P, Chambers A, Leong H, and Tuck A. "PAK1 Regulates In Vivo Invadopodia Chemosensing During Cancer Cell Extravasation and is Important for Metastatic Efficiency". *Oncogene.* December 2018.

Parkins KM, Hamilton AM, Makela AV, Chen Y, Foster PJ, Ronald JA. "A multimodality imaging model to track viable cancer cells from single arrest to metastasis" *Scientific Reports.* October 2016.

Hamilton AM, **Parkins KM**, Murrell DH, Ronald JA, Foster PJ. "Investigating the Impact of a Primary Tumor on Metastasis and Dormancy Using MRI: New Insights into the Mechanism of Concomitant Tumor Resistance". *Tomography.* July 2016.

Chen Y, Hamilton AM, **Parkins KM**, Wang J-X, Zeineh M, Rogers KA, Rutt BK, Ronald JA. "Magnetic resonance imaging and histopathologic analysis of a novel cholesterol fed rabbit model of xanthogranuloma". *Journal of Magnetic Resonance Imaging.* February 2016.

BOOK CHAPTERS

Parkins KM, Makela AV, Hamilton AM, Foster PJ. "Cellular Magnetic Resonance Imaging for Tracking Metastatic Cancer Cells in the Brain" *Methods in Molecular Biology; Brain tumor stem cells.* October 2018.

Makela A*, Murrell DH*, **Parkins KM**, Kara J, Gaudet J, Foster PJ. "Cellular Imaging with MRI" *Topics in Magnetic Resonance Imaging.* October 2016.

Bazalova-Carter M, Murrell DH, **Parkins KM**, Ronald J, Foster PJ, Graves E, Granton P, and Wong E. "Small Animal Radiotherapy and Imaging" *Advances in Medical Biophysics.* March 2016.

PRESENTATIONS

KM Parkins, AM Hamilton, AV Makela, PJ Foster, JA Ronald. The development of a multimodality imaging model to monitor breast cancer metastasis. *Imaging Network of Ontario, March 2016,* Toronto, Ontario, CA. **Poster Presentation**

KM Parkins, AM Hamilton, AV Makela, PJ Foster, JA Ronald. Monitoring breast cancer metastasis with a multimodality imaging model. *London Health Research Day, March 2016,* London, Ontario, CA. **Poster Presentation. Ranked top 100 abstract.**

KM Parkins, AM Hamilton, AV Makela, PJ Foster, JA Ronald. A multimodality imaging model to monitor cancer metastasis. *Oncology and Research Education Day, June 2016,* London, Ontario, CA. **Poster Presentation.**

KM Parkins, AM Hamilton, AV Makela, PJ Foster, JA Ronald. A multimodality imaging model to monitor cancer metastasis. *Robarts Research Retreat, June 2016,* London, Ontario, CA. **Poster Presentation.**

KM Parkins, AM Hamilton, AV Makela, PJ Foster, JA Ronald. Filling the MR void with

BLI: A multimodality imaging model to track viable cancer cells from single arrest to metastasis *London Imaging Discovery Conference, June 2016,* London, Ontario, CA. **Poster Presentation.**

KM Parkins, AM Hamilton, AV Makela, PJ Foster, JA Ronald, Filling the MR void with BLI: A multimodality imaging model to track viable cancer cells from single arrest to metastasis. *World Molecular Imaging Congress, September 2016,* New York, USA. **Poster Presentation**

KM Parkins, AM Hamilton, AV Makela, PJ Foster, JA Ronald. The development of a multimodality imaging model to monitor breast cancer metastasis. *Brain Tumour Foundation of Canada, October 2016,* Toronto, Ontario, CA. **Poster Presentation**

KM Parkins, V Dubois, AM Hamilton, JA Ronald, PJ Foster. A multimodality imaging model to study concomitant tumour resistance. Imaging network of Ontario. London, Ontario. March 2017. **Oral Presentation.**

KM Parkins, V Dubois, A Makela, AM Hamilton, JA Ronald, PJ Foster. A multimodality imaging model to study concomitant tumour resistance. *London Health Research Day*. London, Ontario. March 2017. **Poster Presentation**.

KM Parkins, V Dubois, A Makela, AM Hamilton, JA Ronald, PJ Foster. A multimodality imaging model to study concomitant tumour resistance. *Robarts Research Retreat*. London, Ontario. June 2017. **Oral Presentation**.

KM Parkins, V Dubois, A Makela, AM Hamilton, JA Ronald, PJ Foster. A multimodality imaging model to study concomitant tumour resistance. *Oncology Research and Education day*, London, Ontario. June 2017. **Poster Presentation**.

KM Parkins, V Dubois, A Makela, AM Hamilton, JA Ronald, PJ Foster. Building new imaging technologies to study breast cancer metastasis in the brain. *Internal review and site visit by the Breast Cancer Society of Canada*, London, Ontario. June 2017. **Invited Talk**.

KM Parkins, V Dubois, AM Hamilton, A Makela, JA Ronald, PJ Foster. A multimodality imaging model to study the impact of a primary tumour on metastasis. *Canadian Cancer Research Conference*. Vancouver, CA. November 2017. **Poster Presentation.**

KM Parkins, V Dubois, A Makela, AM Hamilton, JA Ronald, PJ Foster. Investigating the impact of a primary tumour on metastatic outgrowth in a syngeneic mouse model of breast cancer. *Stanford University*, Molecular Imaging Program & Radiological Science Laboratories, California, USA. January 2018. **Invited Talk**.

KM Parkins, V Dubois, A Makela, AM Hamilton, JA Ronald, PJ Foster. Investigating the impact of a primary tumour on metastatic outgrowth in a syngeneic mouse model of breast

cancer. *AC burton Day, Department of Medical Biophysics, Western University, London, Ontario.* May 2018. **Invited Talk.**

KM Parkins, V Dubois, A Makela, AM Hamilton, JA Ronald, PJ Foster. Investigating the impact of a primary tumour on metastatic outgrowth in a syngeneic mouse model of breast cancer. *International Society for Magnetic Resonance in Medicine.* Paris, France. June 2018. **Oral Presentation**.

KM Parkins, V Dubois, A Makela, AM Hamilton, JA Ronald, PJ Foster. Investigating the impact of a primary tumour on metastatic outgrowth in a syngeneic mouse model of breast cancer. *Oncology Research and Education day*, London, Ontario. June 2018. **Poster Presentation.**

KM Parkins, V Dubois, A Makela, AM Hamilton, JA Ronald, PJ Foster. Investigating the impact of a primary tumour on metastatic outgrowth in a syngeneic mouse model of breast cancer. *German Cancer Research Centre*, Heidelberg, Germany. June 2018. **Invited Talk**.

KM Parkins, V Dubois, J Kelly, Y Chen, PJ Foster, JA Ronald. Dual-luciferase imaging enables visualization of efficient tumour self-homing of metastatic breast lesions. *Imaging Network of Ontario*. London, Ontario. March 2019. **Oral Presentation. *Top presentation award.**

KM Parkins, V Dubois, J Kelly, Y Chen, PJ Foster, JA Ronald. Dual-luciferase imaging enables visualization of efficient tumour self-homing of metastatic breast lesions. *London Health Research Day*. London, Ontario. April 2019. **Oral Presentation. *Top presentation award.**

KM Parkins, V Dubois, J Kelly, Y Chen, PJ Foster, JA Ronald. Engineering self-homing circulating tumor cells as a novel cancer theranostic. *World Molecular Imaging Congress.* Montreal, Quebec. September 2019. **Oral Presentation.**